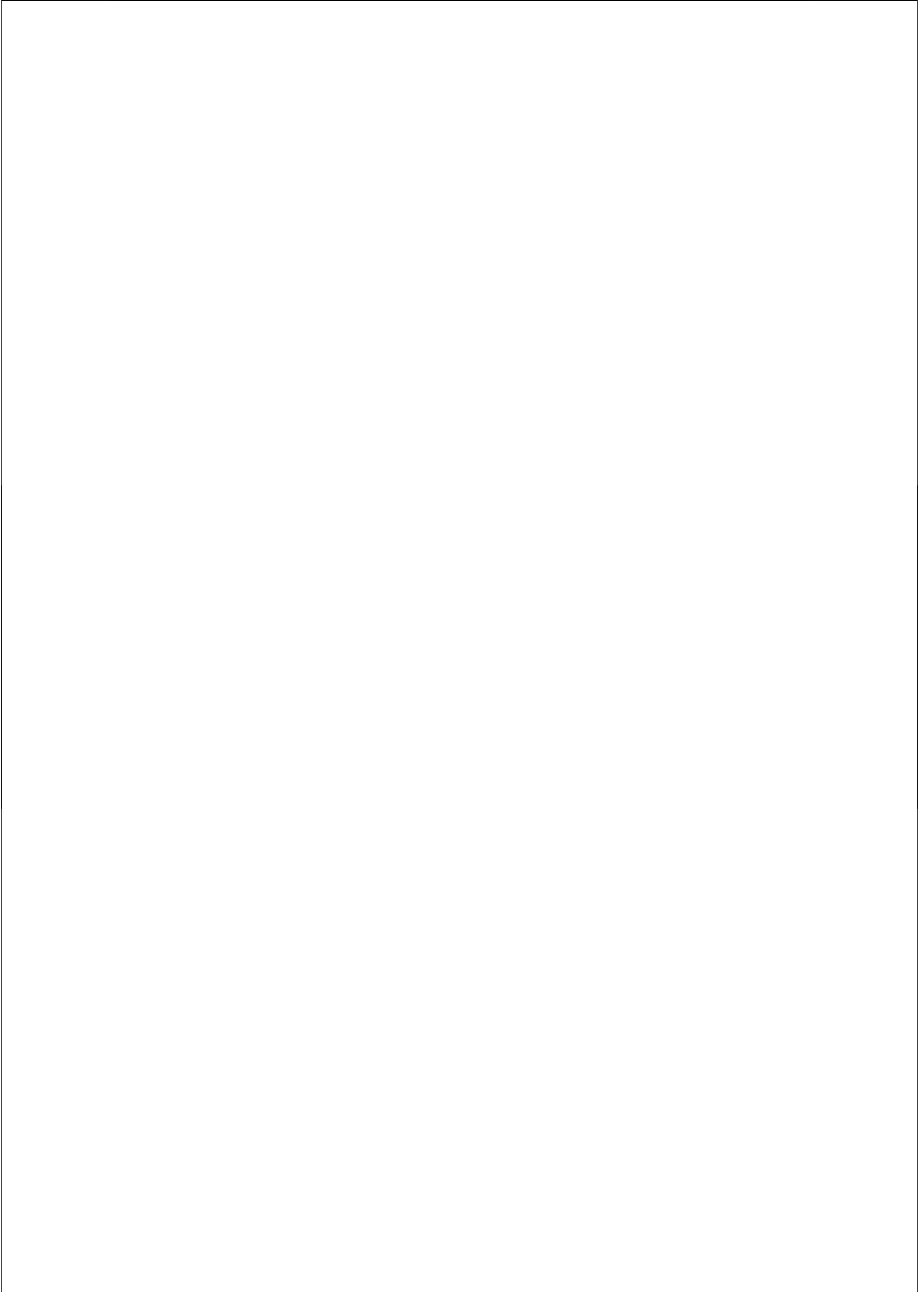

Manipulation of Ultracold Bose Gases
in a Time-averaged Orbiting Potential

Paul William Cleary



Manipulation of Ultracold Bose Gases in a Time-averaged Orbiting Potential

ACADEMISCH PROEFSCHRIFT

ter verkrijging van de graad van doctor
aan de Universiteit van Amsterdam
op gezag van de Rector Magnificus
prof. dr. D.C. van den Boom
ten overstaan van een door het college voor promoties ingestelde
commissie, in het openbaar te verdedigen in de Agnietenkapel
op donderdag 20 December 2012, te 14:00 uur

door

Paul William Cleary

geboren te Dungarvan, Ierland

Promotiecommissie:

Promotor: prof. dr. J.T.M. Walraven

Co-promotor dr. T.W. Hijmans

Overige leden: prof. dr. D. Bonn
prof. dr. H.B. van Linden van den Heuvell
dr. A.P. Mosk
prof. dr. G.V. Shlyapnikov
prof. dr. P. van der Straten

Faculteit der Natuurwetenschappen, Wiskunde en Informatica (FNWI)

ISBN: 978-94-6191-545-0

Cover showing time-of-flight images of a $F=1$ Bose Einstein condensate, center-of-mass motion of an ultracold gas in a TOP trap and a spinning TOP. Design and implementation by dr Antje Ludewig.

The work described in this thesis was carried out in the group "Quantum Gases and Quantum Information" at the Van der Waals-Zeeman Institute of the University of Amsterdam, Science Park 904, 1098 XH Amsterdam, The Netherlands. A limited number of hard copies of this thesis is available there.

A digital version of this thesis can be downloaded from www.science.uva.nl/walraven
This work is part of the research programme of the Foundation for Fundamental Research on Matter (FOM), which is part of the Netherlands Organisation for Scientific Research (NWO).

Contents

Contents	v
Foreword	ix
1 Introduction	1
1.1 This Thesis	2
1.2 Outline	4
2 Experimental Set-up	5
2.1 Introduction	5
2.2 Vacuum System	6
2.3 Optics	8
2.4 2D MOT	11
2.5 3D MOT	15
2.6 Magnetic trap	18
2.6.1 Ioffe-Pritchard quadrupole trap	18
2.6.2 Circuitry	20
2.6.3 Additional coils for axial field control	21
2.7 TOP trap	23
2.8 RF evaporation	24
2.9 Control	25
3 Lasers and Imaging	29
3.1 Laser Systems	30
3.1.1 Master Laser	30
3.1.2 DFB laser	31
3.1.3 Tapered amplifier	33
3.1.4 Implementation and usages of stabilized lasers	37
3.2 Imaging	37

3.2.1	Integration with MOT optics	37
3.2.2	Resolution Tests	39
3.2.3	Image blurring by the atoms	42
3.2.4	Conclusions	43
3.3	Analysis of Imaging Noise	43
3.3.1	Method	45
3.3.2	Camera	46
3.3.3	Reducing the noise	49
3.3.4	Conclusion	52
4	Measurements with long-lived condensates	53
4.1	Introduction	53
4.2	Trapping and condensing the $ 1, -1\rangle$ state	54
4.2.1	Optical pumping scheme	54
4.2.2	Magnetic transfer and evaporative cooling	55
4.2.3	Imaging	56
4.3	$F = 1$ BEC	57
4.3.1	BEC characteristics and lifetime	57
4.3.2	BEC of $ 1, -1\rangle$ atoms in TOP trap	60
4.4	Vortex excitation and detection	62
4.4.1	BEC and vortices	62
4.4.2	Generation of vortices	63
4.4.3	Excitation by rotation in a magnetic trap	64
4.4.4	Vortex detection	65
4.5	Experiments rotating the TOP	66
4.5.1	Results with radial imaging	67
4.5.2	Results with axial imaging	67
4.5.3	Conclusions	69
5	Manipulation using phase jumps of the TOP	71
5.1	Introduction	71
5.2	Theory	73
5.2.1	Time-averaged Ioffe-Pritchard potential	73
5.2.2	Micromotion and macromotion	75
5.2.3	Numerical analysis	77
5.2.4	Phase jumps	79
5.3	Experimental	82
5.3.1	Apparatus	82
5.3.2	Measurement procedure	83
5.4	Analytic Model	86
5.5	Results and discussion	87
5.6	Summary and conclusion	90

<i>CONTENTS</i>	vii
A Quadrupole field with permanent magnets	93
Bibliography	97
Summary	105
Samenvatting	107
Acknowledgements	109

Foreword

Chuireamar ár n-aisling ag snámh mar eala ar an abhainn.

Rinneadh fírinne den aisling.

Rinneadh samhradh den gheimhreadh.

Rinneadh saoirse den daoirse agus d'fhágamar agaibhse mar oidhreachtí.

A ghlúnta na saoirse cuimhnígtí orainne, glúnta na haislinge.

We sent our vision aswim like a swan on the river.

The vision became a reality.

Winter became summer.

Bondage became freedom and this we left to you as your inheritance.

O generations of freedom remember us, the generations of vision.

Liam Mac Uistin

Chapter 1

Introduction

In 1925 a new state of matter was predicted by Einstein [1] following up on the work published the previous year by Bose on the quantized electromagnetic field [2]. Below a certain temperature, the critical temperature for Bose-Einstein condensation T_c , a macroscopic fraction of a non-interacting ensemble of massive particles (called the condensate) occupies the lowest-energy single-particle state [3]. This phenomenon only happens for bosonic particles and persists in the presence of interparticle interactions [4]. Once T_c is reached the ensemble will display quantum mechanical phenomena on a macroscopic scale. The Bose-Einstein condensate (BEC) emerges as the result of a phase-transition at T_c . The critical temperature is density dependent and is reached in three-dimensional gases when the interparticle spacing equals the thermal wavelength. As T_c is approached, the classic picture of individual particles breaks down and the ensemble has to be treated as a quantum many-body system. The presence of interactions modifies the low-energy excitation spectrum of the ensemble and is associated with the occurrence of coherence and superfluidity.

For a long time the only material known to display such characteristics was liquid Helium-4, which below its lambda point becomes a superfluid [5, 6]. Upon rotation, the fluid displays quantized vortices as demonstrated in [7] and discussed in detail in [8]. In this fluid, a macroscopic condensate fraction of up to 11% occurs. As techniques for cooling gases developed, a dilute gas of weakly interacting bosons was considered a possible candidate for a more pure condensate. Following promising results with spin-polarized atomic Hydrogen [9] and key breakthroughs in the areas of magnetic trapping [10], laser cooling [11] and evaporative cooling [12, 13], degeneracy was finally achieved with dilute gases of alkali atoms in 1995 when it was demonstrated in separate experiments at JILA [14] and MIT [15]. In these gases the critical temperature is achieved around 1 μ K.

The first BEC experiment at JILA was done using a time-averaged orbiting potential (TOP) trap. The TOP trap consists of a three-dimensional magnetic quadrupole trap and a rotating modulation field which translates the zero of the quadrupole field. The result is a time-averaged effective trapping potential where the field zero orbits

the center of the effective potential [16]. As long as the sample size is much smaller than the radius of this orbit and the rotation speed is sufficiently fast, this arrangement acts as an efficient trap for spin-polarized atoms in low-field-seeking states. The atoms instantly depolarize upon crossing the field zero and are ejected from the trap. Therefore, the radius of the orbiting field zero is called the "radius of death".

Following the success at JILA the TOP was used in a number of groups to reach BEC [17, 18, 19, 20, 21] and described in several theoretical works [22, 23, 24, 25, 27, 26]. The TOP at JILA was used to imprint the first vortices in a BEC [28] and later by introducing ellipticity to the modulation field of the TOP, vortices were induced in a rotating trap [29, 30]. Variations on the original TOP were also introduced, breaking the axial symmetry to produce a triaxial asymmetric TOP [31, 32, 33] and using alternatives to the spherical quadrupole trap such as optically plugged magnetic quadrupoles [34] and Ioffe-Pritchard traps [35, 36, 37].

1.1 This Thesis

The work presented in this thesis seeks to explore the opportunities and phenomena associated with the use of time-averaged potential fields for the investigation of Bose-Einstein condensates. In our experiments atom samples of ^{87}Rb are trapped and cooled in a static Ioffe-Pritchard trap. This trapping potential is then modified by applying a time-averaged orbiting potential. The Ioffe-Pritchard trap we use was designed to produce large dense ^{87}Rb condensates [38] in a cigar-shaped trapping potential and to study condensation in the hydrodynamic regime [39]. The addition of a TOP provides the opportunity to produce trapping geometries difficult to realize in a static trap. Unlike the quadrupole field, the Ioffe-Pritchard trap has a nonzero field minimum at its center. It was shown in [35], that if this trap minimum is compensated by a bias field then a double-well potential can be realized with a zero field minimum at the center of each well. Adding a rotating modulation field to the Ioffe-Pritchard trap results in a time-averaged potential allowing the achievement of BEC in the double well. Removing the bias field restores the Ioffe-Pritchard trapping potential and causes the two trapped condensates to move to the center of the trap and collide [36, 37].

The question arises as to whether it is possible to rotate the condensate and stir vortices in the Ioffe-Pritchard and TOP trap combination. Experiments involving vortex nucleation require timescales much longer than the lifetimes of the condensates produced previously on this apparatus in the $F = 2, m_F = +2$ state [38, 39]. These are typically performed in the longer lived $F = 1, m_F = -1$ state. Preparation of BEC samples in this state required considerable alteration of the apparatus. Detection of vortices also requires greater resolution and laser stability than was previously available. With these adjustments in place we proceeded to try to stir the condensate. Rotation of the TOP field is done by adjusting the amplitude of the field in one

radial direction so that an elliptical effective radial potential can be created and then sinusoidally modulating the amplitudes in the radial direction so that this elliptical shaped potential can be caused to rotate. This rotating elliptical modulation field can be added to the Ioffe-Pritchard trap in both single- and double-well potential configurations. Using the double well provides the opportunity to combine two condensates which have vorticity. Combination and splitting of condensates containing vortices has previously been shown in a quadrupole-based TOP trap [33].

In our experiments, as in several others [31, 34], condensate samples are prepared in the static trap and later transferred to the TOP. This method was chosen because the use of radio-frequency (rf) induced evaporative cooling is more efficient in a static magnetic trap than in a TOP. The consequences of the switch-on behaviour of the TOP during this transfer is not trivial and leads to a sloshing motion which is not predicted by considering only the time-averaged potential. The major results of this thesis concern the center-of-mass motion of a Bose Einstein condensate in a TOP trap. The atomic motion in the TOP consists of a fast rotating part (micromotion), and a slow oscillating part (macromotion). In the usual description of the motion, the static approximation, the micromotion is eliminated by time-averaging the instantaneous potential over a full cycle of the modulation field. This picture is inadequate to describe the motion of the TOP in realistic situations. Challis et al. [40] showed that the dynamical eigenstates of a degenerate Bose gas in a TOP are given by solutions of the usual Gross-Pitaevskii equation but taken in a circularly translating reference frame, that is, a reference frame the origin of which performs a rapid circular motion but retains a constant orientation. With this insight we model the motion of the atomic cloud in the TOP trap. The micromotion of atoms in the TOP was studied by the Pisa group who characterized this motion in a triaxial asymmetric TOP trap in measurements requiring analysis beyond the time-averaged and adiabatic approximations and demonstrating the handedness of the TOP field rotation [32, 41].

We proceed to show that manipulating the phase of the TOP, the micromotion can be used to influence the macromotion behaviour. The role of the initial phase of the TOP was studied by Ridinger and coworkers [42, 43] for the special case of a one-dimensional rapidly oscillating potential (ROP) with zero average. Ridinger et al. also showed, first for a classical particle [42] and subsequently for the quantum case [43], that the amplitude and energy associated with the slow motion can be altered by applying a suitable phase jump in the rapidly oscillating field. We succeeded in realizing these ideas in a two dimensional oscillating potential in our apparatus. We can produce a sloshing motion in the direction of our choice by choosing the initial phase appropriately. We can also quench this sloshing motion by calculating the correct timing and change in phase for a phase jump. We show this result both theoretically and experimentally for a two dimensional rotating TOP and also add an analytical model explaining the phenomenon.

1.2 Outline

This thesis is a study of the motion of Bose-Einstein condensates in a time-averaged orbiting potential (TOP) trap. In **Chapter 2** the experimental apparatus used to produce the condensates is explained. The vacuum system and magnetic trap were retained in the form described in [38] but acoustically separated from each other. The two-dimensional magneto-optical trap (2D MOT) source was updated by creating the 2D quadrupole field with small bar magnets instead of race-track shaped coils. To increase flexibility the apparatus was modularized with the use of optical fibers, with an overhaul of the optics to supply light for the MOT, optical molasses, optical pumping, and detection of condensates in both $F = 1, m_F = -1$ and $F = 2, m_F = +2$ trappable states. The control system of the apparatus was also updated. The new interface enabled amplitude- and phase-controlled switching of the TOP fields, which was essential for the experiments described in Chapters 4 and 5.

Chapter 3 explores the changes made to the apparatus in the area of lasers and imaging. Lasers were stabilized on side tables disconnected from the main optical table and the power of the stabilized lasers amplified by in-house designed laser amplifiers. The implementation and characterization of the tapered amplifiers is described in detail. These amplifiers were found to be very reliable to boost the optical power, insensitive to disturbances in temperature or vibration. The apparatus was modified to allow imaging along the axis of the cloud to search for vortex lines head-on. This required overlap with the optical pathways for the MOT and for optical pumping. A detailed account is given of the improvements in resolution and signal-to-noise ratio of the imaging system.

In **Chapter 4** we describe how we produce a condensate in the $F = 1, m_F = -1$ state. The properties of these condensates in our Ioffe-Pritchard trap are investigated, measuring the lifetime and inferring a value for the three-body recombination decay rate constant. Condensates are also produced in different types of time-averaged potential fields. Following an overview of methods to induce vorticity in the BEC, we introduce a rotating ellipticity to our trapping potential. We see evidence of rotation but do not find convincing visual proof of the existence of vortices in the sample.

In **Chapter 5** we report on the manipulation of the center-of-mass motion (‘sloshing’) of a Bose Einstein condensate in a TOP trap. We start with a condensate at rest in the center of a static trapping potential. When suddenly replacing the static trap with a TOP trap centered about the same position, the condensate starts to slosh with an amplitude much larger than the TOP micromotion. We demonstrate, both theoretically and experimentally, that the direction of sloshing is related to the initial phase of the rotating magnetic field of the TOP. We show further that the sloshing can be quenched by applying a carefully timed and sized jump in the phase of the rotating field.

Chapter 2

Experimental Set-up

2.1 Introduction

The essential elements of a BEC experiment are a trapped cloud of atoms under vacuum conditions, laser light for optical cooling and trapping, an adjustable form of magnetic trapping, a split-second control system and a detection method of the cloud of atoms. These aspects were in place from a set of three predecessors who developed the existing apparatus [38, 39, 44] and much of this apparatus could be used unchanged or with minor modifications, namely the vacuum system and magnetic trapping apparatus. The optical system required substantial improvement and these improvements are discussed in Chapter 3.

In reaching condensation, a good vacuum is required to ensure that at least some of the atoms which are being cooled to condensation are not heated by collisions with background "thermal" atoms before reaching BEC. In this set-up, the conundrum of desiring excellent vacuum conditions and yet requiring an adequate vapour pressure as a source of cold atoms was solved by using a dual vacuum chamber system [38]. Optical cooling and trapping is performed with resonant frequency-stabilized laser light to form a two-dimensional magneto-optical trap (2D MOT) [45] in the lower vacuum chamber (using bulk optics) and a three-dimensional magneto-optical trap (3D MOT) in the upper (ultra high vacuum) chamber (using an optical fiber distributor). Laser light is then utilized to pump the atoms to states suitable for magnetic trapping. The magnetic trapping is performed in an adjustable Ioffe-Pritchard (IP) trap suitable to cool the atoms by rf evaporation to BEC. The ultra-cold atomic cloud is detected by time-of-flight absorption imaging on to a CCD camera after release from the trap. The experiments are controlled with the aid of a LabView graphics user interface connected to National Instrument input and output cards. The software was running on a regular Windows XP PC.

In this chapter the various components are discussed, with emphasis on changes to the set-up with respect to the previous thesis works on this apparatus. After a description of the vacuum system in Section 2.2 we discuss the various optical

frequencies used in the experiment along with the organization of the optical table (Section 2.3). In Section 2.4 we discuss the 2D MOT system with emphasis on the advantage of the use of permanent magnets for the creation of magnetic field gradients. A complete overhaul of the 3D MOT is presented in Section 2.5. The Ioffe-Pritchard trap and its current supply are introduced in Section 2.6. This is followed by a discussion of the implementation of time-averaged orbiting potentials (Section 2.7) as well as rf evaporative cooling (Section 2.8). The chapter is concluded with an overview of the components used for interfacing in Section 2.9.

2.2 Vacuum System

Vacuum conditions are essential in order to reach Bose-Einstein condensation with a relatively large number of atoms and for this condensate to a workable lifetime. The process of enhancing the phase space density to condensation by evaporative cooling takes about 10 s and another few seconds are needed for the experiments. The required lifetime was realized by separating the source of cold atoms from the measurement region by the use of a differentially pumped dual vacuum chamber system. As can be seen in Fig. 2.1, one vacuum chamber is located directly above the other and there is a channel of diameter 0.8 mm and length 3 mm joining the two chambers. Differential pumping is performed via this channel and allows us to achieve a vacuum of $\ll 10^{-10}$ mbar in the upper chamber and yet have a Rb vapour pressure of 10^{-7} mbar in the lower chamber. The collisional lifetime of trapped atoms due to collisions with background gas in the upper chamber is 50 s. Each of these two quartz chambers is joined to a metal manifold by a pair of viton rubber O-rings and the space between these is pumped by a rotary pump, which greatly reduces permeation through the O-rings (by 6 orders of magnitude [38]). The entire vacuum set-up rests on a breadboard at a height of some 500 mm above of the optical table.

The vapour pressure of rubidium in the lower chamber was created when the first BECs were made in this machine. It was supplied by heating the rubidium reservoir after which the supply valve was closed. Since then rubidium has been in overabundance in this chamber so that there is always a Rb vapour pressure of $\sim 5 \times 10^{-7}$ mbar, the saturated vapour pressure of rubidium at room temperature [46]. The leak rate to the upper chamber via the adjoining channel is calculated to be negligible compared to the controlled flux which will be supplied during measurements.

At the beginning of this work, the entire apparatus was dismantled and transported from the FOM institute AMOLF to the Van der Waals-Zeeman Institute (WZI) of the University of Amsterdam (UvA). During this transport and subsequent storage, for some days the system was not pumped and the quality of vacuum in the UHV (upper) vacuum chamber deteriorated several orders of magnitude. Placing a backing turbo pump (*Balzars*) behind the ion pump, over a period of 48 hours, the vacuum recovered from 9×10^{-6} mbar to 5×10^{-9} mbar as measured on an ion gauge.

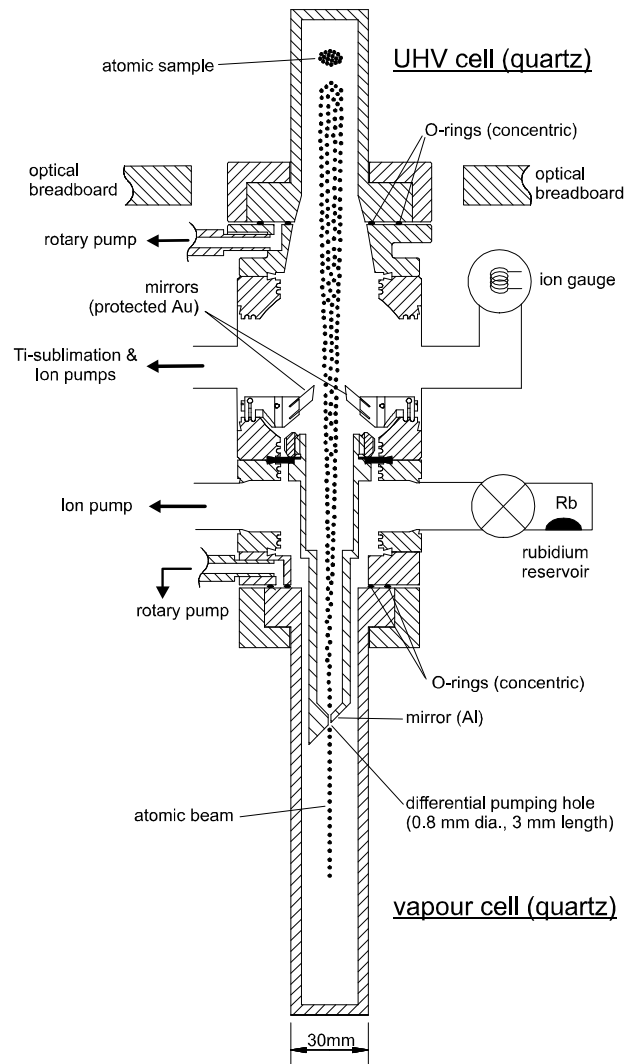


Figure 2.1: Schematic of the vacuum system showing upper and lower vapour cells, the differential pumping hole and all connections to pumps, gauges and the rubidium reservoir.

Both ion pumps were subsequently baked out and over a period of one month vacuum pressure in the upper chamber recovered to 10^{-11} mbar.

While the upper vacuum system was pumped directly by an 40 l/s ion pump (*Varian*) and was connected to an ion gauge (*Varian*), the lower cell was pumped via the differential pumping hole and the O-rings between the chambers pumped by a rotary pump. In the lower cell the rubidium pressure remained at the saturated vapour pressure. However, contamination presumably by air permeating the viton O-rings (during the move when the rotary pump was without power) resulted in an increasing amount of a greyish compound attributed to rubidium hydroxide. This contamination adhered to the windows of optical access of the lower cell reducing transmission at the lower half of the cell, but not affecting the quality of the vacuum. Various attempts were made to remediate this problem. The system was baked out repeatedly up to 135 C. Beyond this temperature the viton O-rings from the cells to the metal manifold tend to malfunction due to thermal deformation and unfortunately this temperature was not high enough to desorb the hydroxide from the glass. Desorption techniques for Rubidium on glass using white light [47] and blue LEDs [48] also failed to remove the hydroxide. In order to avoid a repeat of this contamination situation a valve was placed between the O-rings and the rotary pump.

2.3 Optics

In this section a summary is given of the optical frequencies employed for running the experiment. The relevant optical transitions are indicated in Fig. 2.2. The electronic ground state $5^2S_{1/2}$ of ^{87}Rb has two hyperfine levels $5^2S_{1/2}$ ($F = 1$) and $5^2S_{1/2}$ ($F = 2$) separated by 6.8 GHz. Optical transitions are possible between the ground state $5^2S_{1/2}$ and the first two excited states $5^2P_{1/2}$ and $5^2P_{3/2}$ coupling these levels with what are known as the D1 and D2 lines, respectively. Only D2 transitions are used and indicated in Fig. 2.2. Electric-dipole transitions are allowed between the levels $5^2S_{1/2}$ and $5^2P_{3/2}$ for $\Delta F = F' - F = -1, 0, +1$. The excited state $5^2P_{3/2}$ has four hyperfine levels $F' = 0, 1, 2, 3$ so for the D2 line a total of six hyperfine transitions are possible, three from $F = 1$ and three from $F = 2$. In our experiments we use two of these from $F = 1$ and two from $F = 2$. For locking the frequency of the master laser we use the crossover transition $F = 2 \rightarrow F' = 1, 3$. The lasers are used for the following purposes:

Laser cooling: Laser cooling makes use of near resonant light to reduce the momentum of atoms by the absorption of photons. Each photon carries momentum $E = h\omega$ and so can effect a change of velocity of hk/m on the atom which absorbs its energy. By arranging light beams such that the momentum of an ensemble of atoms is reduced in every direction, the average kinetic energy can be reduced and so the ensemble cooled. This can be accomplished with the aid of the Doppler shift, which

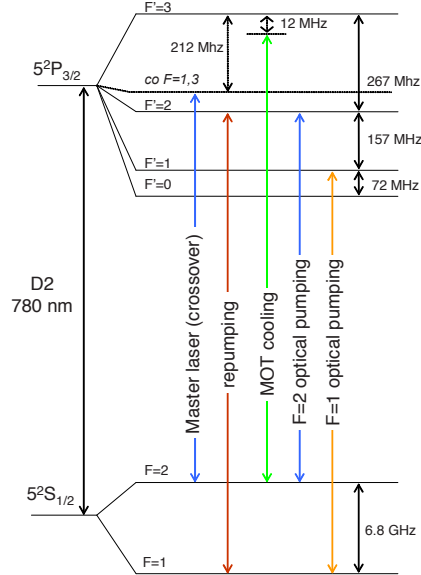


Figure 2.2: Energy level diagram for ^{87}Rb showing the optical transitions and colour coding used in this thesis. Note that the frequency splittings are not drawn to scale.

makes the light force velocity dependent. This type of laser cooling is called Doppler cooling and has a limit known as the Doppler limit. Laser cooling is used here in an optical molasses configuration with laser cooling beams from all 6 directions and in a magneto-optical trap as described in Sections 2.4 and 2.5. A review of laser cooling is included in [11]. To produce a considerable cooling each atom must be excited many times. Therefore, the cooling is performed with light red-detuned from the σ_+ cycling transition $|F = 2, m_F = 2\rangle \rightarrow |F' = 3, m_{F'} = 3\rangle$ of the D2 line (see Fig. 2.2).

Repumping: Because of the relatively small frequency differences of the levels in the $5^2P_{3/2}$ manifold (see Fig. 2.2), atoms in the $F' = 2$ state have an off-resonant probability of being spuriously excited by the cooling light to the $F' = 2$ level from which they can decay to the $F = 1$ ground state hyperfine level. As excitation from the $F = 1$ state is negligible at the cooling frequency, the $F = 1$ state is a dark state in which the atoms are trapped. The trapping is avoided by the addition of a second laser (repumper) on the $F = 1 \rightarrow F' = 2$ transition in order to enable decay back to the $F = 2$ ground state.

Optical Pumping: Resonant light is also used to spin polarize the sample. This is done by optically pumping to one of the desired magnetically trappable states, $|F, m_F\rangle = |2, 2\rangle$ and $|F, m_F\rangle = |1, -1\rangle$. Pumping to the $|2, 2\rangle$ state is done with σ_+ polarized light on the $F = 2 \rightarrow F' = 2$ transition (for which the $|2, 2\rangle$ state is

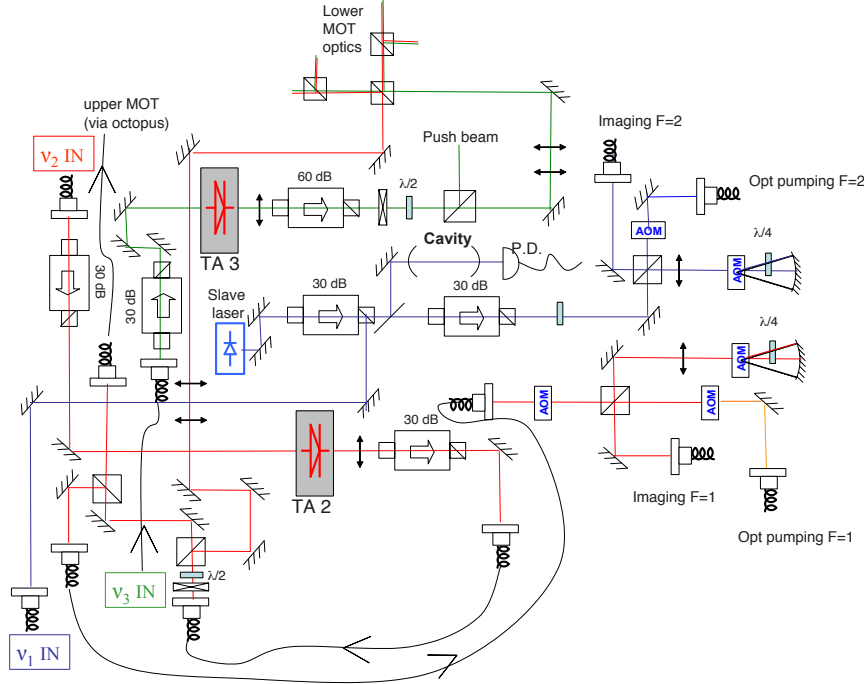


Figure 2.3: Schematic diagram showing positioning of optical elements and light paths and frequencies of laser beams on main table. Incoming fibers 1, 2, 3 carry light stabilized at, respectively, the crossover transition (ν_1 , shown in blue), the repumper frequency (ν_2 , red) and the MOT cooling frequency (ν_3 , green). Light leaves the table to the lower MOT, upper MOT (via octopus), and to both the imaging and optical pumping fibers for $F = 1$ and $F = 2$, respectively.

dark). Similarly, optical pumping to the $|1, -1\rangle$ level is done with σ_- light on the $F = 1 \rightarrow F' = 1$ transition (for which the $|1, -1\rangle$ state is dark). Preparation of the $|1, -1\rangle$ state is discussed in detail in Section 4.2.1.

Detection: The sample is detected using time-of-flight absorption imaging onto a CCD camera after release from the magnetic trap using a closed-cycle transition. The choice of imaging transition for $F = 1$ and $F = 2$ atoms is discussed in Section 4.2.1.

Optical beam delivery For the optical system it was decided to have a complete redesign. The two stabilized master lasers (at frequencies ν_1 and ν_2) were removed from the main table and installed on side tables as part of the modularization of the experiment (see Chapter 3). This greatly improved the stability and reliability of the optical system and strongly reduced the number of optical elements on the

main table. Key to the process of modularization was the use of 4 polarization maintaining fibers to deliver light from laser modules on one of the well-isolated side tables to the main table optical system. The arrangement of the main table is shown in Fig. 2.3. Fiber 1, 2, 3 carry light stabilized at, respectively, the crossover transition (ν_1 , shown in blue), the repumper frequency (ν_2 , red) and the MOT cooling frequency ($\nu_3 = \nu_1 + 200$ MHz, green).

Fiber 1 is used to inject a slave laser similar to that described in [49] monitored by Fabry-Perot cavity. This light at frequency ν_1 is then split at a polarization cube. One part is sent through a fixed-frequency AOM and coupled into a fiber for optical pumping on the $F = 2 \rightarrow F' = 2$ transition at frequency $\nu = \nu_1 - 55$ MHz (dark blue path in Fig. 2.3). The other is sent double pass through an AOM and into a fiber for imaging atoms at the $|2, 2\rangle \rightarrow |3, 3\rangle$ transition. By adjusting the control voltage of this AOM the detuning of the imaging light can be set without losing alignment. Thus we can image $F = 1$ at detunings from -60 MHz to $+20$ MHz relative to the imaging transition at $\nu = \nu_1 + 212$ MHz.

Fiber 2 is used to inject an in-house designed tapered amplifier at frequency ν_2 (TA 2 - see Section 3.1). The amplified light is spatially filtered by a fiber and then split four ways to supply power for (a) repumping the upper MOT (via the *Octopus* fiber distribution system - see Section 2.5); (b) repumping the lower MOT (via solid optics); (c) optical pumping to the $|1, -1\rangle$ state using a fixed AOM ($\nu = \nu_2 - 157$ MHz, orange path in Fig. 2.3); (d) imaging $F = 1$ atoms using a variable double pass AOM. In the latter case we scan between -20 MHz and $+40$ MHz relative to the transition $|F = 1, m_F = 1\rangle \rightarrow |F' = 2, m_{F'} = 2\rangle$ at frequency ν_2 .

Fiber 3 is used to inject a tapered amplifier at frequency ν_3 (TA 3) and combined with repumper light at frequency ν_2 to form the four main beams and single push beam of the lower MOT. A shutter in front of each incoming fiber ensures absolute extinction when the light is not use, greatly reducing stray light and thus increasing the trapping lifetimes of the samples. The absence of frequency stabilized lasers on the main optical table means that acoustic noise caused by these shutters is not a problem. The components on the main optical table are much less sensitive to such noise.

2.4 2D MOT

The ^{87}Rb atoms are optically cooled from room temperature to sub-millikelvin temperatures in a two-dimensional magneto-optical trap (2D MOT) acting as a source of cold atoms. This 2D MOT (the lower MOT) consists of two orthogonal pairs of horizontal light beams and a 2D quadrupole field with its symmetry axis in the vertical direction. Each beam pair consists of two cooling beams of opposite helicity and light for repumping. As the light beams trap and cool the atoms horizontally this results in an vertically elongated MOT cloud. In the vertical direction a beam from below

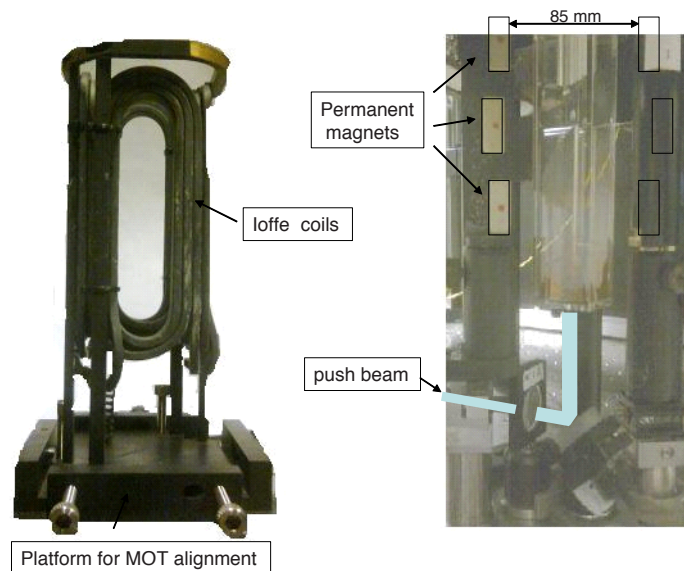


Figure 2.4: Left: old 2D MOT with Ioffe coils. Right: the new set-up with permanent magnets (see Fig 2.5) in the configuration shown in Fig 2.6.

pushes the atoms through the differential pumping channel towards the 3D MOT in the upper vacuum chamber. This channel also acts as a velocity selector for the atoms of the 2D MOT; only atoms with a sufficiently low transverse velocity pass through [45]. The magnetic trap previously used for the 2D MOT consisted of four race-track shaped coils generating the 2D quadrupole field with its symmetry axis vertically along the central axis of the cell. This system pre-existed from previous projects on this machine and was combined with retroreflected cooling beams. This set-up was shown to be a successful rival to alternative sources of precooled atoms such as a Zeeman slower [45]. In view of the contamination of the lower vacuum system mentioned in Section 2.2 it proved to be imperative to use four balanced MOT beams to compensate for the reduction in cell transparency to 70 – 75%. The increased amount of stray light made locating the MOT from a side-on view impossible and this greatly complicated the alignment procedure of the MOT coils. A convenient solution was found by using an alternative and much simpler method of creating a quadrupole field by the use of permanent magnets, see Fig. 2.4. Proof that a 2D quadrupole field can be formed which just two dipoles or bar magnets is given in Appendix A. To produce a 2D quadrupole field which is homogenous over a distance of 5 cm in the

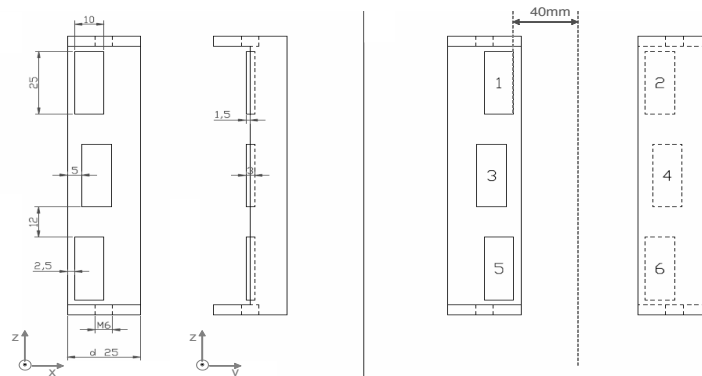


Figure 2.5: Left: diagram of magnet holder showing dimensions and positioning of permanent magnets 1-6. Right: magnet holders are placed opposite to one another to create a quadrupole field with a linear field minimum (see Fig. 2.6).

z direction, we placed a set of three bar magnets on a holder as shown in Fig 2.6. Summing the contributions of all six magnets $n = 1, \dots, 6$ in the arrangement shown in Fig. 2.5 we obtain the total magnetic field at position \mathbf{r} ,

$$B_i(\mathbf{r}) = \sum_{n=1}^6 (-1)^n B_i(\mathbf{r}, \mathbf{r}_n) \quad \text{with } i \in \{x, y, z\}. \quad (2.1)$$

This equation can be used along with the results in Appendix A to calculate the magnetic field close to the axis of the cell.

Measurements of magnets and implementation

The magnetization of the bar magnets was found with the aid of Eq. (A.7) by taking an individual magnet bar of $25 \times 10 \times 3$ mm (*Eclipse Magnetics Ltd.*) and measuring the magnetic field as a function of the distance from the magnet center. The field was measured with a Hall probe (*Honeywell SS490*) calibrated against a precision solenoid carrying a known current. Two individual magnets measured in this way showed good agreement with one another. The value for the magnetization found is reported in [50] as 879 kA/m and lies well within the range of values 850 – 950 kA/m reported in the literature. This value was then used to calculate the field along the z -axis between two assemblies of 3 magnets each. Comparing this calculation to the measurements of the field from each of the three-bar magnet assemblies is shown in Fig. 2.7.

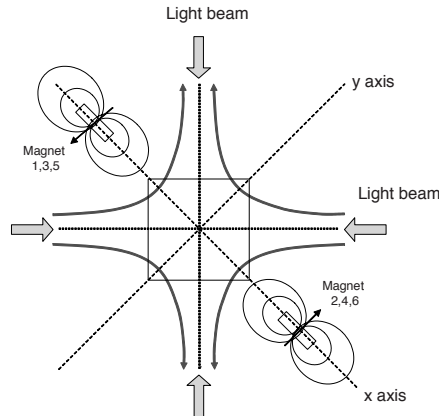


Figure 2.6: Schematic illustration of the 2D MOT arrangement as seen along the vertical symmetry axis of the lower vacuum cell. The solid square shows the orientation of the cell. The magnet sets (1, 3, 5) and (2, 4, 6) are placed on one of the cell diagonals on either side of the symmetry axis. The curved lines show the direction of the 2D magnetic quadrupole field lines close to the axis.

It should be noted that the magnets were tested well beyond the limits of what was required for the experiments. Using the magnet assemblies it was possible to create a quadrupole magnetic field which was constant in the axial direction to within 3% over a distance of 5 cm - similar to the length over which the MOT beams are applied in the vertical direction. The magnet holders were placed on translation stages along the diagonal of the cell and adjusted to 42.5 mm distance from the centre of the cell (see Fig. 2.4) to give a gradient of 23 G/cm. Four beams with 22 mW of cooling light each were combined with 1 mW repumper power and transmitted through the cell using the cylindrical optics to produce elliptical beams as described by Dieckmann [45]. The opposing beams were aligned on top of each other. Precision alignment of the atomic beam was carried out by placing a camera below the cell. This camera was aligned to the axis of the differential pumping channel by shining white light from above. With a clean line of sight in place, the 2D MOT was then aligned to the bright spot from the top using the translation stages of the permanent magnet holders. Using this method a beam of atoms to the upper MOT could be established albeit with a low flux (10^7 atoms per second) as measured by capture in the upper (3D) MOT. This flux could be tweaked with the translation stages but a substantial increase in flux was found only after the installation of a push beam from the bottom of the cell, also taken from the trapping light of TA 3 (see Fig. 2.3). This beam was reflected via a mirror at 45° to the vertical located directly below the cell (Fig. 2.4) but allowing enough space between mirror and cell to fit the pinhole camera to check alignment.

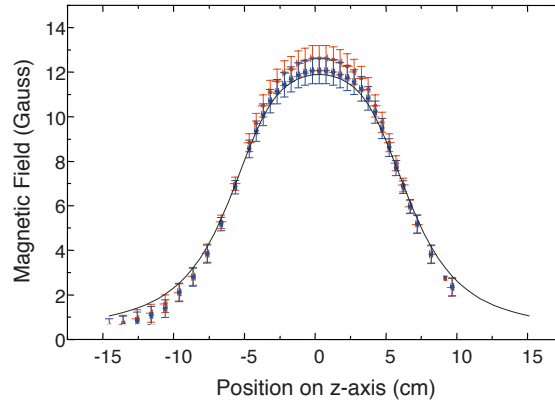


Figure 2.7: Measurements of magnetic field from each of the magnet sets (upper and lower points) at a distance of 4 cm from the magnet edge (see Fig. 2.5), along the long axis of the cell (z -axis) showing homogeneity over a distance of 5 cm. The mismatch in the wings of the distribution may be due to small measurement errors with the Hall probe.

The push-beam increased the flux to 5×10^8 atoms per second and the loading time of the 3D MOT reduced to about 5 s comfortably increasing the repetition rate of experiments. The flux was found to be maximal at a detuning of 12 MHz to the red of the cooling transition in zero field. The quadrupole field drops rapidly with distance and the permanent magnets had no noticeable effect on the performance of the 3D MOT or the experiments described in this thesis. Permanent magnets were also successfully used in our laboratory for 2D MOT of other species such as K and Li [51].

2.5 3D MOT

The cooled atoms from the 2D MOT which pass through the differential pumping channel are then captured in a 3D MOT. This MOT consists of a set of six beams which overlap at the zero of a 3D magnetic quadrupole field. The quadrupole field is provided by the pinch coils of the Ioffe Pritchard trap (to be described in Section 2.6). This combination produces a spherically shaped cloud which is trapped and cooled in all directions and appropriate for transfer into a magnetic trap such as the Ioffe Pritchard described below.

The magnetic part of the upper MOT was left unchanged from the work in previous theses. The optical part of the upper MOT by contrast was completely re-designed to allow the integration of the optical detection system with the MOT (see Section 3.2). This caused new restrictions on the space available for the MOT optics,

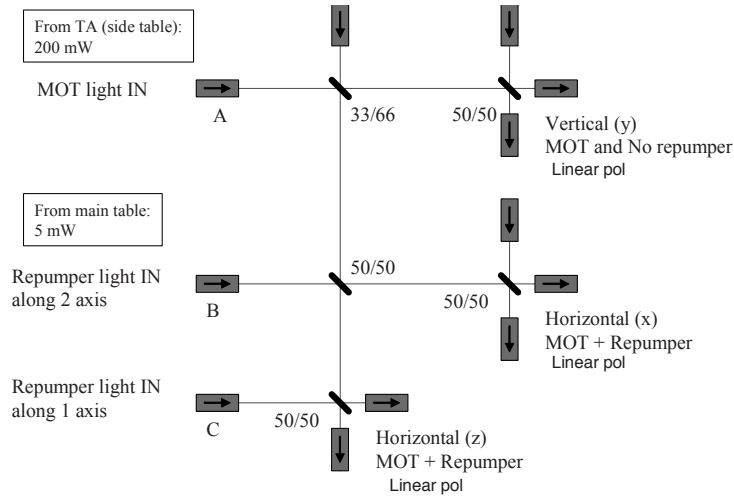


Figure 2.8: The 6-in 6-out fiber distributor or octopus (3 inputs unused) allows beams from different modules to be easily combined and the polarization to be controlled as well as acting as a spatial filter for our MOT beams.

which were satisfied with the introduction of a fiber distribution system from Canadian Instrumentation and Research Limited (*CIRL*), the "octopus" (see Fig. 2.8). This consisted of 6 fiber inputs and 6 outputs and provided an increase in flexibility and convenience as well as savings in space in comparison with the previous bulk optics based system. The distribution system is based on polished evanescent wave couplers. These couplers bring the cores of two fibers close together with their polarization axes aligned, removing part of the cladding and optically contacting the polished faces. The two cores then behave as if they are contained within the same cladding and coupling from core to core occurs by evanescent wave. The fibers show low loss and back-reflection and are thermally stable. We found that 67% of the light coupled into the octopus at port A was outcoupled from the 6 fibers and that polarization loss as measured with polarization cubes was less than 1% as limited by the cubes. Stability was found to be one part in a thousand over tests lasting several minutes, going up to two parts in a thousand under physical pressure and five parts in a thousand when heated over 40 C. The system had active temperature stabilization via a thermocontrolled array, model 928T (*CIRL*), and longer time polarization drifts were found to be negligible in the temperature controlled environment of the lab.

Implementation

Adversely, the heads of the fibers were found to be very sensitive to contamination by airborne particles. Outcoupling is readily reduced by 20% or more due to such

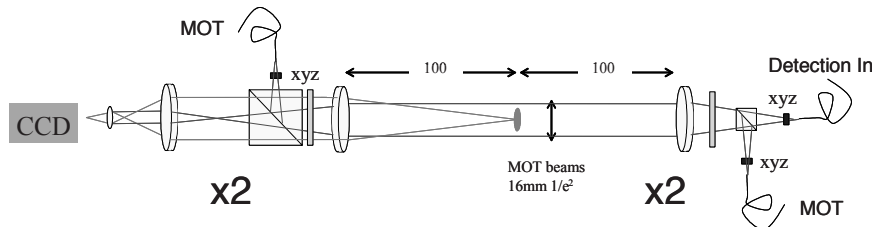


Figure 2.9: Sketch of integration of MOT and imaging optics in horizontal plane. MOT and imaging beams enter the upper vacuum cell via the same 100 mm focal length lenses.

incidents and since the MOT beams form pairs which need to be carefully balanced to maintain the position of the MOT this was a very disruptive feature. Once such an imbalance was observed the fiber heads needed to be polished with a fiber polishing kit (*Thorlabs*) to regain performance. Even slight imbalances caused changes to the position of formation of the MOT, and particularly to the position of the optical molasses, inhibiting accurate transfer to the magnetic trap. Alignment was thus very important and so each fiber was situated in a XYZ translation stage (*Siskiyou*).

By making the housing of the fiber rotatable without coupling to translation, it was possible to also balance the powers of opposing beams. This worked because rotating the fiber head rotates the polarization of the outcoupled beam and in combination with the polarization cube in front of the fiber head (see Fig. 2.9) this rotation thus corresponds to varying the power of the beam after the cube.

The four beams in the plane of the optical table were located on separate modules which could be unclamped from the table and separately inspected and aligned. Each module produced a collimated beam of 25 mm diameter at a height of 37.5 mm and the opposing beams could then be aligned by moving the entire module. Aligning the beams in the vertical direction was a particularly cumbersome process and is best understood by considering Fig. 2.10. Due to the small size of the internal gold mirror it was not possible to use collimated beams as in the four horizontal beams, so the divergence of the vertical beams had to be matched as well as possible.

The performance of the 3D MOT was monitored in a number of ways. Its shape was imaged at an angle of 30° with respect to the horizontal MOT beams with a firewire camera (*Imaging Source*). Position was monitored on a screen via a pinhole camera from above. The fluorescence power was measured by imaging the MOT onto a DET 110 photodiode (*Thorlabs*). These diagnostics warned of slower loading times, beam misalignment or lasers out of lock. In combination with the 2D MOT with push beam the upper MOT was found to load in 5 s. Its stability was found to depend critically on alignment, particularly at higher atom numbers where exact alignment can lead to a pulsing behaviour. The power used was 20 mW per beam of cooling light at a detuning of two linewidths (12 MHz) and about 1 mW of repumping light.

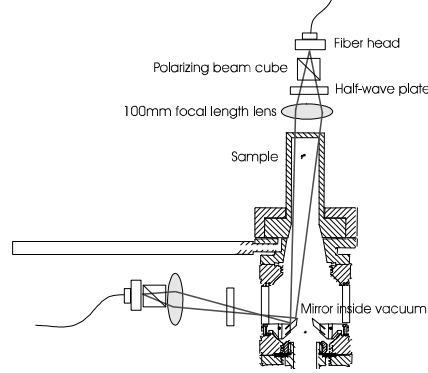


Figure 2.10: Vertical MOT beams are reflected on a gold mirror inside the vacuum chamber at an angle of 40 degrees to the horizontal. This mirror is 1 cm in diameter. The beam from below must be slightly divergent to match the size of the horizontal MOT beams at the location of the sample.

2.6 Magnetic trap

The magnetic trap surrounds the upper vacuum cell with two sets of circular coils (the smaller pinch or axial coils and the larger compensation coils) and four radial racetrack shaped coils. This set-up is shown in Fig. 2.11 and has been described in detail previously [38]. It cleverly provides trapping for both the Ioffe-Pritchard (IP) trap and the upper MOT.

2.6.1 Ioffe-Pritchard quadrupole trap

This geometry is known as a Ioffe-Pritchard quadrupole trap. The quadrupole field is produced by the straight bars of the race-track shaped Ioffe coils creating a field which rises linearly with distance from the central axis with gradient $\alpha = 3.53$ T/m at full current. The field produced by the curved parts of these coils cancel to good approximation on the symmetry axis. The axial confinement is given by a pair of round pinch coils which produce a largely quadratic field with a curvature of $\beta = 266$ T/m², measured at full current. A second pair of axial (compensation) coils are at greater distances from the center of the trap and compensate the offset magnetic field from the pinch coils leaving a tunable residual trap bottom B_0 of about 10^{-4} T depending on the current. This combination produces a cigar shaped trap with the potential at distance $\rho \ll \alpha/\beta$ from the symmetry axis given by:

$$U(\rho, z) = \mu\sqrt{\alpha^2\rho^2 + (B_0 + \frac{1}{2}\beta z^2)^2}, \quad (2.2)$$

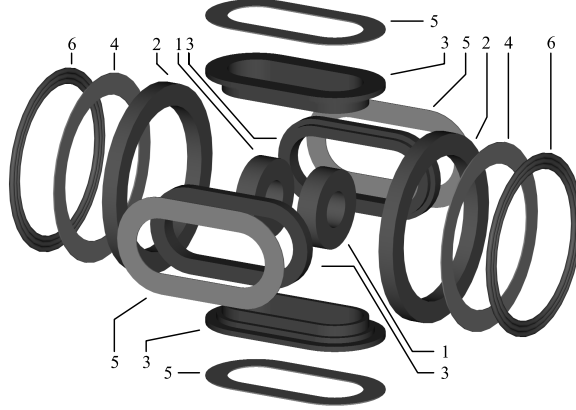


Figure 2.11: Schematic (exploded) of the various coils used in the experiment: Pinch coils (1); compensation coils (2); and Ioffe coils (3) together form the Ioffe Pritchard trap. The additional coils axial PCB coils (4) TOP coils (5) and Axial wire coils (6) were added to the IP trap to provide additional functionality.

where $\mu = g_F m_F \mu_B$ is the magnetic moment of the atom. Taking a harmonic approximation gives the trapping frequencies

$$\omega_\rho = \sqrt{\frac{g_F m_F \mu_B}{m} \left(\frac{\alpha^2}{B_0} - \frac{1}{2} \beta \right)} \quad (2.3)$$

and

$$\omega_z = \sqrt{g_F m_F \mu_B \beta / m} \quad (2.4)$$

for the radial and axial directions, respectively. It should be noted that because the magnetic moment μ is proportional to the m_F number, atoms in the $|1, -1\rangle$ level are trapped a factor of $\sqrt{2}$ less tightly than in $|2, 2\rangle$. Typical values of B_0 are about 1 G, giving a confinement which is far tighter at full current in the radial direction than in the axial direction. The confinement increases as B_0 is reduced, with the harmonic approximation breaking down at $B_0 = 0$ where the trap becomes linear in the radial direction. The adjustable current through the compensation coils also gives the option of $B_0 < 0$ which leads to a trap with two minima (see Fig. 2.13) exploited in [35]. The axial symmetry assumed above is broken by the acceleration due to gravity in the vertical direction. In the harmonic approximation, the main effect of this is a displacement Δy in the vertical direction of the minimum of the potential. The size of this displacement can be simply estimated by equating the potential energy in the trap

$$U = m\omega^2 y^2 - mgy \quad (2.5)$$

to that of the shifted potential without gravity

$$U_{eff} = m\omega^2(y - \Delta y)^2 \quad (2.6)$$

giving a shift of

$$\Delta y \simeq g/\omega^2. \quad (2.7)$$

2.6.2 Circuitry

The circuit which allows the versatility to switch between upper MOT and Ioffe-Pritchard trap is shown in Fig. 2.12. The current through the coils is provided by three Hewlett-Packard HP 6681A power supplies whose current and voltage are controlled via analogue outputs from the control system described in Section 2.9. The current through each path A-E is controlled by circuitry based on IGBT switches (*IXYS*, model *IXGN200N60A*). These allow for ramping of currents using the gate voltage of the IGBTs or quick switching on a timescale of 50 μ s in combination with the diodes D1-D6 and capacitors C1 and C2.

With path A and C open, power supply A gives current to both pinch coils in the same direction, while B and C give double the current to pinch 1 only, but in the opposite direction to A to form an anti-Helmholtz configuration creating the quadrupole field of the MOT (see Section 2.5). The MOT stage was performed with 40 A in the axial coils.

Using path E instead of path C (*i.e.* simultaneously opening the MOT IGBT and closing the Ioffe coils IGBT) runs current through all power supplies and coils in series, changing the pinch coils to Helmholtz configuration and giving the Ioffe Pritchard field geometry (see Section 2.6.1) created by the Ioffe coils in the radial directions and pinch coils and compensation coils in the axial direction. This switch could be made in 300 μ s. Switching off the Ioffe coils from full current (400 A) before imaging occurred in 60 μ s. Path D via the Ioffe bypass IGBT allows one of the Ioffe coils to be bypassed, the lower coil in the vertical direction. This can be used to counteract the influence of gravity which can shift the axis of the trap in the vertical direction.

During the compression stage the currents of the power supplies were ramped up to the full 400 A of the power supplies. The coils are all water-cooled, as is the control unit consisting of the banks of IGBTs and diodes. Adjusting the gate voltage to the IGBT for the application of ramps from fully open to fully closed allows smooth changes in trap geometry such as compression of the trap. These switches are not designed for longer operation or higher currents at intermediate gate voltages and it was essential that, for instance the single IGBT Ioffe bypass was not used for long and that its gate voltage was quickly ramped down as currents were ramped up during compression. Glitches and errors in routines meant that this was not always the case and IGBTs were sometimes destroyed.

Due to a lack of exact replacements of these IGBTs it was necessary to replace some with switches of lower current rating and the magnetic trap loading routines had to be altered accordingly. In the case of the Ioffe bypass IGBT, the original functionality could not be maintained as the replacement IGBT, could not maintain the current sent through path D (see Fig. 2.12) during the transfer from MOT to magnetic trap. This severely impacted the process of transfer, making it a much more delicate process. This bypass ensured that the vertical position of the MOT in the center of the trap coincided with the position of the axis of the IP trap. Without this possibility the MOT had to be released at a position above that of the subsequent axis of the IP trap and then allowed to free-fall the required amount of time so that when the IP trap was turned on, the cloud had fallen to precisely the center of the trap. Failure to time this correctly resulted in a sloshing motion in the trap, heating and consequently atom loss.

A number of positive upgrades were made to the experiment upon re-installation of the magnetic coils in order to mitigate some known problems. Firstly, in its previous incarnation at AMOLF, the magnetic trap when switched off, was observed to make a large acoustic disturbance which propagated via the main table to the stabilized lasers and via the bread board to the imaging optics. Secondly, the mounting procedure of the magnetic trap around the quartz cell was lacking control, which meant it was a very precarious task to install or remove the magnetic trap without damaging the quartz cell. The first problem was solved by supporting the coils from the same platform as the vacuum system, whereas all optics were mounted on a separate breadboard. The second problem was solved by installing a guiding structure for vertical adjustments using tightly fitting sliders on support legs.

2.6.3 Additional coils for axial field control

In addition to the main high current coils of the magnetic trap describe above, three sets of coils were added to the trap and used in the experiments here. All are shown in Fig. 2.11. In the axial direction a set of round PCB coils are mounted directly on the compensation coils used to trim the field. Mounted on these PCB coils are an additional set of axial coils consisting of 10 turns of 2 mm diameter copper wire. These were used to adjust the trap bottom B_0 dynamically in some of our experiments. They can produce fields up to 40 G but have relatively slow switching times. A set of four racecourse – shaped PCB coils were also mounted on top of the Ioffe bars. These coils have a function crucial to the experiments described in this work, creating a time-averaged orbiting potential (TOP) and are described in the following section.

Another set of extra coils was used to compensate the effect of the earth's magnetic fields. The entire cell assembly was placed inside a standard six coil earth field compensation cage, providing fields of the order of a few Gauss at the center of the trap with excellent homogeneity over the size of the cloud. This coil system was primarily used to cancel stray magnetic fields. It was also found to be useful to apply

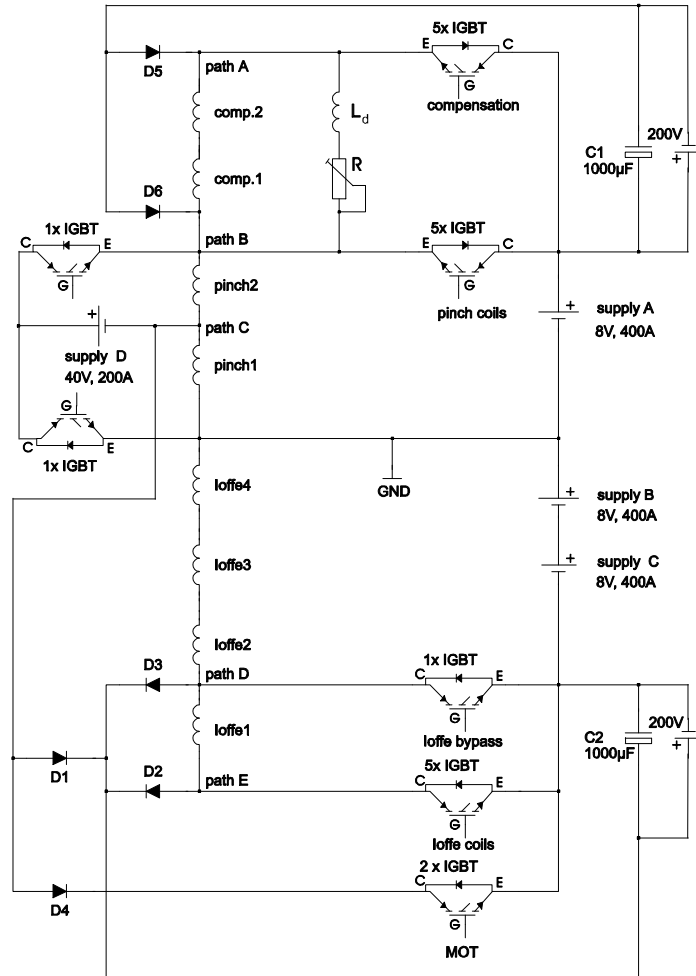


Figure 2.12: Control circuit set-up of magnetic trap. Paths A and C are used during the MOT stage. All coils run in parallel during magnetic trapping with paths A and B determining the axial confinement and offset. The external power supply D with accompanying IGBTs are not used.

homogeneous fields during optical pumping and imaging to provide the desired axis of quantization.

2.7 TOP trap

The time-averaged orbiting potential or TOP trap is a method employed to avoid Majorana losses in traps with a zero trap bottom and was used in the first experimental realization of BEC [14]. A bias field shifts the minimum of the potential away from the center of the trap where the atoms are located. Before the atoms can move to this new trap bottom, the minimum point is moved by rotating the bias field quickly about the center of the original trap at a radius dependent on the size of the bias field. This rotating bias field is known as the TOP field and the radius at which the trap minimum is rotated is known as the radius of death. The atoms remain trapped if the size of the cloud is significantly smaller than this radius and the rotation frequency of the TOP field is much larger than the trap frequencies of the original potential. In the latter case the resulting effective potential can be calculated by taking a time average of the combined potential. The minimum of this effective potential in general does not coincide with the minimum of the instantaneous potential.

In previous work on this apparatus the coils denoted as TOP coils in Fig. 2.11 were used to add time-averaged fields to the Ioffe Pritchard trap in order to create a double trap potential [35]. The TOP coils are connected pairwise in series to produce two orthogonal near-homogeneous fields perpendicular to the trap axis. They consist of just 2 windings so that they have a low inductance and can be switched quickly on a microsecond timescale. The field produced by such a PCB coil pair provides a field with a magnitude of 0.221 GA^{-1} and is supplied with currents up to 5 A.

In the case of the Ioffe-Pritchard trap used in these experiments, the addition of the TOP modulation field B_m to a Ioffe Pritchard trap with $B_0 < 0$, shifts the double zero-points of the potential away from the atoms and ensures that Majorana losses in the double well trap are minimized [35]. The resulting effective potential is shown on the bottom row of Fig. 2.13. Plot (e) of this figure shows the effective double wells in the axial direction while plot (f) shows both the instantaneous potential (dotted line) and effective potential (solid line) in the radial direction.

For $B_0 > 0$, the addition of a TOP field also leads to an effective trap potential with a higher effective trap bottom $\bar{B}_0 = (B_0^2 + B_m^2)^{1/2}$ and a lower radial trapping frequency than the instantaneous potential corresponding to the Ioffe-Pritchard trap

$$\Omega_\rho = \sqrt{\frac{\mu\alpha^2}{m\bar{B}_0} \left(1 - \frac{1}{2}B_m^2/\bar{B}_0^2\right)}. \quad (2.8)$$

These expressions are derived in Chapter 5. It can be seen from Eq. (2.8) that the effective radial trap frequency is dependent on the amplitude of the TOP field B_m . An elliptical effective potential can be created by applying different field strengths

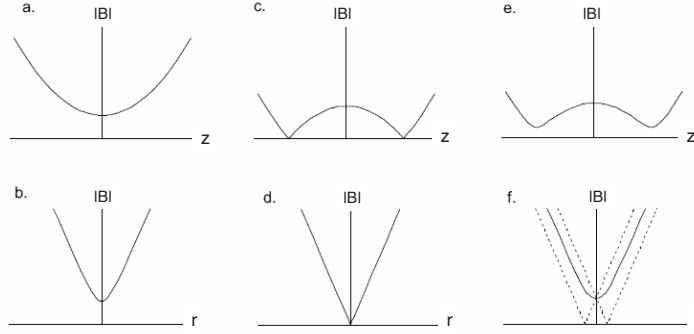


Figure 2.13: Trapping geometry of the Ioffe Pritchard trap in the radial (lower) and axial (upper) directions. From left to right the plots show the situation for $B_0 > 0$, $B_0 < 0$ and $B_0 < 0$ with the addition of the TOP trap ($B_m \neq 0$).

in x and y directions, breaking the radial symmetry. A time variation in B_m will produce a non-constant effective potential. By adding a rotating elliptical TOP field, the total effective potential also takes the shape of a rotating ellipse and thus the cloud can be stirred about the z axis.

2.8 RF evaporation

The standard method to cool a quantum gas that is confined in a magnetic trap to the degeneracy temperature is to use radio-frequency (rf)-induced evaporative cooling. The principle of this cooling method is simple: the rf-field causes transitions from trapped to untrapped states by inducing spin flips. These flips occur only at positions in space r where the magnetic field $B(r)$ corresponds to the resonance value of the rf field given

$$\hbar\omega_{rf} = \mu_B g_F |B(r)|, \quad (2.9)$$

where ω_{rf} is the frequency of the rf field applied. This allows the preferential removal of higher energy atoms which are located higher in the potential. Following each removal of atoms, rethermalization via collisions must be possible so that the ensemble of atoms can reach a lower temperature as a consequence. The RF field also effects the magnetic trapping potential so that the effective trap frequencies are reduced. This process is known as the dressed state potential. In our experiments, as the RF frequency is ramped down so is the RF power so that we avoid the problem of significant rf dressing with the result that our trap bottom is within 5–10 kHz [44] of the value which removes all atoms. The total time of the evaporation became slightly longer because of this, taking a total of up to 15 s to reach the trap minimum (see

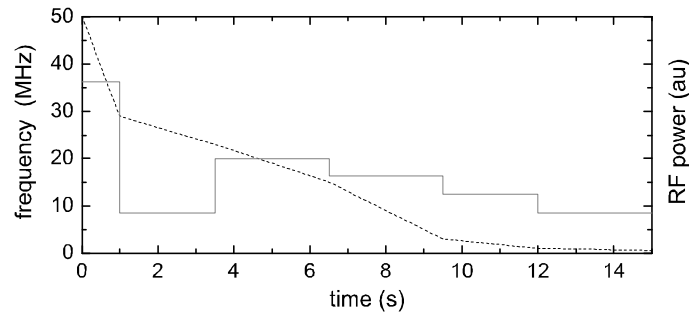


Figure 2.14: Typical RF evaporation sequence showing ramp down of DDS frequency (dashed line) and power via voltage controlled attenuator (solid line). Between 29 MHz and 23 MHz, the speed of rampdown is slowed and power attenuated as required by a resonance at this frequency. The power is again ramped down near the final frequency to avoid complications of RF dressing.

Fig. 2.14). The RF (radio-frequency) coil has a diameter of 31 mm and is located between the axial coils of the IP trap (as shown in Fig. 2.11) at a distance 16 mm from the center of the cloud. The current to the coil is controlled by an Agilent DDS from the control rack shown in Fig. 2.15. This produces a frequency with constant voltage which can then be attenuated by an inhouse designed voltage controlled attenuator (VCA) and amplified by Amplifier Research broadband 25 W amplifier with a range from 250 MHz down to 10 kHz, ideal for our purposes. To produce an arbitrary ramp, the DDS is sent a signal which controls the frequency and the VCA a control for the amplitude. A strong resonance was found for RF in the range 4–4.5 MHz about 14 dB higher than surrounding frequencies. This resonance is possibly a mutual inductance effect with the magnet trap [38] and was dealt with by adding extra attenuation at this stage of frequency sweeps (see Fig. 2.14).

2.9 Control

Our experimental control system consists of three levels centered on a PXI 1006 18 slot chassis from National Instruments and was developed entirely at the FOM institute AMOLF. A PCI-MXI-3 card is located in the personal computer and a PXI-MXI-3 card is placed in the chassis. Communication between these cards is made via fiber optic cable. A further 12 slots of the chassis are occupied, with four slots taken by PXI DIO64 (viewpoint systems) cards with Labview interface software providing digital outputs, seven analogue output devices NI 6713 and one analogue input device NI PXI-6070E. Each of these cards is in turn connected to the signal condition rack; a 19 inch rack with various functionality. Two of the digital PXI DIO64 cards are

used to supply a total of 4 banks of digital outputs at TTL level; another is used for a bank of shutter drivers (higher voltage) and the last supplies a pair of DDS systems. The NI PXI-6713 card is a 12-Bit, 1 MS/s (mega-samples per second) per channel analogue output board used for unipolar and bipolar control voltages up to 10 V or in one case to give out preprogrammed waveforms. The NI PXI-6070E is a 12-Bit, 1.25 MS/s 16 analogue input multifunction DAQ card and was used for monitoring purposes and occasionally for simple feedbacks to the Labview software.

This control system was responsible for executing the experimental sequence. The cards are run with MXI software for windows on the control PC. The program Measurement and Automation explorer (MAX) provides access and troubleshooting capability to the devices, which can then be controlled with Labview software. There was in addition a card for image acquisition via WinView and image taking was also integrated in the Labview program. Getting all these boards to run in parallel and produce the 250 or so outputs necessary to make each BEC required careful assignation of individual IRQs and DMAs to prevent conflicts caused by sharing. In order to maximize the number of IRQs, all but one USB slot of the personal computer was disabled. In addition it was necessary to run NI-DAQ (traditional) data acquisition software alongside the newer NI-DAQ to deal with the differing generations of components. This prevented the classic communication error "not handshaking" from reoccurring.

A dedicated Labview software state engine also written at the FOM institute AMOLF was capable of running all events of the experiments so that no development of software was required during the period of the experiments. The experimenter had only to devise a timeline which could be set to carry out all the actions necessary for each experimental run. Once the timeline has been executed the experimental data takes the form of a cloud absorption image (see section 3.2). Image manipulation and conversion as well as subsequent data analysis was carried out on a Linux machine using open-source software and routines adapted from those employed on neighboring experiments [49]. The Linux operating system greatly simplified batch processing and had the added advantage of allowing remote data analysis of images.

The control system also facilitated the adaptability needed to control the current through the TOP coils as shown in Fig. 2.15. Signal multiplier boxes were designed inhouse based on the Ad835AN chip, a 250 MHz, Voltage Output 4-Quadrant Multiplier from Analog Devices. A pair of these multipliers were used to multiply the fast frequency output of two synchronized Hewlett-Packard 3310 function generators with the slow frequency outputs of a Krohn-Hite model 4024 oscillator and add the outcomes in order to create a rotating elliptical potential (see Chapter 4). The amplitudes of the signals was controlled via analogue outputs of the signal conditioning rack while the triggering of the function generators was controlled via the TTL outputs of the rack. In another set of experiments the multipliers were combined with a TTI 4 channel arbitrary wave generator to produce jumps in the phase of the TOP (see Chapter 5). This was done by assigning two channels of the synthesizer to each

coil pair and setting a given phase difference between the channels. The TTL outputs of the signal condition rack were then using to simultaneously switch channels for both directions, giving a near instantaneous phase jump in both directions.

Chapter 3

Lasers and Imaging

In this chapter a description is given of the improvements of the laser and imaging systems in preparation for the experiments described in this thesis. These improvements were driven by new requirements on the power and stability of the lasers and the necessity of imaging along the cloud axis. Further, to facilitate detailed imaging and better analysis of the atomic clouds, greater position resolution and improved signal/noise were imperative.

An improved laser stabilization was required to realize a better shot-to-shot reproducibility in absorption imaging. For this purpose a stable sub-1 MHz linewidth external cavity diode laser (ECDL) stabilization was developed using Zeeman sideband spectroscopy. New higher powered laser systems were needed as a result of the decision to put all stabilized lasers on separate optical tables in order to decouple them from the sources of acoustic vibration caused by switching of trap currents and various shutters on the main table. This decision also allowed a very flexible mode of operation in which improvements could be developed alongside an operational system on the main table. To enable this approach insertion losses caused by the optical fibers bridging the optical tables had to be compensated. For this purpose tapered amplifiers were introduced in the system and a temperature stabilized mount was developed inhouse to make best use of the increased laser power. For the less critical purposes, such as optical pumping and repumping, a distributed feedback laser (DFB) was found to be a conveniently suitable alternative. The lasers were situated on two side tables, one containing the DFB laser and the other the ECDL master laser and tapered amplifier (TA). All optics on the side tables were enclosed in a metal casing thus avoiding stray light, thermal fluctuations and air turbulence disturbances to experiments.

The detection and imaging system was adapted to image both along the axis of the cloud and perpendicular to the cloud in order to investigate structure in the condensate introduced when rotating the cloud about its axis. This required a new system for absorption imaging, which again was cast in a modular concept. The new imaging directions overlap with the paths of the MOT beams and so required

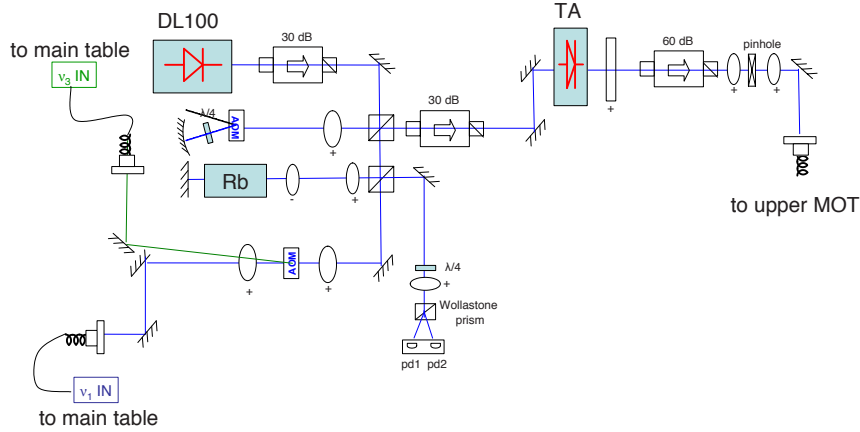


Figure 3.1: DL100 master laser with tapered amplifier. The master laser is stabilized using modulated zeeman spectroscopy in Rb vapour. Light is sent at two frequencies ν_1 and ν_3 to the main table and also as seed to the tapered amplifier (TA) where it is amplified to up to 1 W and via a telescope coupled into the fiber distributor (octopus) of the upper MOT.

an overhaul of all optics about the upper cell to integrate the imaging optics with those of the MOT. Researching the best way to proceed with this integration lead to several insights into the operation of the camera and key properties of detection such as optical resolution and signal to noise optimization. Polarization maintaining optical fibers were employed for their advantages of compactness and well-defined polarization. Investigating the performance of the imaging system, gains were also made in both optical resolution and imaging noise reduction with the aim of allowing finer detail examination of the clouds than was hitherto possible on this system. The limiting components for both resolution and imaging noise were identified and replaced resulting in better resolution and a signal to noise ratio.

3.1 Laser Systems

3.1.1 Master Laser

The master laser for this experiment is locked to a crossover line of the D2 transition and is based on a higher power version of the DL100 laser (*Toptica*). The locking system uses Zeeman sideband spectroscopy, explained at length in [52] and mentioned in [44], with some improvements here to help stability. The optical paths of the setup is shown in Fig.3.1. Linearly polarized light is retroreflected through a small Rb-vapour saturation spectroscopy cell located between two coils connected in series in Helmholtz configuration (not shown in the figure). The current to these coils is

modulated creating an AC magnetic field in the cell.

The Rb atoms in the cell can make σ or π transitions by absorbing photons from laser light at the transition frequency creating a dip in the transmission of the light through the cell [53, 54]. In the presence of a magnetic field the σ^+ and σ^- transitions become non-degenerate and are frequency shifted in opposite directions proportional to the magnetic field due to the linear Zeeman effect. Thus the dips in the transmission of the light through the cell with a modulated magnetic field become frequency modulated just as if the laser light itself were modulated. This induces sidebands on the light through the cell without having the sidebands on the light directly from the laser. A combination of a Wollastonite prism and a $\lambda/4$ plate allow σ^+ to be detected on one photodiode of a high speed differential detector and σ^- to be detected on the other. The combined (differential) signal is then amplified and multiplied on a mixer with the drive frequency of the coil current to produce a DC error signal which can be converted to feedback to the grating and power supply of the laser. The signal from a single photodiode could in fact be used individually to lock the laser but subtracting the two allows us to cancel laser noise as well as reducing greatly the effect of external magnetic fields, increasing stability [52].

Additional stability was gained by shielding the cell from external magnetic fields with a soft iron mount. The error signal is sensitive only to noise in a narrow band at the specific drive frequency. The result is a laser which can be stabilized to well below 1 MHz as measured by beat experiment between two such lasers. It shows excellent isolation from magnetic, electrical and vibrational noise but without creating sidebands on the laser as in other modulation methods.

This stabilization method is used for the imaging laser. Following amplification and additional detunings imparted with acousto-optical modulators (AOM) it also used for magneto-optical trapping and optical pumping. As can be seen in Fig.3.1, a part of the beam is double passed through an AOM and sent as seed laser to the tapered amplifier (TA) which produces the upper MOT. A second beam goes to the main table at the crossover frequency ν_1 and a third at frequency ν_3 corresponding to a detuning of two linewidths (12 MHz) from the $F = 2 \rightarrow F' = 3$ transition.

3.1.2 DFB laser

The distributed feedback laser (DFB) is a 50 mW GaAs semiconductor laser diode with an integrated grating structure. For applications not requiring sub-natural linewidth accuracy in wavelength, the DFB laser was a useful tool introduced to the apparatus. The main advantage over the external cavity diode is that instead of an external grating, the DFB incorporates a grating into the active region of the semiconductor, which then via Bragg scattering provides optical feedback to the laser. By construction it is made near single mode in frequency (highly favouring modes in a narrow region). This is done by concatenating two such gratings, thus in effect creating a periodic structure with a phase change in the middle. The incorporated grating

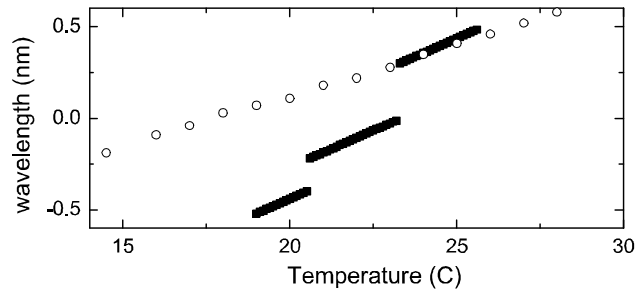


Figure 3.2: Comparison of mode behaviour of DFB (open circles) and EDCL (solid squares). Temperature was varied from 14-40 C and detuning from D2 line of ^{87}Rb plotted. Note the continuous wavelength property of DFB laser shows no modehops over a 15 C temperature change while the EDCL is stable over about 4-5 C and makes large mode hops.

makes the DFB laser very insensitive to sources of acoustic noise. Wavelength tuning is realized by altering the refractive index of the semiconductor by changing the temperature or the operating current. Changing the temperature causes, via thermal expansion, a change to the bandgap of the semiconductor and hence also to the refractive index of the grating. This in turn causes a change to the pitch of the grating and thus the wavelength of the light produced, providing a wavelength tunable diode laser (TDL). The tuning range or free spectral range (FSR) is usually of the order of 6 nm for a 50 K change in temperature. Significantly though, in contrast to an ECDL a DFB there is no competition between the external and internal cavities to produce a most favourable mode and thus the familiar step-wise mode-hop behaviour of the ECDL is avoided as shown in Fig. 3.2. The output wavelength changes with temperature due to thermal expansion of the cavity. Altering the current to the diode also changes the temperature of the laser and hence the wavelength. This property can be used for frequency stabilization. The thermal coefficient is 0.06 nm/K and the current coefficient is 0.003 nm/mA corresponding to 300 MHz/K and 15 MHz/mA respectively. Frequency stabilization to better than 1 MHz requires temperature stabilization in the millikelvin range and current stability to better than 0.05 mA. It has been shown previously [55] for this particular DFB laser that the observed linewidth of a few MHz is not due to a single cavity resonance, but in fact consists of a lot of fluctuating resonances of about 300 kHz in width, which persist typically for times of about 0.5 μs and together provide a time-averaged envelope. The jumps are thought to be due to inhomogeneities in charge carrier density caused by spatial hole burning and leading to changes in the preferred mode. In our case this envelope was measured with a beat experiment and found to be around 6 MHz, comparable to the natural linewidth of the Rb transition.

We designed a temperature-stable mount with temperature regulation via Peltier

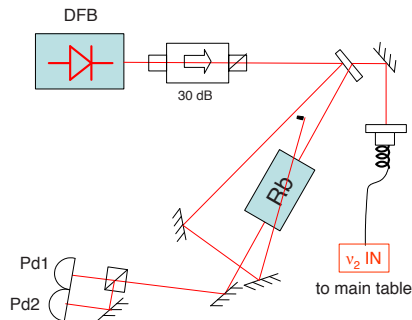


Figure 3.3: DFB locking set-up employing polarization spectroscopy to produce a difference signal on photodiode pd1 and pd2 which are used to lock the laser.

elements (based largely on the mount for the tapered amplifier discussed in the next section). We then set up a DC polarization Zeeman spectroscopy configuration (see Fig. 3.3). Linear polarized light is sent through a Rb saturation spectroscopy cell which has a coil of manganin heating wire wrapped around it. Another coil is used to create a static magnetic field of some 4 G which separates the Zeeman sublevels for σ^+ and σ^- polarized light, shifting them in opposite directions. A second beam (split off from the first) is reflected back through the cell as a probe beam, allowing detection of a doppler-free saturated absorption spectrum. A combination of quarter waveplate and polarization cube allows us to direct σ^+ and σ^- polarized light components onto separate photodiodes. These are then electronically subtracted to create a dispersive signal used for locking. Feedback to the current supply of the DFB allows compensation of thermal drifts as well as suppression of the effects of electronic noise.

3.1.3 Tapered amplifier

The total laser power needed for laser cooling and trapping in this experiment is of the order of 120 mW after outcoupling from a polarization maintaining fiber. This increased requirement with respect to the previous use of bulk optics, could not be met by the DL100 (*Toptica*) alone and was only marginally fulfilled by other lasers used previously [44] so an optical amplifier was introduced to the set-up. The tapered amplifier (TA) operates much as a diode laser and can be similarly seeded with incoupled light. However, in the absence of seeding of light, the TA emits only amplified spontaneous emitted light, while suitable seeding leads to stimulated emission and up to 50 times amplification of the incoming beam. It also has a quite different geometry comprising an index-guided straight section and a gain-guided tapered section with AR coated facets at either end. In our experiments the tapered amplifier was variously seeded by a DFB or ECDL. The emission of these lasers can be amplified if the laser wavelength falls within the gain profile of the amplifier. The

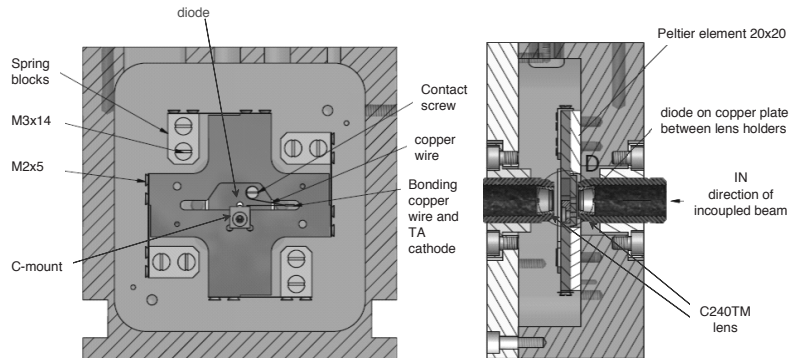


Figure 3.4: Left: Inside of tapered amplifier mount showing the diode, a grounding contact screw and spring mounted translation-free copper plate. Right: From the side the position of the in- and out-coupling lenses as well as the peltier element are visible.

seed laser is coupled into the narrow straight section. The amplified laser light is emitted at the facet of the tapered section. Since both sides have to be accessible and the electrical power input is of the order of 4.5 W (2-2.5 A and 1.8-2 V), mounting of the TA is not trivial. Some 1 W of this power is produced in the form of light when correctly seeded, so about 3.5 W is dissipated as heat. This heat load is considerable compared to standard diode lasers and requires careful design to prevent excessive heating of the diode or loss of alignment both on inject side and on the output side where the light is coupled into a single mode fibers.

Diode and Housing

The tapered amplifier diode used in these experiments was the EYP-TPA-0780-01000-3006-CMT03-0000 (*Eagleyard Photonics*), supplied in a 2.75 mm C mount package and inspected under a microscope for defects upon in-take. To ensure stability of beam power and direction we developed a housing which could deal with the thermal load produced with minimal translation due to thermal expansion. The housing is made of aluminium and contains a copper cross-shaped block mounted on 4 springs and screwed in place with nylon screws to the aluminium housing (see Fig 3.4). This mounting block functions as a cooling plate temperature-stabilized by two Peltier elements (*Eureca Messtechnik GmbH TEC 1H-30-30-44/80-BS*) as well as a beam direction stabilizer. The innovative spring mounted construction has the result that any differential thermal expansion in the mounting plate will cause to first order only a rotation and not a translation of the tapered amplifier. This holds for both facets of the TA, so not only is good coupling maintained with the seed beam, but the outgoing beam remains coupled to the optical fiber. In our design two small lenses (*Thorlabs C230TME-B*) are mounted in PEEK cylinders which can be screwed in and out for

accurate semi-permanent positioning of the foci. To protect against overheating the diode, an interlock was included to shut down in the current controller if the diode temperature exceeds 40 C.

Seeding and Alignment

Alignment of the seed laser is critical for stability and lifetime of the TA diode and this was a difficulty with commercially available self-seeded lasers. In these designs the spontaneously emitted light produced from the rear facet is reflected back into laser but limits seed power and complicates alignment. Both power and alignment are much more flexible with the introduction of a dedicated seed laser. Additionally the tapered amplifier then takes on the spectral properties of the seed laser, which can be tailored to be superior to the spontaneous emission spectrum of the TA diode itself.

The incoupling facet is only $3 \times 3 \mu\text{m}$ in size which provides an obvious difficulty for introducing the seed beam. Alignment was done with current running through the diode. The TA then produces light from both facets. From the rear facet the beam of light produced is close to circular and can be collimated with a single lens. The $3 \times 190 \mu\text{m}$ front facet produces a beam with differing divergences in the long and short directions. The power of the seed laser should be in the range from 10 mW to 50 mW. Exact focussing into the active region of the tapered amplifier is very important in order to achieve the maximum output power of the tapered amplifier. This difficulty is solved by focusing the incoming light onto this opening by use of a 4.5 mm focal length lens which is adjustable in position relative to the diode as described in the previous section. This alignment uses the light from the free running amplifier. By placing the lens at the position which collimates the emitted light, we simultaneously ensure that a collinear collimated incoming beam is properly focused at the depth of the opening.

Due to the tapered geometry of the chip, the outgoing light not only has a different divergence in the long and short direction of the front facet but also considerable astigmatism. The divergences were measured to be 10.5° and 26.2° , respectively. Our solution to the astigmatism was to first collimate the tapered direction (horizontal in our design) with a 4.5 mm focal length lens as with the incoupling facet and to then use a $f = 60$ mm cylindrical lens to collimate the non-tapered (vertical) direction. As shown in Fig. 3.5, we found collimated beam widths of 1.52 mm and 1.77 mm in the vertical and horizontal directions, respectively, for the lenses selected, the resultant aspect ratio of 1.18 gives a near round beam which helps coupling to an optical fiber. This collimation must be carried out without an optical isolator after the TA and so is done at low light intensity (without seeding) to reduce the chance of damage from back reflection. Once the laser beam has been collimated, a 60 dB optical isolator is put in place as shown in Fig 3.1 after which the TA can be safely seeded and the intensity increased to full specification. We used a telescopic pair of lenses to

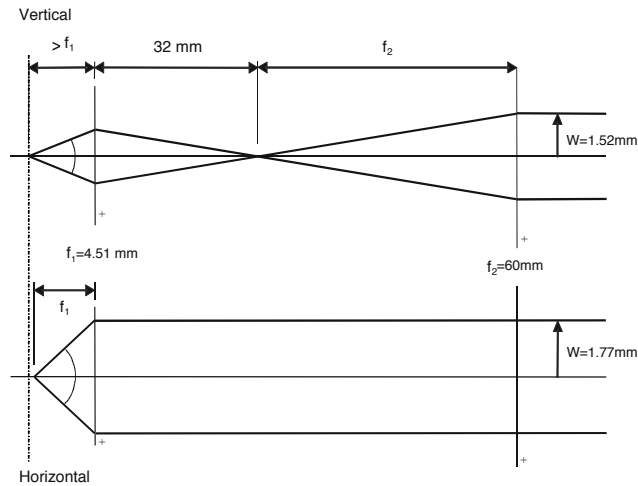


Figure 3.5: Collimation of the outgoing beam of the TA is achieved by placing a lens of focal length 4.51 mm in front of the diode collimating the beam in the horizontal direction and thereafter a cylindrical lens of focal length 60 mm collimating the vertical direction.

decrease the size of the beam to one suitable for incoupling to a fiber. The focused point between the lenses also serves as a convenient location to spatially filter the beam using a pinhole, or as a place to position a shutter for rapid switching of the beam.

Stability Tests and Results

The tapered amplifier was tested with a DFB laser as seed laser [50] which allowed the seed power to be easily varied. The light from the DFB laser was sent to the tapered amplifier via a fiber and a beam splitter was placed in the beam path to allow a pick-off so that the seed power could be monitored. With a seed power of 12.5 mW, it was found that ramping up the current from the power supply we could reach the specified maximum power of 1 W (Fig. 3.6). At an input current of 2 A, we measured 1 W directly from the tapered amplifier. Of this 1 W we found that 640 mW remained after passing through an optical isolator and 440 mW after spatial filtering through a $50 \mu\text{m}$ pinhole. After coupling into input A of our octopus fiber distributor (described in section 2.5) 30 mW was emitted from each of the six branches of the distributor. We thus had 180 W of usable spatially filtered light. While not particularly impressive from a starting power of 1 W directly from the tapered amplifier, this was comfortably more than our requirements and was considered a successful modification given the

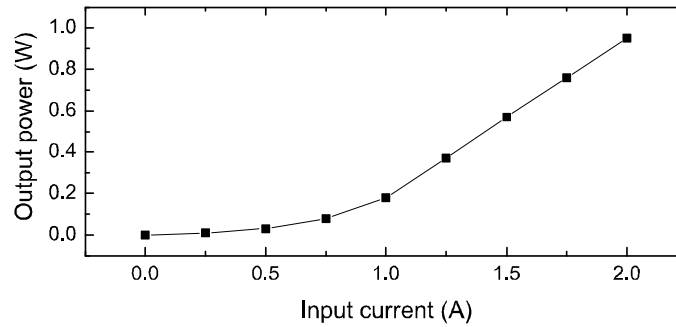


Figure 3.6: Output power of the TA as a function of the current supplied for a fixed seed power of 12.5 mW.

resulting stability. This power was monitored along with the temperature at various parts of the housing. It was found that the temperature of the housing rose 4°C over a period of five hours before stabilizing. However, the effect on the power coupled out of the fiber after an initial settling period was slight (Fig. 3.7) and the power was stable to within 1% over longer periods of time. The M^2 value, a measure of beam quality, was measured to be 1.7, which is a quite good result in comparison with other possibilities for this power and wavelength.

3.1.4 Implementation and usages of stabilized lasers

Our ECDL master laser provides the majority of frequencies in our system with narrow linewidth stabilized power; 10 mW from an ECDL is amplified to up to 1 W of stable, narrow linewidth optical power using the Tapered Amplifier (TA 1) described above. This was used to provide light for cooling and trapping in the upper MOT throughout our experiments while two further tapered amplifiers (TA 2 and TA 3) were used to amplify the trapping light for the lower MOT and repumping light for the entire system. The DFB laser was used for repumping and optical pumping purposes.

3.2 Imaging

3.2.1 Integration with MOT optics

A set of anti-reflection coated glass doublet lenses corrected for spherical aberration, coma and astigmatism (Melles Griot 06LAI011) was placed close to the cell at focal length from the center of the central axis. MOT, optical pumping and imaging

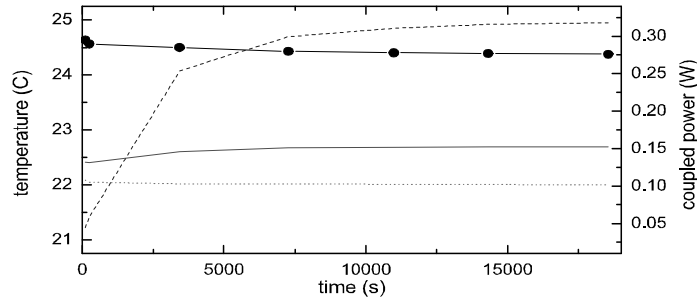


Figure 3.7: Thermal properties of the TA found for a fixed current and seed power over a period of 5.5 hours. Note that while the housing reaches steady state 5 K above the initial temperature (dashed line), the copper plate is well regulated (dot-dashed line) and the diode changes temperature by less than 0.5 K (solid line.) The power loss due to these temperature changes is only a few percent and occurs mainly in the first minutes (black circles).

beams all passed through these four lenses. This configuration is mapped in Fig. 2.9 and Fig. 3.8. The lens chosen has the diameter of the MOT beams (30 mm), a focal length of 100 mm and a numerical aperture of $NA = 0.15$ capturing as much of the solid angle as possible from an aberration free commercial lens of this diameter. This provided an advantage in terms of both space and resolution (see Section. 3.2.2). The lenses are positioned one focal length away from the cloud so that the image can be relayed to the camera. MOT and imaging beams free expand from fiber heads which are located one focal length the opposite side of the lens so that they are collimated after passing through the lens. Imaging beams and MOT beams arrive orthogonally at a polarization cube and are combined before passing through the cell. Note that the imaging beam is linearly polarized. The resulting main imaging line along the axis of the trap is shown in Fig. 3.8. A similar line of imaging is situated perpendicular to the axis of the cloud. Although the MOT beams arrive on the beam splitting cube with opposite polarization to the imaging beams, ensuring that 99% of the light of the MOT beam intensity is not incident on the CCD chip, the remaining 1% is still enough to saturate the camera. The camera is thus shuttered directly in front of the microscope objective where the collected light is brought to a focus. With this configuration and very careful timing, the MOT can be absorption imaged after a very short time-of-flight.

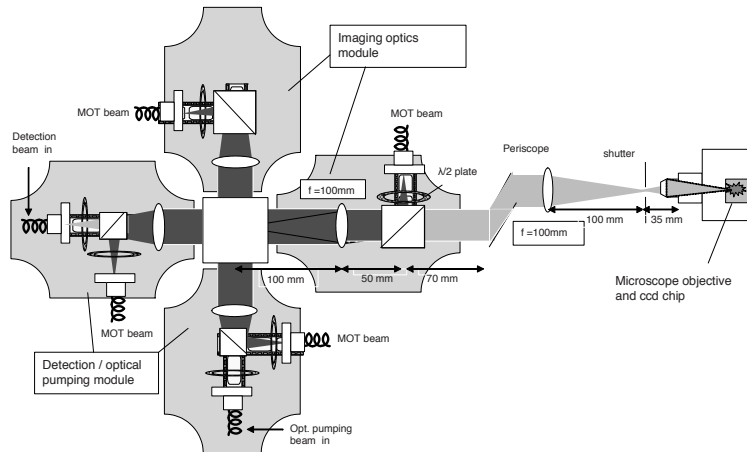


Figure 3.8: Upper optical breadboard consists of four modules which can be independently aligned. Two imaging modules combine MOT and imaging optics integrated on modules (one of these is used for any given experiment). Two detection / optical pumping modules combine repumping and optical pumping or detection with MOT beams. The set up shown is for imaging along the axis of the cloud. Swapping the roles of the detection beam and optical pumping beam and placing the camera on the other imaging module facilitates imaging perpendicular to the cloud axis.

3.2.2 Resolution Tests

Introduction

As shown in Fig. 3.8, a pair of lenses between the cell and the CCD camera separated by the sum of the focal lengths of the lenses relay the image to the camera. The relaying telescope was the limiting factor in the optical resolution of the previous setup [39]. This telescope consisted of two high quality achromats of 100 mm and 200 mm focal length (Melles Griot 06LAI011 and 01LAO189). At 780 nm these lenses provide a near-diffraction limited performance. Following the approach in [39], the optical system was assembled on a single rail away from the setup with a Ronchi ruling (USAF 1951). Later these rails were mounted on modular breadboards so that performance could be easily monitored after installation. To compare various imaging systems, we measure their resolution, *i.e.* the limit or minimum size of a feature which can be identified. Before introducing our findings it is expedient to consider the various definitions which are used to describe resolution values:

- The **Sparrow criterion** measures resolving power as the contrast cut-off distance, a logical definition since when the contrast between two features is zero they are no longer resolved (distinguishable). As soon as the contrast between

two feature is non-zero, they are considered to be resolvable. For a system of optical elements however this excludes the effects of diffraction and for the case of a lens more appropriate definitions consider the Airy disc, the ring-shaped diffraction pattern which occurs when light from a lens interferes.

- The **Rayleigh criterion** requires that the first minimum (zero crossing) of the Airy disk of a feature is aligned with the central maximum of the Airy disk of an adjacent feature for two features to be considered just resolved. Extending this idea to an optical source which can be considered as a point light source, the point spread function is considered - two point sources are regarded as just resolved when the principal diffraction maximum of one image coincides with the first minimum of the other. Finding sub-resolution radiating sources or Airy maxima is problematic so for practical purposes a contrast value of 26.4% is considered necessary to satisfy this condition.
- The **$1/e^2$ width** is commonly considered for Gaussian optics such as that of laser beams. This is the distance where the intensity falls to $1/e^2$ times the maximum value, thus a minimum contrast of 13.5% is necessary. This measurement is thus a weaker condition than Rayleigh's criterion and hence will give a smaller diffraction-limited spot size or linewidth.

In this work we will use the more conservative Rayleigh criterion which for an ideal lens gives the resolution as

$$\Delta L = 1.22(f\lambda/D), \quad (3.1)$$

where f and D are the focal length and diameter of the lens and λ the wavelength of the incident light. In general, Sparrow's resolution limit is about half the length of Rayleigh's resolution limit.

Tests

The resolving power of a set of Melles Griot microscope objectives was tested by imaging a USAF resolution plate backlit with 780 nm laser light via a microscope objective onto the CCD camera described in Section 3.3.2. The contrast between the sets of vertical and horizontal bars is measured and compared to the Rayleigh criterion. The notation for the smallest resolvable feature is read from an accompanying table showing the cycles/mm value for each set of lines. The $\times 2.5$ microscope objective (m.o.) was found to resolve features from $16 \mu\text{m}$. The $\times 4.0$ m.o. resolves from $10 \mu\text{m}$ and the $\times 6.3$ m.o. resolves from $6 \mu\text{m}$. The $\times 10$ Olympus microscope objective resolves to better than $4 \mu\text{m}$, the smallest feature size available on the resolution plate. These results are shown in Fig. 3.9.

Two lens telescopic systems were tested using the same method. With the $1\times$ transfer telescope (i.e. two 06LAI011 lenses), a resolution of $16 \mu\text{m}$ was measured. Testing the $2\times$ telescope (Melles Griot 06LAI011 and 01LAO189), the resolution was

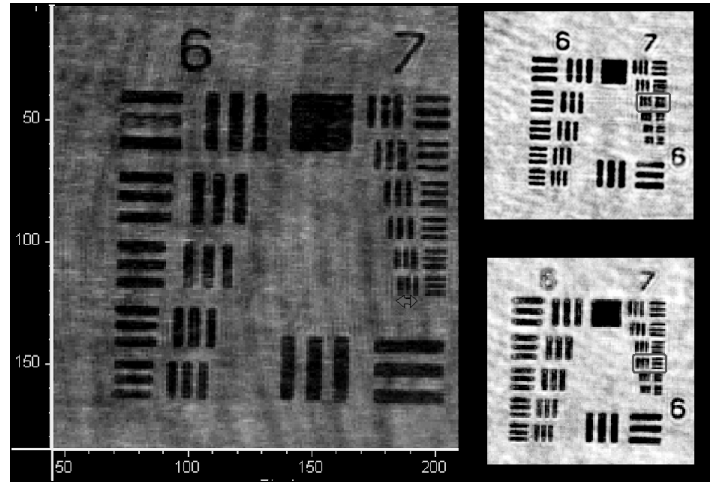


Figure 3.9: Imaging of USAF gratings using microscope objectives of magnification $\times 10$ (left), $\times 4$ (top right) and $\times 6.3$ (bottom right). Note that on the left all sets of lines are resolved, top right the 4th smallest and bottom right the 3rd smallest lines are just resolvable.

found to be $12 \mu\text{m}$, so it appears that the resolution of the $2\times$ telescope is superior. However when we combine the lens system with a microscope objective we get the opposite result: as low as $5.5 \mu\text{m}$ for the $1\times$ telescope, but no better than $8.8 \mu\text{m}$ for the $2\times$ telescope.

Resolution of a lens system

The results indicate that the magnifying power of the lens system is important and also that we cannot ignore a key property of the camera used to measure; the pixel size $r_{\text{pixel}} = 15 \mu\text{m}$. These two effects combine so that when measuring with magnification M , an area of width $\Delta x_{\text{pixel}} = r_{\text{pixel}}/M$ is imaged on each pixel. When resolution measurements are taken in this manner what is measured is in fact a convolution of this effective pixel size with the actual resolution limit of the lens. Thus for a single lens of resolution Δx_1 we approximate the measured resolution by

$$\Delta x_{\text{meas}} \simeq \sqrt{\Delta x_1^2 + \Delta x_{\text{pixel}}^2}. \quad (3.2)$$

For a telescopic lens system consisting of two lenses of resolution Δx_1 and Δx_2 , the total resolution of the system is obtained from a convolution of the point spread function of each lens and can be approximated by

$$\Delta x_t \simeq \sqrt{\Delta x_1^2 + \Delta x_2^2}. \quad (3.3)$$

Table 3.1: Resolution achievable with a system of two lenses for two 100mm lenses and a 100mm, 200mm pair. Each system was tested without additional microscope objective (m.o), with a x10 olympus m.o and with an intermediate m.o. Tabulated are the respective net magnifications, effective pixel size, diffraction limited resolution (dlr) as calculated with the Rayleigh condition as well as the actual measured resolution using a Ronchi grating and the resolution of the telescope implied by this measurement

optical system		calculated		measured	
telescope	lenses	Δx_{pixel}	d.l.r. ΔL	total Δx_{meas}	lenses Δx_t
1×	100, 100 mm	15 μm	15.7 μm	16 μm	5.6 μm
	with ×6.3 m.o	2.4 μm	5.1 μm	6.2 μm	5.7 μm
	with ×10 m.o	1.5 μm	4.7 μm	5.5 μm	5.3 μm
2×	100, 200 mm	7.5 μm	10.4 μm	12 μm	9.3 μm
	with ×4.0 m.o	1.875 μm	7.4 μm	8.8 μm	8.6 μm
	with ×10 m.o	0.75 μm	7.2 μm	8.8 μm	8.8 μm

Applying Eq. (3.2), we can estimate the measured resolution of the system as

$$\Delta x_{meas} \simeq \sqrt{\Delta x_t^2 + \Delta x_{pixel}^2} = \sqrt{\Delta x_1^2 + \Delta x_2^2 + \Delta x_{pixel}^2}. \quad (3.4)$$

To understand the results, experimental values for the resolution measurements found with Eq. (3.4) are compared with those calculated with the Rayleigh ideal lens formula Eq. (3.1). Substituting wavelength $\lambda = 780 \text{ nm}$, and a lens diameter $D = 30 \text{ mm}$, for the lens of focal length $f = 100 \text{ mm}$, an estimated diffraction limited resolution of $\Delta L = 3.2 \mu\text{m}$ is found. For focal length $f = 200 \text{ mm}$, this value is $\Delta L = 6.4 \mu\text{m}$. Combining each lens with a second lens of focal length $f = 100 \text{ mm}$ we get diffraction limits of $\Delta L = 4.5 \mu\text{m}$ and $\Delta L = 7.2 \mu\text{m}$ for the 1× and 2× telescopes respectively. As Table 3.1 shows, we do not quite reach the estimated diffraction limited imaging. However the results are consistent, differing for each lens set on the scale of the 12% difference between successive elements of the test target, our effective measuring error level. The table clearly shows the advantage of the pair of 100 mm focal length lenses as the relaying telescope, used for all subsequent experiments.

3.2.3 Image blurring by the atoms

In the above tests resolution is measured by imaging the light blocked (absorbed) by the dark lines. In experiments with BECs however the incident resonant light on atoms will cause photons to be absorbed and some of the photon energy eventually turned into additional atomic kinetic energy; *i.e.*, our measurement moves the atoms

whose position we are trying to measure. We can calculate the blurring effect from the imaging photons to the atoms by considering the re-emission of this energy as a velocity kick in a random direction. This velocity is known as the recoil velocity and can be expressed as

$$v_r = \frac{hk}{m} \quad (3.5)$$

The net effect of these velocity kicks is an uncertainty in the release *velocity* of the atoms and hence a blurring in the effective pre-release *position* of the atoms within the cloud. Following the analysis in [56] we take the following measure for the mean blur of a cloud in a given direction:

$$X_{rms} = \sqrt{\frac{N_p}{3}} v_r \partial t \quad (3.6)$$

where N_p is the number of absorbed photons per atom and ∂t is the length of the exposure.

Substituting typical values from our experiments in Eq. (3.5) using the shortest exposures that we typically make, we get a value of $v_{rec} = 5.9$ mm/s for ^{87}Rb atoms. Expressing N_p in terms of P the power density (mW/cm²) of the incident light, $E_p = hc/\lambda$ the energy per photon and $\sigma = 3\lambda^2/2\pi$ the absorption cross section of the atoms, with an exposure time of 40 μs the effect of blurring on resolution is 3 μm .

3.2.4 Conclusions

Lens quality being equal, best resolution is achieved with the lens combination with the highest NA, so for the same diameter and lens quality $f = 100$ mm is preferable to $f = 200$ mm. In particular with high magnification, camera pixel size becomes less important and lens quality and NA will dominate. The choice of $f = 100$ mm also allows us to have a compact and modularized design. Blurring due to recoil velocities is minimized with short exposures. A recoil velocity with our parameters of 5.9 mm/s is low compared to lighter atoms, nonetheless it is a potential limitation on resolution causing a blurring of some 3 μm . Combined with the lenses selected it will be possible to resolve features in atomic clouds above $\sqrt{3^2 + 5.5^2} = 6.2$ μm in diameter along or perpendicular to the long axis of the cloud.

3.3 Analysis of Imaging Noise

The information used to analyze sample cloud properties in the experiments of Chapters 4 and 5 is provided by absorption imaging, the standard method to detect and measure a BEC. A resonant or near-resonant laser beam is passed through an atomic cloud with the absorption shadow imaged onto a CCD camera. There, the transmission profile is measured and the amount of light absorbed by the atoms can be

determined. The 2D distribution of the transmission profile can be related to the 3D distribution of the cloud by considering the absorption of light by atoms along the direction of propagation of the light as a column density at each point on the CCD. To exclude external influences on the profile of the light, a dark background image is subtracted and the profile normalized to an image of the beam's transmission without the atomic cloud present. The log of this normalized transmission profile at any point is known as the optical density (OD) and this can be related to the atomic density distribution n of the cloud by the following relation

$$\text{OD}(x, y) = \sigma \int n(x, y, z) dz \quad (3.7)$$

where σ is the scattering cross-section of the light and z the direction of propagation of the light [56]. The total number atoms is then calculated by summing over the profile of the cloud. The scattering cross section σ depends on the detuning from resonance of the imaging light, the wavelength λ and the Clebsch-Gordan coefficient of the transition. Estimating the latter when spin states are not well-defined is a source of uncertainty in determining an atom number from absorption imaging. This uncertainty can be reduced by ensuring a spin-polarized sample and imaging with circularly polarized light (σ^+) and a well-defined magnetic field along the direction of imaging. The other source of uncertainty can be the precise detuning from the resonance, so frequency stability of the lasers is also essential.

Absorption imaging is most often employed in concert with time-of-flight (TOF). In this method the cloud is not imaged in the trap but after a given time after release from the trap. The cloud will then expand (ballistically for a thermal cloud) as each atom carries on with its velocity at the time of release. This expansion is measured as a function of time t_{TOF} . Assuming a Gaussian atomic density distribution and temperature T the cloud width w will evolve as

$$w(t_{TOF}) = \sqrt{w(0)^2 + \frac{k_B T}{m} t_{TOF}^2}. \quad (3.8)$$

To make an absorption image, at least three separate exposures are necessary. Firstly, exposure (A) is made with the cloud in the beam path. The profile of the laser beam on the CCD chip will then show a drop of intensity where light is absorbed by the atoms. With minimum delay a second flat field exposure (B) is taken with the same laser beam and beam path but without the cloud so that the profile of the light beam without the absorption from the atoms is reproduced as faithfully as possible. A third exposure (C) is taken to record the dark background without atomic cloud and without detection beam. The normalized difference is then calculated pixel-by-pixel, creating an $n \times m$ array

$$D = D_{ij} = \left\{ \frac{(A_{ij} - C_{ij})}{(B_{ij} - C_{ij})} \right\}, 1 \leq i \leq n, 1 \leq j \leq m \quad (3.9)$$

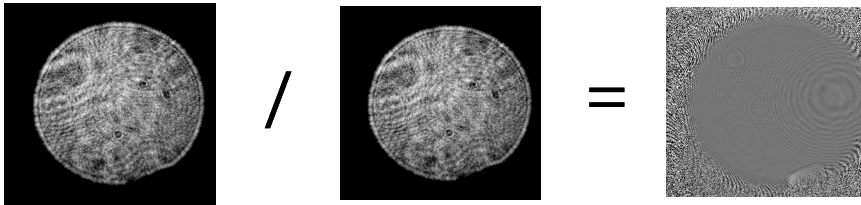


Figure 3.10: Noise measurements without a cloud: pixelwise division of images $A - C$ and $B - C$ (the background image C is not shown) produce a resultant image D . Note that these images taken under identical conditions 1 s apart still leave residual concentric rings even after division.

where $X_{ij} \in \{A_{ij}, B_{ij}, C_{ij}\}$ is the pixel count of the pixel in the i th row, j th column and n, m the number of pixel rows and columns. Accurately determining the atomic density distribution requires good reproducibility of imaging conditions and a low noise level on the images. Noise can come from the method of detection of the photons or from time-dependent disturbances of the wavefront at any of the optical elements in the optical path to the camera. Such disturbances give rise to interference fringes which are fluctuating in time for instance as a result of acoustic noise. Our aim will be to determine the theoretical limits of our imaging system imposed by the detection method and to minimize sources of noise.

3.3.1 Method

Since our cloud exposures are normalized to a flat field exposure, we will follow the same process of normalization in the analysis of the noise. In order to simplify matters, we will consider calibrated exposures in the absence of a cloud (see Fig. 3.10). To estimate the effect of multiple exposures at the same pixel, we measure the noise by considering a sub-array M of the array D of all pixel positions on the CCD chip. We choose $M = \{D_{ij} \mid x_1 \leq i \leq x_2, y_1 \leq j \leq y_2\}$ where (x_1, y_1) and (x_2, y_2) are pixel coordinates such that M defines a square area of adjacent pixels where all pixels can be assumed to give identical response, avoiding any known bad pixels of the CCD chip. For a flat light field the average value over this sub-array should be 1. The variation in normalized pixel count can thus be measured by calculating the standard deviation

$$\sigma(M) = \sqrt{\sum_{i,j \in M} (D_{ij} - \bar{D}_{ij})^2}. \quad (3.10)$$

The value $\sigma(M)$ can be considered to be a good approximation for the variation over multiple exposures on a single pixel. It is thus a good measure of the noise ratio $\Delta N/\bar{N}$ (standard deviation/mean) on processed images, which is the inverse of the commonly used signal to noise ratio (SNR). The quality of our imaging can be

improved by quantifying and achieving a reduction of the relative noise.

There are three limiting factors to achieving a low noise ratio for a given optical detection system: these are read-out noise, dark noise and photon noise. The first two are related to properties of the camera. Read-out noise is the noise introduced during the process of quantifying the electronic charge on the pixels. This noise originates from the on-chip preamplifier and analogue-to-digital conversion. Dark noise is due to the statistical variation of thermally generated charge on the pixels. Cooling the camera CCD from room temperature to -25 C reduces dark noise by a factor of 100.

The third and most important limiting factor is photon shot noise. The photon flux per pixel obeys poissonian statistics, which means that the pixel charge grows proportional to the number of photons while the photon shot noise increases with the square-root of the number of photons incident on a pixel. This means that in relative terms the shot noise becomes less significant for higher intensity. Taking these limiting contributions to the noise for a given exposure and detection system together, the best achievable noise ratio $\Delta N_0/\tilde{N}$ for our camera can be expressed as

$$\Delta N_0/\tilde{N} = \frac{\sqrt{(\alpha_{QE}\dot{N}_s + \dot{N}_d)t + N_r^2}}{\alpha_{QE}\dot{N}_s t} \quad (3.11)$$

where \dot{N}_s is the photon flux (photons/pixel/second), α_{QE} is the quantum efficiency of the camera, and t is the integration time (second); \dot{N}_d (electrons/pixel/second) is the rate of increase of the dark count with time and is heavily temperature dependent. The read noise, N_r ($\sqrt{\text{electrons/pixel}}$) is independent of both photon flux and exposure time.

In the following tests, the integration time t will be fixed and only the photon flux \dot{N}_s will be varied so that $\Delta N_0/\tilde{N} \equiv \Delta N_0(\dot{N}_s)/\tilde{N}(\dot{N}_s)$. We will measure the constants \dot{N}_d , N_r and α_{QE} and so establish the lowest noise ratio which can be reached. Eq. (3.11) gives the noise on a single image such as A , B , C as described above and as such is arguably not directly applicable to the situation of the normalized array D , where multiple contributions from each of these noise sources should be included for a full error analysis. It nonetheless gives a good lower bound for the reproducibility of an exposure and is thus used to compare to measurement of the D matrices with the method described above.

3.3.2 Camera

The camera used to produce the images is the TE/CCD-512EFT (*Princeton Instruments*) which functions in either a frame transfer or kinetics mode chosen by way of a switch. The CCD-chip type is EEV 512x512 FMTR and can operate as low as -70 C using a thermoelectric cooler. The chip has a full size of 7.7×15.4 mm with 512×1024 pixels of size $15 \mu\text{m} \times 15 \mu\text{m}$. Half of the chip is shielded from incident light by a mask, so only a maximal surface of 7.7×7.7 mm can be illuminated, *i.e.*

an area of 512×512 pixels. The read-out procedure involves two steps. First the image information stored in the lower half is shifted under the mask. Then the actual read-out is done line-by-line. This procedure is chosen because the shift is fast ($0.2 \mu\text{s}/\text{line}$) and the read-out is slow ($15 \mu\text{s}/\text{line}$). In this way, exposure to light during read-out is minimized.

In the read procedure, the information is then processed by the camera controller ST-138 which has two modes of Analogue-to-Digital Conversion (ADC): 12 bit and 16 bit registers. These registers are full at 2^{12} and 2^{16} counts respectively, so the 16 bit can give greater accuracy but the 12 bit has the advantage of greater speed. To test the readout of the ADCs and also estimate dark noise, background images (no light on camera) were taken. With the 12 bit ADC a background count of 307(1) counts/pixel is found per exposure. The 16 bit ADC gives an offset of 230(1) counts/pixel per exposure. The background contribution can thus be subtracted from our images to an RMS accuracy of about 1 count/pixel which gives the read noise contribution for a divided image. This translates to $N_r \simeq 20 \sqrt{\text{electrons/pixel}}$ using the calibrations in Section 3.3.2. These measurements were made with exposures of $40 \mu\text{s}$, typical for measurements. Taking progressively longer exposures we can measure the dark count N_d . This value is found to be 10 electrons/pixel/second with a camera cooled to -40 C and for the $40 \mu\text{s}$ exposures a negligible contribution to the noise.

As in many cooled cameras, the fan of the thermoelectric cooler is a source of vibration, which effects the light field reproducibility and shows up as noise at the pixel level. This is removable by switching off the fan when imaging.

Controls

The camera software, WinView32 (*Roper Scientific*) works in concert with a Labview (*National Instruments*) visual interface. This works differently in frame transfer and kinetics mode and since both modes will be used in the experiments and tests, a brief description of the differences are given here.

For most of the tests we use the frame transfer mode. The camera is activated via WinView by means of an active-X command. This initiates a constant cleaning mode. Subsequently, a TTL-high pulse of maximum duration 0.5 ms starts exposure for a time specified in the WinView software, after which the exposed half of the chip (512×512 pixels) is read-out. The time to shift one line is $0.2 \mu\text{s}$, the time to shift one line into the register is $15 \mu\text{s}$ and this is then followed by the digitization time. Either 12 bit or 16 bit may be selected under ADC conversion. The time to digitize one pixel is $0.9 \mu\text{s}$ for 12 bit and $10 \mu\text{s}$ for 16 bit. At 12 bit the overall frame capture cycle takes 0.6 s while for 16 bit this takes 2.7 s. A trigger pulse exceeding 0.5 ms results in read-out of the entire 1024×512 pixels, which includes the masked area.

In this case we acquire 4 images in 4 WinView frames. The timing of the first exposure was found to be unreliable. This is probably caused by differences in the termination of the cleaning cycle, the process by which accumulated charge on the

CCD before imaging is removed to begin measurements. Therefore, only the three subsequent exposures are used. The 2nd exposure is called the signal exposure (A), the 3rd the flatfield (B) exposure and the 4th the background exposure (C). Only during the 2nd and 3rd exposure is the imaging beam on. Exposure during the shift stage of the read-out must be avoided.

The kinetics mode allows multiple shifts of a specified number of lines before read-out of the lower 512 lines of the chip as above. This allows multiple exposures at a repetition rate limited only by the shift time. To make use of this feature, the hardware set-up menu in WinView must have Kinetics mode selected as well as a number of lines $n_k \leq 512$, required per exposure. In this mode the TTL pulse will finish the previous exposure of n_k lines and after the required shift time the next exposure will begin automatically. To avoid exposure beyond the selected n_k lines, an external mask must be put in place to block light to the rest of the chip.

Calibration and Quantum Efficiency

To calibrate the bit counts of the ADC to incident photon numbers, the CCD chip is exposed to laser beams of known intensity. The photons per pixel are then plotted against the counts recorded in the WinView software at both 12 bit and 16 bit ADC resolution. It should be noted that the count/photon ratio varies substantially with exposure time. For a fixed exposure time of 0.2 ms we find a good linear relation over a range of values. For 12 bit ADC we find 0.019 counts/photon (53 photons/count) and for 16 bit ADC: 0.063 counts/photon (16 photons/count). In 12 bit mode the ADC register is full at 4096 or 2^{12} counts which corresponds to 20,000 photons/pixel. In 16 bit the ADC register would be full at 65536 or 2^{16} counts but already at 20,000 counts the response becomes non-linear, reaching saturation at 30,000 counts (see Fig. 3.11).

This saturation effect gives a useful way to check the quantum efficiency of the camera. Each CCD-well is specified to collect up to 129,000 electrons. Thus in 16 bit, we can expect the electron well to saturate before the ADC register can be filled. The camera is specified with a quantum efficiency of 45% at 780 nm, the wavelength of the imaging light. At high intensities, we can see the number of counts reach a saturation value of 340,000 photons/pixel. According to the specifications of the manufacturer, the end of the linear regime corresponds to a full well (129,000 electrons). This gives a measured quantum efficiency of 38(2)%,

$$\alpha_{QE} = \frac{\text{\#electrons}}{\text{\#photons}} = \frac{\text{electrons in full well}}{\text{photons recorded at linear limit}} = \frac{129000}{340000} = 38(2)\%. \quad (3.12)$$

Using this quantum efficiency we can compare the contributions from read noise and dark noise with that from photon noise using Eq. (3.11). For our camera, at -40 C, dark noise contribution is negligible, a factor of 1000 less than the read noise. For

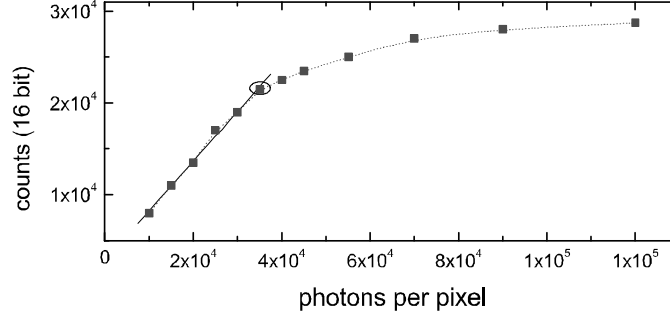


Figure 3.11: The Quantum Efficiency (QE) is found by measuring counts vs photons per pixel and noting the limit of the linear range which indicates a full electron well. Squares indicate measured values, solid line indicates a fit to the linear regime and the black ring shows the linear limit.

low-light exposures the image quality is read noise limited. With an exposure time of $40 \mu\text{s}$, the photon noise term in Eq. (3.11) becomes greater than the read noise for exposure intensities higher than $0.005 \text{ mW}/\text{cm}^2$. Thus, at the light intensities used in experiments with BEC clouds as described in this thesis ($0.1 \text{ mW}/\text{cm}^2 - 1 \text{ mW}/\text{cm}^2$), the image data is photon-limited and displays a near square-root relationship to the number of incident photons. The noise ratio ($\Delta N/\tilde{N}$) from the photon noise for a range of light intensities is plotted in Fig. 3.12 along with the camera limited noise ratio $\Delta N_0/\tilde{N}$ as calculated using Eq. (3.11). The measured noise in our experiments will be compared to these limits. The range $0.1 \text{ mW}/\text{cm}^2 - 1 \text{ mW}/\text{cm}^2$ for a $40 \mu\text{s}$ exposure is also indicated in the figure as is the electron well depth.

3.3.3 Reducing the noise

The data points in Fig 3.12 show the results measured experimentally using the method mentioned in Section 3.3.1. Consecutive exposures of a calibrated collimated beam with a flat wavefront were imaged onto the Princeton Instruments TE/CCD-512EFT. The exposures were then processed using Eq. (3.9) to produce an image as in Fig 3.10. The standard deviation (sigma) inside the area of the light beam of the processed image is calculated and this number is the relative noise compared to unit average. Physical imperfections in the imaging optics produce undesired patterns in the images such as fringes. These patterns are minimized by the image processing procedure, but persist if the fringes move between exposures. It is thus essential to reduce time-dependent disturbances of the wavefront caused by vibrations. In practice this is done by minimizing the time between exposures. Further improvement can be made by image selection. This gives rise to a trade-off between image quality

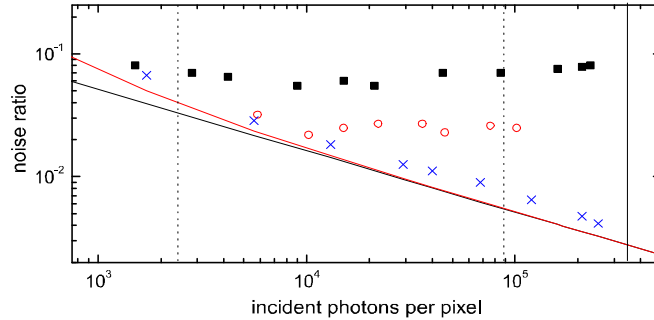


Figure 3.12: Plot of noise ratio versus signal on a log-log scale containing data points from three sets of measurements and systematic limits. The straight black line shows the photon shot noise $\Delta N/\bar{N}$ and the solid red curve shows the total limiting noise ratio $\Delta N_0/\bar{N}$ for the noise on a single image. The solid squares show noise measurements from images containing many fringes using the imaging system as received. The open circles show measurements with reduced noise following selection of optical elements. The crosses show the improvement of imaging quality to near poissonian-limited noise after selection of optical elements and after the replacement of the CCD window. The dashed vertical curves show 40 μ s exposures representing 0.1 mW/cm² and 1 mW/cm², while the solid vertical line corresponds to the full electron well exposure (see Fig. 3.11).

and measurement time. In our case a discard rate of 40% was used, comparable to other authors [57].

Using the full imaging system as shown in Fig. 3.8 the measurement points taken with unselected optics in Fig 3.12 show a relative noise level $\Delta N = 0.08(1)$. This noise level is due to fringes which are not entirely divided out. Further improvement can be gained by taking a series of flat-field exposures and by post-processing the exposures are selected that best reproduce the fringes of exposure *A* [58]. This results in a smaller discard rate but this was not employed here. Although the imaging processing results in a spectacular improvement in image quality as illustrated in Fig. 3.10, for best results it is important to eliminate - as good as possible - the sources of the wavefront distortions, for instance dust on the imaging optics or other blemishes. To trace such sources, one method is to rotate each optic to see if a feature moves and then cleaning the relevant optic. For inaccessible blemishes it is possible to identify the focal plane of the blemish and insert a pinhead to block the diffracted light. Dynamical sources of wavefront distortion such as dust in the air are minimized by enclosing the beam path. Using these methods we improve the relative noise for the highest exposure intensities from around to $\Delta N = 0.02$ for frame transfer and to $\Delta N = 0.015$ in kinetics mode (shorter time between exposures). This is illustrated by the points taken with selected optics (red circles) in Fig. 3.12. Note that the relative noise is essentially constant for intensities above 10,000 photons per pixel. As will be

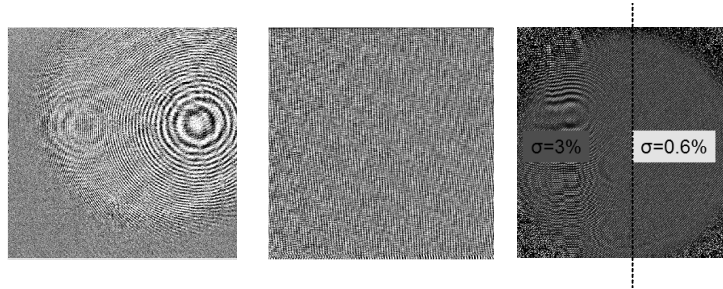


Figure 3.13: Divided images with camera test set-up. Left: an image taken with a collimated beam incident on the ccd via microscope objective. Middle: an image taken with a collimated beam directly incident on the ccd. Right: image taken with light incident via a microscope objective but with the incident beam at an angle to chip. This image shows an area of high noise ($\Delta N \equiv \sigma = 0.03$) on the left due to interference and an interference free region on the right with a lower noise level ($\Delta N \equiv \sigma = 0.006$).

explained below, this results from fringes originating at the camera window.

To test the camera, we made a reduced set up consisting of laser, single mode fiber, collimating lens and camera. Fig.3.13 shows the images taken with and without a microscope objective in the left and middle panels, respectively. The left panel correspond to a diverging beam obtained by inserting the microscope objective used in imaging the gas clouds. The central panel is free of bull's-eye shaped fringes but contains interference stripes both vertically and diagonally. The explanation was found with experiments varying the angle of the light incident to the chip as shown in Fig.3.14. The CCD chip is a very reflective surface, and although the vacuum window is AR-coated, the incoming beam will interfere with the reflected beam from the chip. Depending on the angle, a larger or smaller fraction of the chip is exposed to the interference (see right panel of Fig.3.13). By using a tilted

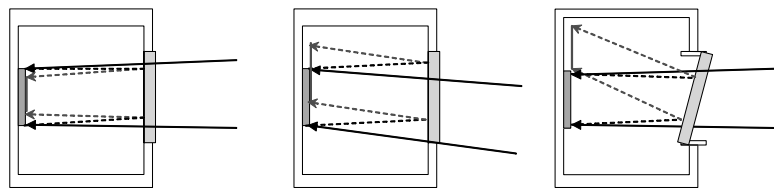


Figure 3.14: Slightly convergent collimated beams incident on the camera. Left: beams normal to ccd via original camera window results in circular interference pattern. Middle: beams at angle to original window result in interference pattern on part of ccd chip. Right: beams normal to ccd via angled camera window result in no interference on ccd.

camera window, the reflection between chip and window can be eliminated. For this purpose a camera window was custom made (*LENS-optics*) which could be fitted at 15° to the surface of the chip replacing the original. The results were essentially fringe-free images with and without microscope objective as in the right side of the right panel of Fig. 3.13. The best relative noise, $\Delta N = 0.003$, was observed with 16 bit ADC to accommodate exposures approaching 1 mW/cm^2 . At this low noise the imaging becomes very susceptible to other disturbances in the optical path and the best results were obtained with a discard rate of 40%. Measuring under these conditions as a function of imaging intensity we obtain the results shown by the blue cross-shaped data points in Fig. 3.12, only slightly above the theoretical limit of shot noise, dark noise and read noise for a single exposure. The deviation from this limit may in part be attributed to our procedure of normalizing to a flat field exposure to produce an image as described in Section 3.3.1 resulting in an underestimate of the system noise limits where we consider only a single exposure.

3.3.4 Conclusion

In our experiments we demonstrated that we can approach the poissonian limit for the signal-to-noise of our images. In principle, this signal-to-noise ratio could even be improved by a factor of two by using a camera with a higher quantum efficiency. However these signal-to-noise ratios were only achieved on the test bench and could not be reproduced with the full imaging system including vacuum cell necessary to observe the gas clouds. With the latter a typical exposure is a factor of 3 worse than the camera limited noise. To achieve the poissonian limit on the full apparatus, extreme care is required in avoiding dust, in particular on the inside of the vacuum system, which means that mounting of vacuum components under cleanroom conditions seems indispensable. Also, in hindsight, combining the MOT optics with the imaging optics, results in more optical surfaces which can become contaminated or give rise to interferences and although essential for the measurements discussed in this thesis, this configuration is less favourable from a signal-to-noise point of view.

Chapter 4

Measurements with long-lived condensates

4.1 Introduction

There are two hyperfine levels $F = 1$ and $F = 2$ of the electronic ground state in ^{87}Rb with three trappable magnetic substates $|F, m_F\rangle = |2, 1\rangle, |2, 2\rangle, |1, -1\rangle$. The previous successful experiments on our apparatus, creating and manipulating condensates, exclusively employed the $|2, 2\rangle$ state. Following the upgrades discussed in Chapters 3 and 4, it was possible to image BEC clouds with large atom numbers in the $|2, 2\rangle$ state, along and perpendicular to the cloud axis. This trappable state has the advantage that it can be imaged on a cycling transition but it has the strong disadvantage of a short lifetime due to collisions with $|2, 1\rangle$ atoms which are trapped spuriously. This limits the experimental possibilities to measurements that do not require a long sample lifetime. To enable the possibility of observing clouds over longer time periods, we developed a method of condensing atoms in the $|1, -1\rangle$ state, requiring modification of the apparatus. These modifications, the experiments on the $|1, -1\rangle$ samples and some of the underpinning theory will be discussed in this chapter. We begin in Section 4.2 by outlining the optical pumping, trapping, evaporative cooling and imaging of the atomic samples. In Section 4.3 we create a BEC of $F = 1$ atoms in the Ioffe-Pritchard trap and measure its properties including lifetime of the sample. We proceed to a BEC of $|1, -1\rangle$ atoms in a time-averaged orbiting potential (TOP) for both a single well and double well potential. Section 4.4 explains the origin of vorticity of the trapped condensate and outlines methods to create and detect vorticity in the sample. Finally, Section 4.5 describes our experiments in a rotating TOP and our efforts to induce and detect vortices.

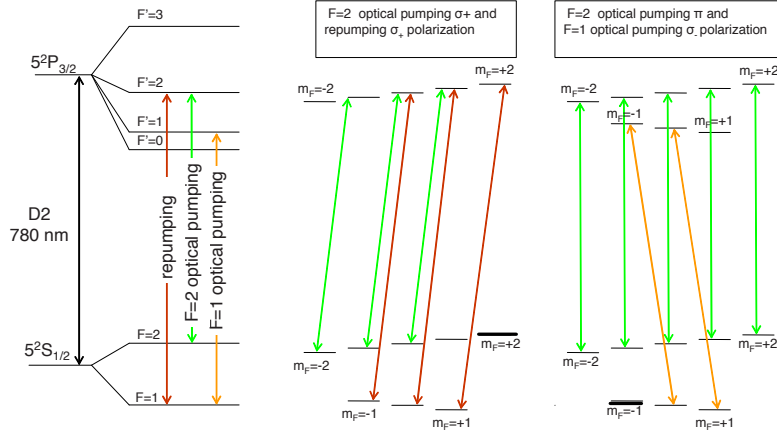


Figure 4.1: Optical pumping schemes with dark states represented by a thick black line. Left: a simplified level diagram showing the $F = 1$ and $F = 2$ manifolds of $5S_{1/2}$ and $5P_{3/2}$. Center: preparation of $|2, 2\rangle$ using $F = 2 \rightarrow F' = 2 \sigma_+$ transition to pump atoms out of the unwanted $F = 2$ states and a $F = 1 \rightarrow F' = 2 \sigma_+$ transition to repump atoms from $F = 2$ states. Right: preparation of $|1, -1\rangle$ using $F = 2 \rightarrow F' = 2 \pi$ -transition to clear out the $F = 2$ state and a $F = 1 \rightarrow F' = 1 \sigma^-$ transition to remove atoms from the unwanted $F = 1$ sublevels.

4.2 Trapping and condensing the $|1, -1\rangle$ state

4.2.1 Optical pumping scheme

All sublevels are equally populated in the MOT and molasses stages, we modified both optical pumping and magnetic trapping to work with $|1, -1\rangle$. The concept of optical pumping has been outlined in Section 2.3 and we continue the nomenclature adopted there to describe levels, sublevels and the transitions of the D2 line. To collect atoms in the $|2, 2\rangle$ state it is necessary to drive the σ^+ transition $F = 2 \rightarrow F' = 2$, while also repumping the atoms from the $F = 1$ manifold back to $F = 2$ as illustrated in Fig. 4.1. When the goal is to collect the atoms in the $|1, -1\rangle$ state, the ideal scheme is to drive the σ^- transition $F = 1 \rightarrow F' = 1$ and to clear the $F = 2$ manifold with π transitions $F = 2 \rightarrow F' = 2$, with a decay channel to $F = 1$. To implement the $F = 1$ scheme we can utilize for the $F = 2$ clearing the same laser as used for the optical pumping in the $F = 2$ scheme. For the σ^- optical pumping on the $F = 1 \rightarrow F' = 1$ transition an additional laser is required. Interestingly, we found that we can do without this additional laser. Optical pumping generally works imperfectly. In the case of optical pumping in the $F = 2$ scheme, typically 40% of

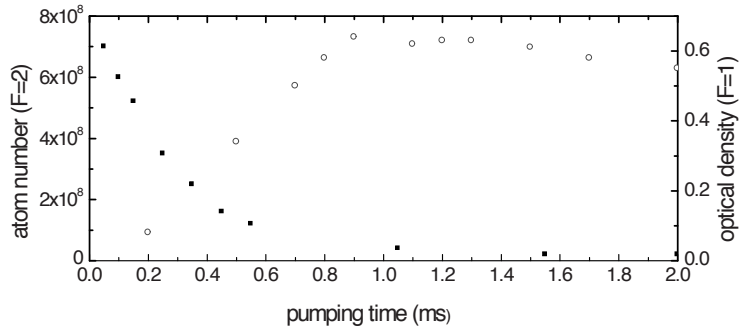


Figure 4.2: Increase of the $|1, -1\rangle$ population as a function of the π excitation $F = 2 \rightarrow F' = 2$ (red circles). The associated loss of $F = 2$ atoms is also shown (black squares). At a later stage after removing stray $F = 1 \rightarrow F' = 2$ light, pumping could be completed within 0.2 ms with the number of $F = 2$ atoms reduced below the level of detectability.

the atoms is transferred to the desired $|2, 2\rangle$ state, corresponding to some 10^9 trapped atoms. In view of the five $F = 2$ sublevels this is a reasonable return. In the $F = 1$ optical pumping scheme we ended up with a similar efficiency. However, as there are only three $F = 1$ sublevels, the use of only the $F = 2$ clearing laser already resulted in the transfer of some 30% of the atoms. Hence, the gain by optical pumping was found to be too small to justify the overhead of the additional laser.

In the time-line of the experiment the MOT is driven as usual on the $F = 2 \rightarrow F' = 3$ cycling transition with 1 mW repumping light on the $F = 1 \rightarrow F' = 2$ transition along one of the MOT axes in the horizontal direction. After switching off the MOT coils we apply optical molasses with the same light. After 5 ms, we stop driving the cycling transition and switch to the π transition $F = 2 \rightarrow F' = 2$ along a single horizontal MOT direction. Simultaneously, we switch off the $F = 1 \rightarrow F' = 2$ repumper and observe the decay to the $|1, -1\rangle$ state. In Fig. 4.2 we show the increase of the $|1, -1\rangle$ population as a function of the duration of the π excitation. Also the associated loss of $F = 2$ atoms is shown. The actual measurement is made after recapturing the atoms for a short time in the magnetic trap. The imaging was done after a time of flight of 5 ms. With this method we typically collected 7×10^8 atoms in the $|1, -1\rangle$ state.

4.2.2 Magnetic transfer and evaporative cooling

In this section we discuss the sequence of steps under which a Bose-Einstein condensate is produced and emphasize the difference with the procedure used for $F = 2$ atoms.

Transfer to the magnetic trap

As mentioned in Section 2.6.1, the effective magnetic moment of the $|1, -1\rangle$ state is a factor of 2 smaller than for the $|2, 2\rangle$ state. This has consequences for the current settings of the magnetic trap. As the size of the MOT cloud is the same after $F = 1$ and $F = 2$ preparation, 40% more current is required to reproduce the optimal axial trap frequency ω_z and radial trap frequency ω_ρ for transfer to the magnetic trap. The transfer was done with the semi-adiabatic method [59]. Due to gravity, the position of the MOT does not match exactly that of the magnetic trap center in the vertical direction and so the cloud is allowed to fall for 1 ms before switching on the magnetic trap. This introduces an oscillation of the cloud in the trap and results after thermalization in a temperature too high to remain trapped. Therefore trap depth is increased before thermalization. Optimizing for the maximum number of atoms the best transfer was realized after a holding time of 50 ms in the shallow trap before compression. For the compression the current was increased to 400 A in 250 ms. In this procedure the cloud temperature increased to approximately 1 mK. The trap bottom field B_0 was then lowered over a period of 1.2 s, decreasing the share of the current through the compensation IGBT at the expense of the current through the pinch IGBT (see Section 2.6) until $B_0 = 0.9$ G is reached. This results in trapping frequencies of $\omega_\rho/2\pi = 339$ Hz and $\omega_z/2\pi = 14.7$ Hz for radial and axial directions, respectively. If B_0 is significantly lowered below this value the cloud suffers from Majorana losses, limiting the trapped cloud lifetime.

RF evaporation was initiated at a frequency of 100 MHz. The optimal evaporation curve was approximated by four linear frequency ramps. The ramp-down rate was optimized for maximum degeneracy parameter $n_0\lambda^3$. The cloud was then imaged after up to 27 ms time of flight.

4.2.3 Imaging

Converting from a system imaging $F = 2$ atoms to imaging for $F = 1$ atoms contains some subtle aspects. Imaging with σ^- light on the $F = 1 \rightarrow F' = 2$ transition sends the $|1, -1\rangle$ atoms to the excited state sublevel $|F', m'_F\rangle = |2, -2\rangle$. However, this is not a closed transition; there is a 40% chance of decay to the dark ground state sublevel $|2, -2\rangle$ so that after absorption of just two photons most atoms are in this dark state. Scanning the detuning of the light and measuring the linewidth shows progressively larger effective linewidths for longer exposures as shown in the left graph of Fig. 4.3. Imaging on $F = 1 \rightarrow F' = 0$ solves this issue and produces a linewidth only slightly larger than the natural linewidth of the transition (6 MHz), neatly demonstrating the narrow laser bandwidth as shown on the right of Fig. 4.3. The latter method requires a dedicated laser for imaging because the ground states $F = 1$ and $F = 2$ are too far apart in frequency to be bridged by an AOM. An alternative way is to use the cooling laser for the imaging. In this scheme, we use excess (3 mW) repumping light

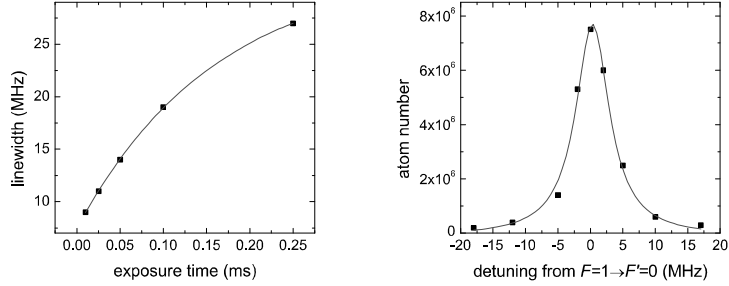


Figure 4.3: Imaging trapped $F = 1$ atoms. Left: linewidth increases with longer exposure on the $F = 1 \rightarrow F' = 2 \sigma^-$ transition. Right: linewidth is as narrow as natural linewidth (6 MHz) imaging with exposure on the $F = 1 \rightarrow F' = 0$ transition. Fitted curve shows lorentzian linewidth of 6.3 ± 0.5 MHz.

($F = 1 \rightarrow F' = 2$) orthogonal to the direction of the camera to transfer the $|1, -1\rangle$ atoms to the $F = 2$ state and image on the $F = 2 \rightarrow F' = 3 \sigma^+$ transition. This simplifies the imaging set-up and makes it easier to switch between experiments with $F = 1$ and $F = 2$ atoms. It has the additional advantage that we can monitor the presence of spuriously trapped $F = 2$ simply by imaging without repumping light.

4.3 $F = 1$ BEC

4.3.1 BEC characteristics and lifetime

Imaging the cloud perpendicular to the trap axis (radial imaging) we can observe the anisotropic expansion as the classic signature of reaching BEC (see Fig. 4.4). At temperatures just below the transition temperature, the cloud will be partially condensed and the expansion bimodal. By evaporating until the thermal cloud is no longer visible we ensure an essentially pure BEC of some 2×10^5 $F = 1$ atoms.

The cloud images can be used to measure characteristics of the trap for $F = 1$ atoms. The trap frequency is measured by observing parametric heating, sending a small modulation current (0.5 A) through one of the axial helper coils and observing atom loss from the BEC. With this method a radial trap frequency of $2\pi \times 395(3)$ Hz is found at $B_0 = 1.2$ G.

The lifetime of this cloud after an initial period of rapid loss is seen to be much longer than the sub-1 s lifetime of an $F = 2$ cloud but is still found to be less than the magnetic trap lifetime which is almost one minute. There are two main processes which can speed the decay of the Bose Einstein condensate, particularly at higher densities. The first is three-body recombination which occurs when three atoms of the condensate collide with one another, where two of the three atoms combine and

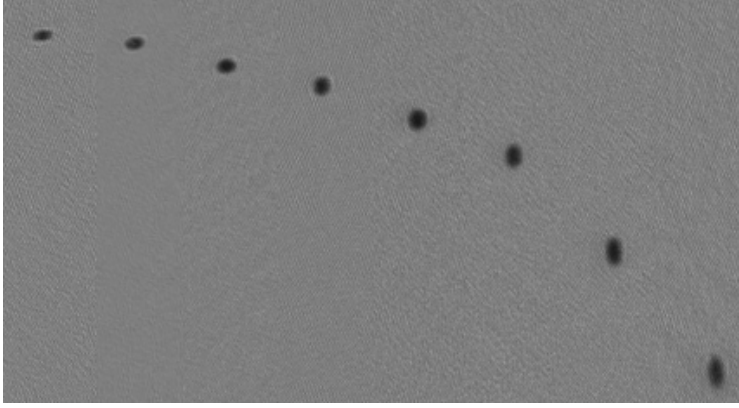


Figure 4.4: Time of flight (TOF) images of a pure $F = 1$ BEC show development of anisotropic expansion with increasing TOF from left to right from 1 ms to 25 ms.

the third carries away the binding energy as kinetic energy and so is lost from the trap [60]. Three body decay in condensate atom number can be written as

$$\frac{dN}{dt} = -L \int n^3(r) d^3r = -L \langle n^2 \rangle N \quad (4.1)$$

where $\langle \eta \rangle = \int \eta(r) n(r) d^3r / N$ for any function η . This decay mechanism thus occurs proportional to the square of the condensate density n^2 with coefficient of decay L . The second decay process is two body spin relaxation, which can occur due to the probability of a collision between two condensate atoms causing a spin flip out of the trapped state. This decay can be written

$$\frac{dN}{dt} = -G \int n^2(r) d^3r = -G \langle n \rangle N \quad (4.2)$$

and thus occurs directly proportionally to the condensate density $n(r)$ with coefficient G .

It is easier to measure condensate numbers accurately than exact density distributions of the condensate. Following [61], we use the Thomas-Fermi approximation of a parabolic condensate density distribution to express the condensate density and its square in terms of N , the condensate atom number. Thus $\langle n \rangle = c_2 N^{2/5}$ and $\langle n^2 \rangle = c_3 N^{4/5}$ with $c_2 = (15^{2/5}/(14\pi))(m\bar{\omega}/\hbar\sqrt{a})^{6/5}$ and $c_3 = (7/6)c_2^2$, where a is the scattering length and $\bar{\omega}$ is the geometric average of the trap frequencies. The dynamic range of our data is insufficient to fit both processes so we adding a single-body

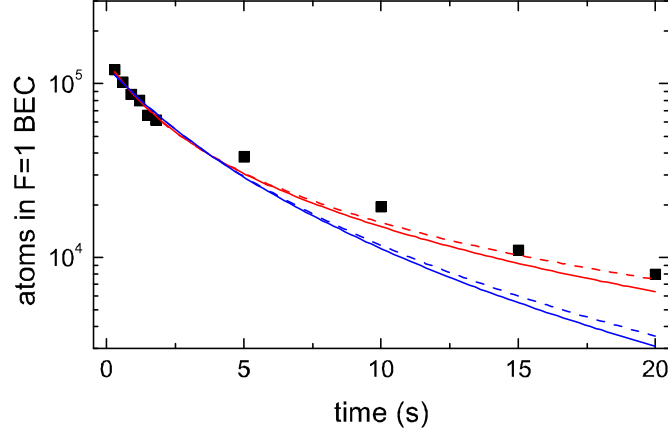


Figure 4.5: Number of atoms in a $|1, -1\rangle$ near pure BEC with $B_0 = 0.9$ G versus time. The solid red line shows the fit to the data for the combination of a three-body decay process along with a lifetime due to background collisions $\tau = 45$ s. The dashed red line shows a fit with the same function but with an infinite lifetime. The solid and dashed blue curves show fits to a two body process with a 45 s and an infinite lifetime background decay constant respectively.

contribution to each equation to give

$$\frac{1}{N} \frac{dN}{dt} = -Lc_3 N^{4/5} - \frac{1}{\tau} \quad (4.3)$$

$$\frac{1}{N} \frac{dN}{dt} = -Gc_2 N^{2/5} - \frac{1}{\tau} . \quad (4.4)$$

The value τ represents a lifetime due to other density independent decay processes such as scattering from thermal atoms or external heating of the cloud. Integrating these equations, we find the general form

$$N = \frac{N_0}{((1 + k_i \tau) e^{t/m\tau} - k_i \tau)^m} \quad (4.5)$$

where N_0 is the initial atom number, and $k_i = (N_0)^{9/5} Lc_3$, $m = 5/4$ and $k_i = (N_0)^{7/5} Gc_2$, $m = 5/2$ for the three body and two body respectively. Fitting these equations to our data, we find for both cases that the influence of τ is actually very slight and to first order can be neglected (see Fig. 4.5). But for all values of τ , the three body process is clearly the better fit to the data as the two body fit deviates strongly especially for longer times. Fitting for $\tau = 45$ s, the lifetime of a thermal cloud in our magnetic trap, we find $L = 4.9(5) \times 10^{-30} \text{ cm}^6 \text{ s}^{-1}$ for the three body decay

fit. Our value for the three body decay constant thus shows reasonable agreement with the results for $F = 1$ obtained by the JILA group of $L = 5.8 \times 10^{-30} \text{ cm}^6\text{s}^{-1}$ [62]. This value is three times smaller than the rate for $F = 2$ atoms [61] and five times smaller than the decay rate for a noncondensed cloud [62] as predicted in [60]. All these aspects explain the long lived nature of the $F = 1$ condensate.

4.3.2 BEC of $|1, -1\rangle$ atoms in TOP trap

The TOP trap is employed by applying a modulating current $A_1 \cos \omega t$ to the horizontal (x-direction) pair of coils and a current $A_2 \sin \omega t$ to the vertical (y-direction) pair of coils with ω a frequency at least a decade higher than the radial trapping frequency ω_ρ of the Ioffe Pritchard trap. Two Hewlett-Packard 3310 function generators were phase locked to produce these signals. The amplitudes A_1 and A_2 were controlled by analogue outputs of the signal conditioning rack (see Section 2.9). This results in a trap axis displaced over a distance $\rho_m = B_m/\alpha$, (where B_m is the amplitude of the modulation field) and orbiting about the symmetry axis at frequency ω . As ω is generally much faster than ω_ρ , the radial oscillation frequency of the atoms in the Ioffe Pritchard trap, this results in a time-averaged effective potential with TOP trap bottom $\bar{B}_0 = (B_0^2 + B_m^2)^{1/2}$, to be described in detail in Chapter 5.

The details of the evaporative cooling in the TOP trap differ from those in the Ioffe Pritchard trap, with the effective trap minimum \bar{B}_0 taking the place of B_0 . To investigate this we produced a BEC with and without the TOP trap. Evaporating without the TOP all atoms are removed at a final RF frequency of 0.65 MHz (equivalent to 0.91 G), and a BEC is formed at a frequency of 0.67 MHz (equivalent to 0.93 G). Obviously for a TOP, the RF frequencies which correspond to the removal of all atoms and the formation of a condensate depend on the strength of the modulation field B_m . For $B_m = 0.57$ G, BEC of 8×10^5 atoms is observed at an RF frequency of 0.84 MHz (equivalent to 1.17 G) slightly above $\bar{B}_0 = 1.07$ G.

For a TOP with $B_0 = 0$, the JILA group found that the lifetime of the BEC goes to zero as B_m goes to zero [63]. With a typical bias field of 0.65 G, the lifetime is 10 s. For our experiments in the TOP trap, the lifetime is determined by \bar{B}_0 , thus B_0 can be made significantly lower without compromising lifetime, once the cloud is smaller than the radius ρ_m . Best results (highest condensate numbers) were achieved by evaporating in the magnetic trap with $B_0 = 0.65$ G and then quickly switching on the TOP with $B_m = 0.68$ G once condensation is reached. In this way condensate numbers of over a million atoms could be achieved with a cloud lifetime of about 10 s.

We also studied the effect on lifetime of the TOP frequency ω . Varying ω , clouds are shown to have progressively shorter lifetime at lower frequencies (see Fig. 4.6). A substantial BEC persists at $\omega/2\pi = 2.3$ kHz for $\omega_\rho/2\pi \simeq 0.3$ kHz such that $\omega < 8\omega_\rho$, but is unmeasurable at $\omega/2\pi = 1$ kHz where $\omega \simeq 3\omega_\rho$. In practice we use $\omega/2\pi = 8$ kHz for the remaining experiments in this chapter as this provided the

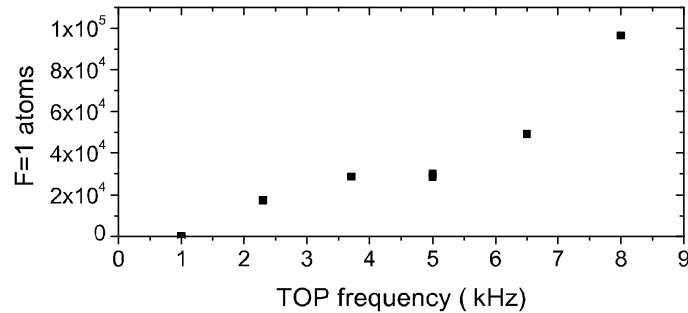


Figure 4.6: Atoms remaining after in the TOP after 2 s, plotted for various TOP frequencies. At $\omega/2\pi = 2.3$ kHz, less than 7 times the trap frequency, a sizeable cloud remains. We operate normally at a TOP frequency of 8 kHz.

highest atom number from the frequencies we tried. Enscher found that for very high TOP frequencies the lifetime begins to drop again [63] but we did not investigate this regime.

Optical Resolution

Absorption imaging doesn't work inside the magnetic trap. Therefore, to get information about the trapped condensate we tried time-of-flight imaging after negligible TOF ($< 50 \mu\text{s}$). We image along the cloud axis, far off-resonance to avoid saturation and with $10\times$ magnification to provide enough resolution. Under these conditions we measure a cloud diameter of some 10 pixels. Not surprisingly we found that proper setting of the imaging focal plane is very critical for measuring the size of the cloud. With $10\times$ magnification a 10pixel cloud width corresponds to a real space gaussian diameter of $15 \mu\text{m}$. As the calculated Thomas-Fermi diameter is much smaller ($8 \mu\text{m}$) we conclude that this method is not suited to gather information of *in-situ* clouds.

At longer time of flights (24 ms) our measured cloud sizes match well with expected values. We measure cloud widths of $96 \mu\text{m}$ and $93 \mu\text{m}$ with $4\times$ and $10\times$ imaging, which corresponds to 10^5 and 8×10^4 atoms in the condensate respectively.

The $F = 1$ double cloud

Using the axial helper coils, B_0 can be also be decreased all the way to zero. When overcompensated we produce a double well potential (see Fig.2.13). In the double well Ioffe-Pritchard trap, the condensate is very short lived due to Majorana losses, so the use of the TOP field is imperative to study the double cloud. A long-lived double condensate was produced in a manner similar to that described in [44]. The cloud was evaporatively cooled in the TOP with a trap minimum $B_0 = 0.58$ G. The

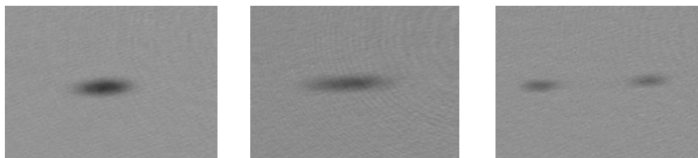


Figure 4.7: Images of clouds formed in the TOP trap with $B_0 = 0.6$ G after ramping axial helper coils to final B_0 values of -0.3 G (left), -0.4 G (middle) and -0.6 G (right). The rightmost image shows formation of a double BEC.

current in the axial helper coils was ramped in steps of 0.1 A to final values of 1.6 A, 2 A, and 2.4 A respectively corresponding to -0.3 G (left), -0.4 G (middle) and -0.6 G. We then RF evaporate in each case to 0.94 MHz. The results are shown in Fig. 4.7. For a final axial helper coil current of 2.4 A ($B_0 = -0.6$ G) this results in creation of a double BEC as evidenced by anisotropic expansion in TOF.

4.4 Vortex excitation and detection

4.4.1 BEC and vortices

It is well known that a superfluid cannot rotate as a normal fluid. As a superfluid, the BEC has a superfluid velocity which can be written as

$$\mathbf{v} = \frac{\hbar}{m} \nabla \phi \quad (4.6)$$

where ϕ is the phase of the condensate wave function. For a weakly interacting gas solutions of the Gross-Pitaevskii equation give the wavefunction of the condensate. In an axially symmetric potential

$$U_{ext}(\rho, z) = \frac{1}{2} m \omega_\rho^2 (\rho^2 + \lambda^2 z^2), \quad (4.7)$$

where λ is the trap anisotropy parameter and ρ , ϕ and z are the cylindrical coordinates, the wave function is described as $\psi_0(\mathbf{r}) = e^{i\ell\phi} |\psi_0(\rho)|$ with ℓ the angular momentum quantum number and $|\psi_0| = \sqrt{n}$, the condensate density [4].

It can be seen that the superfluid is irrotational since

$$\nabla \times \mathbf{v} = \nabla \times \nabla \phi = 0. \quad (4.8)$$

Integrating this velocity about a closed loop such as the circle described by the Thomas-Fermi radius of the cloud reveals a quantization known as the Onsager-Feynman [64, 65] condition

$$\oint \mathbf{v} \cdot d\mathbf{l} = \frac{\hbar}{m} 2\pi l \quad (4.9)$$

where l is an integer.

Consequently upon rotation of the condensate about the axis, the superfluid velocity of the rotation of the fluid is given by

$$\mathbf{v} = \frac{l\hbar}{m\rho} \mathbf{1}_\phi \quad (4.10)$$

where $\mathbf{1}_\phi$ is a unit vector in direction ϕ , which for $l \neq 0$ gives a vanishing wave function on the axis as $\rho \rightarrow 0$. Note that due to the quantization of circulation, after each closed loop, the phase of the fluid ϕ must again equal to ϕ or else differ by a multiple of 2π . These accumulations of multiples of 2π are associated with vortices, which are singularities of the wave function and appear along the axis.

Far from the axis the density must again approach its normal value n and so $|\psi_0| \rightarrow \sqrt{n}$ suggesting the introduction of a dimensionless function $f(\eta)$ such that $|\psi_0| = \sqrt{n}f(\eta)$ where $\eta = \rho/\xi$ and $\xi = \hbar/\sqrt{2mgn}$ is the healing length [4]. The function $f(\eta)$ then satisfies

$$\frac{1}{\eta} \frac{d}{d\eta} \left(\eta \frac{df}{d\eta} \right) + \left(1 - \frac{l^2}{\eta^2} \right) f - f^3 = 0. \quad (4.11)$$

Close to the axis $\eta \rightarrow 0$ and $f \sim \eta^{|l|}$, so the density n goes to zero on the axis. The signature for the presence of vortices in a condensate is this local drop in the density of the cloud. The distance over which the wavefunction increases from zero to the density of the rest of the condensate is of the order of the healing length ξ .

4.4.2 Generation of vortices

The generation of vortices in a condensate was first shown in the JILA group for a two component condensate using microwave transitions between the components and a laser beam to engineer the phase profile of the second component [28, 67, 68].

Vortices can also be created analogously to the rotating bucket experiment with liquid Helium by rotating the confining potential of the condensate. The BEC can be created in a stationary trap and rotation induced by the addition of a rotating anisotropy, before removal of the anisotropy to allow vortices to nucleate. This was first done using a laser beam to stir the cloud in the ENS group [69, 70] and used to investigate the shape of a single vortex line in a condensate [71]. Using this method the presence of a vortex state can be determined by measuring the angular momentum of the cloud by inducing quadrupole shape oscillations [72] or by dislocations in the fringe pattern following coherent splitting and recombination of a BEC [73]. Similar methods, using an optical potential to spin up the condensate were implemented at MIT [74, 75] and used to show the formation and decay of vortex lattices [76].

The Oxford group created vortices by rotating the confining potential of the condensate by purely magnetic means [30]. This method was used to measure the angular momentum associated with the vorticity by precession of the scissors mode [77]. This method was also used to study vortex lattice dynamics [78]. The same method was used by the Arizona group to create a triangular vortex lattice [79].

Another method to induce vortices in a BEC was demonstrated by the MIT group, adiabatically manipulating a magnetic bias field to imprint a phase winding on the condensate [80, 81, 82]. The JILA approach described above was later followed by experiments which used a two photon transitions to produce doubly quantized vortices [83, 84] and later vortex-antivortex superposition states [85, 86].

An alternative to rotating a ready formed BEC is to begin with a rotating thermal cloud, then evaporatively cool to condensation to produce a rotating BEC as demonstrated by the JILA group [87]. Vortex lattice dynamics were studied in detail by this group with a string of interesting results [88, 89, 90, 91, 92, 93]. This approach allows large BEC rotation rates [94] close to the trap frequency where there is large atom loss. The critical rotation regime was also investigated at ENS in attempts to reach the lowest Landau level [95, 96, 97].

More recently the number of methods used to create and study vortex behaviour in BECs has proliferated greatly. One variation is to load the BEC into an optical lattice and rotate the lattice [98]. Studies on vortices in 2D clouds (BKT regime) have also been an area of interest [97, 99, 100, 101]. The method initiated at MIT has been successfully applied to produce vortices in fermionic systems as a proof of BCS superfluidity [102, 103, 104]. This method was also used elsewhere in a series of BEC experiments to investigate quadruply charged vortices [105, 106, 107]. A novel type of manipulation was demonstrated at NIST [108] where synthetic magnetic fields impart a Berry phase to produce vortices without rotation of the condensate.

Further methods which do not require rotation of the cloud have also been developed. Notable examples have been the use of condensate splitting and recombination to create "spontaneous vortices" [109, 33, 110] as well as the use of damping and quenching [111, 112] and helical imprinting [113]. Most recently the use and modelling of quantum turbulence to induce vorticity has been highly successful [114, 115]. Other recent developments have been the discovery of vortex dipoles [116] and an interesting technique taking multiples images from a single BEC to show the development of vorticity [117].

4.4.3 Excitation by rotation in a magnetic trap

In our experiments we use a rotating magnetic potential to stir the condensate. This is done by breaking the cylindrical symmetry of the trapping potential $U_{ext}(\mathbf{r})$ as defined in Eq. (4.7) such that the radial frequencies become $\omega_- = \sqrt{1 - \epsilon} \omega_\perp$, $\omega_+ = \sqrt{1 + \epsilon} \omega_\perp$ where $\omega_\perp = \omega_\rho = \sqrt{\omega_- \omega_+}$ and ϵ is the trap anisotropy.

Applying rotation of the major axis of the potential with frequency Ω , angular

momentum can be imparted to the system. For $\Omega \simeq \omega_{\perp}$, a center of mass instability occurs. The cloud behaves analogously to a classical particle in a rotating elliptical potential and is ejected from the trap due to the coupling of the oscillation frequencies. At lower rotation frequencies the angular momentum introduced can be sufficient to induce vortices. The equation for the wave function of a condensate with a vortex can also be used to calculate the energy associated with the vortex state [4]. For a cylindrical cloud of length L and radius R this is shown to be

$$E_v = L\pi \frac{\hbar^2}{m} \ln \left(\frac{1.46}{\xi} R \right) \quad (4.12)$$

resulting in a critical angular velocity

$$\Omega_c = \frac{E_v}{N\hbar} = \frac{\hbar}{mR^2} \ln \left(\frac{1.46}{\xi} R \right) \quad (4.13)$$

For a cigar-shaped cloud, it is calculated that vorticity can appear for $\Omega \gtrsim 0.3\omega_{\perp}$ [118] and that below this value vorticity cannot be excited.

Experimentally, for low anisotropy ϵ vorticity can be induced around $\Omega = 0.7\omega_{\perp}$ [77, 69]. This is attributed to the quadrupole mode ($l = 2$) excited by the rotation of the elliptical condensate. For a small anisotropy this mode is excited at $\Omega = \omega_{\perp}/\sqrt{2}$ and induces large amplitude oscillations. These oscillations result in the dynamical instability necessary for vortex creation [119]. For larger eccentricities, the dynamical instabilities occur in a range of frequencies around $\Omega = \omega_{\perp}/\sqrt{2}$.

There are two methods to induce this instability via rotation of the magnetic trapping potential of the cloud. The first is to fix the anisotropy ϵ and slowly ramp the rotation frequency Ω . The second is to begin rotating the condensate in the normal state, cool below the condensate transition temperature and then adjust the anisotropy to form a vortex state. Both have been shown to create vortices following a settling time of some seconds [77, 33].

4.4.4 Vortex detection

For a condensate in an axially symmetric trapping potential, the vortex core can take the form of a line along the axis of the cloud. In general the size of the vortex ξ_0 is much smaller than the size of the condensate ρ_0 and so below the optical resolution of most imaging systems. The size of the cloud is expanded by time of flight imaging and in this process also the size of the vortex-generated hole in the cloud increases.

The free expansion from a trap for a cloud during time-of-flight is affected by the presence of a vortex state [66]. Defining the aspect ratio of the cloud during expansion as $A = r_{\rho}/\sqrt{2}r_z$, where r_{ρ} and r_z are the radial and axial sizes of the cloud, the ratio A_{ρ}/A_n of the aspect ratios of rotating to a non-rotating condensate can be calculated. This calculation depends on anisotropy parameter λ used in Eq. (4.7) and

the parameter Na/a_{ho} where N is the condensate atom number, a is the scattering length and $a_{ho} = \sqrt{\hbar/m\bar{\omega}}$ is the harmonic oscillator length scale with $\bar{\omega}$ the geometric average of the trap frequencies ω_x , ω_y and ω_z .

For an isotropic trap ($\lambda = 1$), the deviations from a ratio of $A_\rho/A_n = 1$ are shown to be very slight for all but the smallest cloud atom numbers. For a cigar shaped trap such as ours where $\lambda \sim 0.05$, and $Na/a_{ho} = 100$ (corresponding to 5×10^4 atoms in the condensate), the aspect ratio can be increased by up to 25%.

The development of the size of the vortex core is also shown to be dependent on the parameter Na/a_{ho} . For $Na/a_{ho} = 20$ the vortex core size ρ_i grows from 0.2ρ up to 0.25ρ during 25 ms TOF expansion. For our numbers, the vortex core corresponds to about 0.06ρ or about $15 \mu\text{m}$ after the expansion associated with a 25 ms time-of-flight, and so should be just observable with the imaging system outlined in Chapter 3.

4.5 Experiments rotating the TOP

Previous work [35] suggested a method to produce vortices with the aid of a rotating *linear* TAP (time averaged potential). In combination with a Ioffe-Pritchard trap ($B_0 > 0$) this produces a rotating elliptical potential. This idea can be generalized for arbitrary B_0 by adding a *rotating* elliptical TOP (time-averaged orbiting potential) to the IP trap. For $B_0 > 0$ this is very similar to the rotating linear TAP and for $B_0 < 0$ it gives rise to a pair of rotating elliptical TOP traps. The equation for the TOP field can be written as:

$$\begin{aligned} B_X &: A \cos \omega t \cos \Omega t - B \sin \omega t \sin \Omega t \\ B_Y &: A \cos \omega t \sin \Omega t + B \sin \omega t \cos \Omega t \end{aligned} \quad (4.14)$$

where $\omega/2\pi = 8 \text{ kHz}$ is the frequency of the TOP, Ω is the frequency of rotation of the elliptical potential and the amplitudes A and B can be set in the range $0 - 1.2 \text{ G}$. The resulting radial anisotropy of the total potential (IP trap plus TOP trap) is defined as

$$\varepsilon = \frac{\omega_+^2 - \omega_-^2}{\omega_+^2 + \omega_-^2}, \quad (4.15)$$

where ω_+ and ω_- are the major and minor frequencies of our total potential, respectively. For $A = B$ the TOP field is circular; for $A > B$ it is elliptical with the major axis in the direction $\theta = \Omega t$. For $B = 0$, the TOP field corresponds to the TAP field mentioned above. In this manner we can produce an anisotropy of up to $\varepsilon = 0.25$. The signals $A \cos \omega t$ and $B \sin \omega t$ were produced by the Hewlett-Packard 3310 function generators also used to produce the circular TOP, while the factors $\sin \theta$ and $\cos \theta$ were generated from a Krohn-Hite function generator. The outputs of these function generators were then multiplied with a pair of AD835 multipliers to produce the final inputs to the current supplies. Technical details are found in

Section 2.7. A possibility to trim the offset of the multiplier output was included to avoid wobbling of the trap axis and the associated heating.

4.5.1 Results with radial imaging

Imaging from the radial direction is used to establish the properties of the BEC. This imaging is set up for a large field of view to enable convenient TOF imaging. We can follow the evolution of the cloud shape over a maximum of 27 ms. First we produced a BEC in a circular TOP with $A = B = 0.68$ G rotating at an angular frequency Ω . For this we used the same method described for the ordinary circular TOP ($\Omega = 0$). Ramping the amplitude B to 0.45 G in 15 ms did not result in significant loss of the condensate. The latter condition corresponds to an anisotropy $\varepsilon \simeq 0.14$, $\omega_{\perp}/2\pi = 294$ Hz with $\omega_{+}/2\pi = 316$ Hz, $\omega_{-}/2\pi = 272$ Hz. The measured trap frequency was $\omega_{\perp}/2\pi = 300(10)$ Hz. This frequency was measured by varying the spinning frequency Ω and observing the atom loss. We also measured substantial losses when spinning a circular TOP, which is an indication of residual anisotropy. In this way we measured $\omega_{\perp}/2\pi = 290(10)$ Hz for $A = B = 0.68$ G and $\omega_{\perp}/2\pi = 310(10)$ Hz for $A = B = 0.45$ G. In Fig. 4.8 we show our results for the trap losses in the rotating TOP. The spinning frequency Ω is normalized to the measured radial trap frequency. We not only observe a loss dip at $\Omega = \omega_{\perp}$, but also at $\Omega = 0.5\omega_{\perp}$ and $\Omega \simeq 2\omega_{\perp}$. These results suggest that we were not successful in completely removing the presence of anisotropy possibly due to the presence of gravitational sag.

As explained in Section 4.4.2, the optimal frequency range to produce a vortex under these conditions is around the quadrupole excitation frequency $\Omega \simeq \omega_{\perp}/\sqrt{2} \simeq 2\pi \times 220$ Hz, so we concentrated our search at TOP frequencies in the range 170 – 230 Hz. For this purpose amplitude A was again set to 0.68 G, while B was first set at 0.68 G to produce a condensate and then ramped down to 0.45 G. Measurements were done for spinning times $t_{spin} = 30$ ms, 300 ms, and 1300 ms. After each spinning period the BEC was still found to be intact. This was also the case for the linear TAP ($\varepsilon \simeq 0.25$). The estimated BEC lifetime while stirring at $\Omega/2\pi = 230$ Hz was 3.7 s, long enough for vortices to form according to the literature [77, 33].

With this procedure we observed some indications of vorticity by looking at the aspect ratio of the cloud after a fixed TOF (see Table 4.1). We find that when no radial anisotropy is introduced to cloud ($A = B$) the aspect ratio of the cloud is independent of Ω . Then at $\Omega/2\pi = 230$ Hz, for $B = 0.45$ G we see an increase by some 16% in the aspect ratio as we spin for longer times, corresponding well with the predictions of Lundh et al [66].

4.5.2 Results with axial imaging

The drawback to the large field of view of our radial imaging set-up is that resolution is not good enough to see details such as vortex lines. Therefore to search for vortices

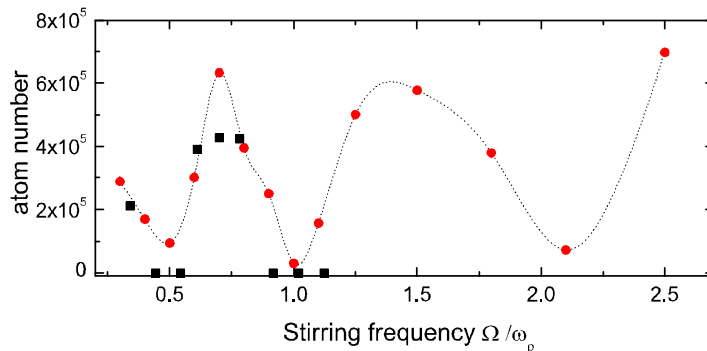


Figure 4.8: Atom number remaining trapped after 30 ms residence in a TOP with low anisotropy stirred at various frequencies Ω plotted in terms of the radial trap frequency ω_p . Red circles show results from 3 sets of experiments; stirring frequencies are normalized to the trap frequency and the data points binned and averaged. The dotted line is a guide to the eye. Black squares show atom numbers for a large anisotropy TOP.

we used axial imaging. In this way the imaging is along the vortex axis and the appropriate magnification can be selected with microscope objectives. To check that the elliptical stirring is really taking place, we cool a cloud in a TOP with a stable and large anisotropy $A = 0.1$ G, $B = 0.5$ G, corresponding to $\omega_+/2\pi = 380$ Hz, $\omega_-/2\pi = 293$ Hz and an anisotropy $\varepsilon = 0.25$. We then set the major axis at an angle $\theta = 0, 45^\circ$ and 90° and evaporate to a temperature just above T_c . Imaging with a TOF $\leq 50 \mu\text{s}$, we find elliptically shaped thermal clouds with the major axis reproducing the three angle settings of θ .

Using axial imaging we tried to excite vortices with an elliptical TOP spinning at $\Omega/2\pi = 230$ Hz for $t_{spin} = 30$ ms, 300 ms, and 1300 ms. In all cases the imaging was done by ramping back to circular conditions in 15 ms and using a 24 ms TOF. However, no vortices were observed in these measurements. We then varied the modulation frequency Ω , set the spinning time $t_{spin} = 1300$ ms and returned for times $t_{hold} = 200$ ms, 500 ms, 700 ms to the circular TOP. We then imaged with $4\times$ and $10\times$ magnification. The number of photons per pixel is inversely proportional

Table 4.1: Ratio of aspect ratio for a nonrotating to a rotating condensate.

$\Omega/2\pi$	B	t_{spin}	A_r/A_n
100 Hz	0.68 G	300 ms	1
230 Hz	0.68 G	300 ms	1.0
230 Hz	0.45 G	300 ms	1.12
230 Hz	0.45 G	1300 ms	1.16

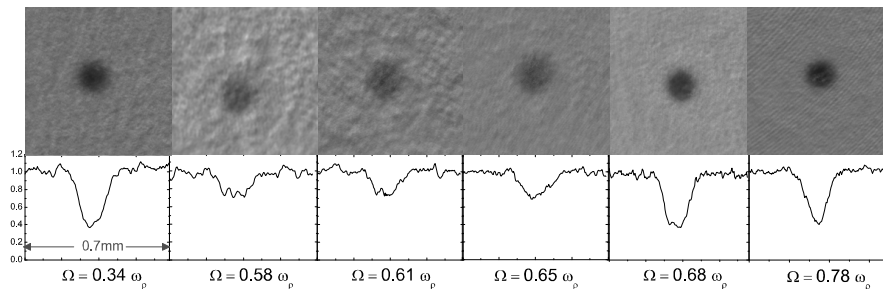


Figure 4.9: Above: Images taken after 20 ms TOF and imaged with $4\times$ magnification. Below: corresponding profiles through the cloud showing optical density. At $0.34\omega_\rho = 2\pi \times 100$ Hz and above $0.68\omega_\rho = 2\pi \times 200$ Hz absorption is high but no evidence of vortices is present. At $0.58\omega_\rho$, $0.61\omega_\rho$ and $0.65\omega_\rho$ absorption is lower due to atom loss close to half the trap frequency but dips in absorption several pixels wide point to possible onset of vortices.

to the magnification and so was quite low with $10\times$ magnification. In the trade-off between signal to noise and resolution $4\times$ magnification was found to be optimal. Between $\Omega/2\pi = 200$ Hz and $\Omega/2\pi = 230$ Hz the cloud could be imaged with both $4\times$ and $10\times$ magnification but no vortices were observed. Below 200 Hz identification of vortices was difficult due to the loss dip around $\Omega = 0.5\omega_\perp$. The cloud was lost entirely by spinning at $\Omega/2\pi = 160$ Hz, which corresponds to $0.5\omega_+$. Some indications for vorticity were present in certain images at $\Omega/2\pi = 170$ Hz, 180 Hz and 190 Hz. These images show drops in absorption over areas of several pixels in diameter corresponding to about 5% of a cloud diameter. The frequencies mentioned correspond to $0.6\omega_\perp - 0.65\omega_\perp$ where the onset of vorticity could be expected. However in this frequency range losses already limit the contrast and makes it difficult to be conclusive. Possible vortex depth is less than 20% and reproducibility of vortex number for a given frequency is poor. Looking at the radial size of the cloud in these images suggests also some evidence for vorticity but is inconclusive.

4.5.3 Conclusions

We can speculate that curving of the vortex along the imaging axis might obscure the visibility of the contrast. However, our aspect ratio is comparable to those used in experiments on vortex shape at ENS, where despite evident bending of the vortex lines, vortices could still be imaged head on [69]. The lack of observation of a vortex above $\Omega/2\pi = 200$ Hz corresponding to $\Omega = 0.68\omega_\rho$ (where losses are minimal) leads to a conclusion that no vortices could be reliably nucleated. A possible reason for the lack of vortices is the radial anisotropy of the TOP which is circular to no better than 1 part in 80. Several authors suggest significantly better homogeneity is

necessary in order to nucleate vortices, as high as 1 in a 1000 is used in nucleation experiments at JILA [120]. It is also unclear what role the uncontrolled switch-on of the TOP field had on the reproducibility of these experiments. We changed our apparatus to produce a more reliable TOP field for the experiments described in Chapter 5 but did not repeat the search for vortices.

Chapter 5

Manipulation using phase jumps of the TOP

This chapter has been published in Ref. [121] Physical Review A 82 (2010) 063635.

5.1 Introduction

Time averaged potentials (TAP) offer a versatile tool for trapping both charged and neutral particles. For neutral atoms the most common example in this class of traps is the Time-averaged Orbiting Potential (TOP) which was used in the experiments in which the first Bose-Einstein condensate (BEC) was created [16, 14]. The TOP trap consists a magnetic quadrupole trap [10, 122] shifted by a uniform magnetic modulation field rotating at a high (audio) frequency. As this rotation is slow as compared to the Larmor precession of the atomic magnetic moments, the atoms remain polarized with respect to the instantaneous effective magnetic field [18] as follows from the adiabatic theorem. On the other hand the rotation is fast as compared to the orbital motion of the atoms. As a consequence, the atomic motion consists of a fast rotating part (micromotion), superimposed on a slow oscillating part (macromotion). In the simplest theoretical description, the static approximation, the micromotion is eliminated by time-averaging the instantaneous potential over a full cycle of the modulation field.

Suppose we load a particle with given momentum \mathbf{p}_0 at position \mathbf{r}_0 in a TOP trap using a sudden switch-on procedure. One might naively guess that the ensuing motion is given by the dynamics in the time-averaged potential, subject to the initial conditions $\mathbf{r} = \mathbf{r}_0$ and $\mathbf{p} = \mathbf{p}_0$ but this guess turns out to be wrong. In fact, one can show that the initial conditions for the slow motion depend on the phase of the TOP at the time of switch-on. This phenomenon was analyzed by Ridinger and coworkers [42, 43] for the special case of a one-dimensional rapidly oscillating potential (ROP) with zero average. Ridinger et al. also showed, first for a classical particle [42] and subsequently for the quantum case [43], that the amplitude and energy associated

with the slow motion can be altered by applying a suitable phase jump in the rapidly oscillating field.

In this paper we show, both theoretically and experimentally, that the dependence on initial phase and the possibility to influence the motion by phase jumps, is also present for a two-dimensional rotating TOP field. In particular we show that a cloud of atoms which is initially at rest with zero momentum acquires a sloshing motion as soon as the TOP is suddenly switched on. This is true even if the cloud is initially at the minimum of the effective potential. The amplitude of this slow macromotion is much larger than that of the fast micromotion while the direction of sloshing depends on the TOP phase at switch-on. We also demonstrate that this macromotion can be almost entirely quenched by applying a carefully timed and sized phase jump in the TOP field.

The motion of atoms and ultracold atomic clouds in TOP traps have been extensively described in the literature. Following the achievement of the first BEC [14], the use of the axially symmetric TOP was described theoretically in [24, 25, 27, 26, 41, 40] and explored experimentally by other groups [19, 31, 20, 32, 21, 33] to study properties of the BEC. The idea of the TOP was extended to an asymmetric triaxial TOP trap developed by [31] and also used by other groups [32, 33]. Further a number of other variations were introduced: In many cases, it turns out to be convenient to switch on the TOP after a preparative stage of cooling in a conventional static trap such as a magnetic quadrupole trap (see e.g. [31]), an optically plugged magnetic quadrupole [34] and Ioffe-configurations [35, 36, 37]. Often, the transfer of the cloud from the static to the TOP trap cannot be performed adiabatically for topological reasons. Bearing this in mind, it becomes relevant to carefully analyze the dynamics that may be induced by a sudden switch-on of the TOP. In addition, applications which require manipulation of a BEC are heavily dependent on precise control of the location of the atomic cloud and can thus benefit from the techniques described.

In our experiments the condensate is prepared in a Ioffe-Pritchard (IP) trap before transferring to a TOP. This procedure induces the above mentioned ‘sloshing motion’. Although our method is very specific, it is typical for any sudden change of a TOP geometry in amplitude and/or phase. In our case the transfer was chosen because the use of radio-frequency (rf) induced evaporative cooling is more efficient in a static magnetic trap than in a TOP. Once transferred to the TOP we can create trapping geometries that are difficult to realize using a static magnetic potential without introducing Majorana losses associated with the presence of zero-field points. An example is the double well potential used in [35].

The remainder of this paper is organized as follows. In Section 5.2 we calculate the motion of a cloud of atoms in a TOP which at switch-on is at rest at the center of the trap. We discuss the motion that results and derive the conditions under which a phase jump can lead to a substantial reduction of the energy associated with the slow motion of the cloud. In Section 5.3 we discuss the experimental details and the preparation of the BEC and its transfer to the TOP. In Section 5.4 an

analytic model to describe the effects of the switch-on of the TOP is developed by approximating it with a sudden step. In Section 5.5 we present the experimental results and compare with the theory of Section 5.2. Finally in Section 5.6 we give a summary and conclusion.

5.2 Theory

5.2.1 Time-averaged Ioffe-Pritchard potential

In the literature the term TOP is most often used for a spherical-quadrupole trap combined with a rotating uniform magnetic modulation field. In this paper we will use the term TOP in a broader context, to include the magnetic trapping potential created by combining a IP trap with rotating modulation field. Challis et al. [40] have shown that the dynamical eigenstates of a degenerate Bose gas in a TOP are given by solutions of the usual Gross-Pitaevskii equation but taken in a circularly translating reference frame, that is, a reference frame the origin of which performs a rapid circular motion but retains a constant orientation. In particular this implies that the center of mass of a condensate in its ground state performs the same micromotion in a TOP as a point particle with the magnetic moment of an atom. In this spirit we use as a ^{87}Rb condensate to study the micromotion and macromotion in a TOP.

We consider a cigar-shaped Ioffe-Pritchard potential [123, 122, 124]

$$U(\boldsymbol{\rho}, z) = \mu \sqrt{\alpha^2 \rho^2 + (B_0 + \frac{1}{2}\beta z^2)^2}, \quad (5.1)$$

where $\boldsymbol{\rho}(t)$ is the radial position of a test atom with respect to the IP symmetry axis, μ the magnetic moment of the atom, and α, β, B_0 the parameters for the radial gradient, the axial curvature and offset value of the IP magnetic field. Eq.(5.1) represents an approximate expression for the IP trap which is valid for $\alpha^2 \gg \beta B_0$ and in the limit $\rho \ll \alpha/\beta$ [123, 122, 124].

In the presence of the TOP field we transform to the circularly translating frame [40] and have

$$\boldsymbol{\rho}(t) = \{x - \rho_m \cos(\omega t + \phi_m), y - \rho_m \sin(\omega t + \phi_m)\}, \quad (5.2)$$

where $\{x, y, z\} \equiv \{\boldsymbol{\rho}, z\} \equiv \mathbf{r}$ is the position of the atom in the laboratory frame and the IP symmetry axis is displaced over a distance $\rho_m = B_m/\alpha$ in the direction

$$\hat{\boldsymbol{\rho}}_m = \{\cos(\omega t + \phi_m), \sin(\omega t + \phi_m)\} \quad (5.3)$$

by the uniform modulation field

$$\mathbf{B}_m = B_m \{\cos(\omega t + \phi_m), -\sin(\omega t + \phi_m)\} \quad (5.4)$$

applied perpendicular to the z axis. The y axis is taken along the vertical direction, the xz plane being horizontal. The modulation field \mathbf{B}_m rotates at angular frequency $-\omega$ (phase $-\phi_m$) about the horizontal z axis as illustrated in Fig. 5.1. Notice that the sense of rotation of the IP-field-minimum is opposite to that of the \mathbf{B}_m field, in contrast to the original TOP configuration [16], where the field-zero rotates in the same direction as the bias field. This reflects the difference between the 2D-quadrupole symmetry of the IP trap and the axial symmetry of the spherical-quadrupole trap. The rotation of the modulation field \mathbf{B}_m also gives rise to a fictitious field \mathbf{B}_ω which has to be added or subtracted from the offset field \mathbf{B}_0 , depending on the sense of rotation,

$$\mathbf{B}_0 \rightarrow \mathbf{B}_0(1 \pm \mathbf{B}_\omega/\mathbf{B}_0) = \mathbf{B}_0(1 \pm \omega/\omega_L), \quad (5.5)$$

where $\omega_L = g_F \mu_B B_0 / \hbar$ is the Larmor frequency of magnetic moment of the atoms, with g_F the hyperfine g factor and μ_B the Bohr magneton. In a standard TOP, the fictitious field in combination with gradient of the quadrupole field gives rise to a shift of the equilibrium position of the cloud in the direction of the axis around which the field rotates [18, 32]. In our IP-TOP the axial field is homogeneous near the origin and the shift is absent; the change in B_0 turns out to be small and will be neglected in this paper.

For $\beta = 0$ and $B_0 = 0$ the potential $U(\boldsymbol{\rho}, z)$ corresponds to that of a two-dimensional quadrupole field with a zero-field line that rotates at distance ρ_m about the z axis as a result of the modulation. For $B_0 = 0$ the distance ρ_m is known as the radius of the ‘circle of death’. For $B_0 < 0$ the potential corresponds to two TOP traps separated by $\Delta z = 2(2|B_0|/\beta)^{1/2}$ [35]. In this paper we will consider only the case $B_0 \geq 0$.

In the common description of the TOP one analyzes the motion in an effective potential, obtained by time averaging the static trap over a full rotation period of the \mathbf{B}_m field. For Eq. (5.1) this procedure yields the effective potential

$$\mathcal{U}(\mathbf{r}) = \frac{1}{2\pi} \int_0^{2\pi} U(x - \rho_m \cos \zeta, y - \rho_m \sin \zeta, z) d\zeta, \quad (5.6)$$

where $\zeta = \omega t + \phi_m$. For the cigar-shaped IP potential we consider the condition

$$\omega \gg \Omega_\rho \gg \Omega_z, \quad (5.7)$$

where, for an atom of mass m , the quantity $\Omega_z = (\mu \beta / m)^{1/2}$ is the axial harmonic oscillation frequency in the effective potential $\mathcal{U}(0, 0, z)$. Analogously, harmonic oscillation frequency in the radial plane is given by

$$\Omega_\rho = \sqrt{\frac{\mu \alpha^2}{m \bar{B}_0} (1 - \frac{1}{2} B_m^2 / \bar{B}_0^2)} \equiv \Omega, \quad (5.8)$$

where $\bar{B}_0 = (B_0^2 + B_m^2)^{1/2}$ is offset value of the effective potential at the origin [35].

The first inequality in Eq. (5.7) ensures that the fast and slow radial motions of the atoms can be separated, which is the well-known operating regime for a TOP trap [16]. The second inequality implies that the axial motion in the effective trap is slowest and that the motion can be treated as quasi two-dimensional in the radial plane.

To account for the acceleration due to gravity (g), the gravitational potential $mg y$ has to be added to Eqs. (5.1) and (5.6). The main effect is to shift the minimum of the potentials in the negative y direction by the amount

$$\Delta y = g/\Omega^2. \quad (5.9)$$

This expression holds as long as the gravitational sag Δy is much smaller than the harmonic radius $\rho_h \equiv \bar{B}_0/\alpha$.

Since $\rho_h \geq \rho_m$, the effective potential (5.6) may be treated as harmonic as long as the motion is confined to a region around the z axis that is small compared to ρ_m . For our experiment the harmonic approximation holds rather well and is sufficient for gaining qualitative insight in the micro- and macromotion as will be shown in Section 5.2.2. Refinements associated with switch-on transients and gravity are discussed in Section 5.4. In the numerical analysis of Section 5.2.3, we solve the classical equations of motion in the full time-dependent potential Eq. (5.1). In this context we also comment on the validity of the harmonic approximation.

5.2.2 Micromotion and macromotion

To analyze the effect of switching on the \mathbf{B}_m field at $t = 0$ we first consider an atom ‘at rest’ in the center of the effective trapping potential $\mathcal{U}(\boldsymbol{\rho}, z)$. Such an atom exhibits no period-averaged dynamics (no macromotion) but only circular micromotion at a frequency ω about the origin as illustrated in Fig. 5.1. The radius of this stationary micromotion,

$$\rho_0 = \frac{\mu\alpha}{m\omega^2} (1 + B_0^2/B_m^2)^{-1/2}, \quad (5.10)$$

follows from the condition $F_c = m\omega^2\rho_0$ for the centripetal force $\mathbf{F}_c = -\nabla_{\boldsymbol{\rho}}U|_{\rho=0} = \mu\alpha(1 + B_0^2/B_m^2)^{-1/2}\hat{\boldsymbol{\rho}}_m$. The speed of this stationary micromotion,

$$v_0 = \omega\rho_0 = \frac{\mu\alpha}{m\omega} (1 + B_0^2/B_m^2)^{-1/2}, \quad (5.11)$$

is directed orthogonally to the direction $\hat{\boldsymbol{\rho}}_m$. Such pure micromotion only results if at $t = 0$ the atom is already moving at speed v_0 along a circle of radius ρ_0 about the origin and is located at position $\boldsymbol{\rho} = -\rho_0\hat{\boldsymbol{\rho}}_m$ (see Fig. 5.1). Obviously an atom at $t = 0$ at rest at the origin, $\boldsymbol{\rho} = \{0, 0\}$ does not satisfy these initial conditions and as a consequence its macromotion will start with a finite launch speed. We will see that the result is elliptical motion at frequency Ω , with the long axis approximately perpendicular to the initial direction of $\hat{\boldsymbol{\rho}}_m$ and with a substantial amplitude, of

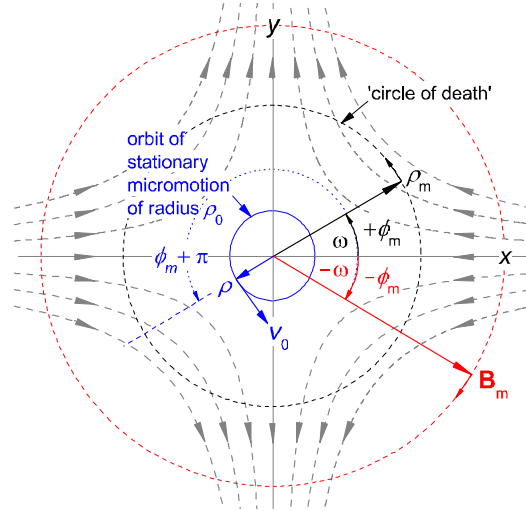


Figure 5.1: Diagram of the magnetic field configuration in relation to the orbit of stationary micromotion (solid blue circle). The view is along the (horizontal) z axis. The orbital position and velocity of the micromotion are denoted by $\boldsymbol{\rho} = -\rho_0 \hat{\boldsymbol{\rho}}_m$ and v_0 . The IP symmetry axis rotates at frequency ω (with initial phase ϕ_m) about the z axis on the circle of radius ρ_m (dashed black circle). Note that the TOP field $\mathbf{B}_m = B_m \hat{\boldsymbol{\rho}}_m$ rotates at frequency $-\omega$ (phase $-\phi_m$), reflecting the 2D-quadrupole symmetry (dashed red circle) of the IP trap.

order $(\omega/\Omega) \rho_0$. Usually this motion is undesired and our aim is to quantify it and subsequently quench it by imparting a phase jump to the TOP-field.

It is worth mentioning that in the conditions relevant for the experiments described below the amplitude and energy of the macromotion are not negligible compared to other relevant length and energy scales. The characteristic size of the condensate is given by the Thomas Fermi radius which turns out to be slightly smaller than the macro motion amplitude. Likewise, the energy associated with the macromotion is at least as large as the chemical potential.

To gain insight into the way in which the sudden switch-on of the TOP influences the macromotion of an atom initially at rest at the origin, we first consider a simple model in which it is assumed that the motion in the radial plane can be decomposed into two harmonic components, oscillating at the micromotion and macromotion fre-

quencies ω and Ω , respectively. The position $\boldsymbol{\rho}(t)$ and velocity $\dot{\boldsymbol{\rho}}(t)$ are given by

$$\begin{aligned} \boldsymbol{\rho}(t) = & \{\rho_0 \cos(\omega t + \phi), \rho_0 \sin(\omega t + \phi)\} + \\ & + \{X_0 \cos(\Omega t + \varphi_x), Y_0 \sin(\Omega t + \varphi_y)\} \end{aligned} \quad (5.12)$$

$$\begin{aligned} \dot{\boldsymbol{\rho}}(t) = & \{-v_0 \sin(\omega t + \phi), v_0 \cos(\omega t + \phi)\} + \\ & + \{-V_{0,x} \sin(\Omega t + \varphi_x), V_{0,y} \cos(\Omega t + \varphi_y)\}, \end{aligned} \quad (5.13)$$

where X_0 (Y_0) is the amplitude, $V_{0,x} = \Omega X_0$ ($V_{0,y} = \Omega Y_0$) the velocity amplitude and φ_x (φ_y) the initial phase of the macromotion in x (y) direction; ϕ is the initial phase of the micromotion. The atom starts at rest at the origin, hence the initial conditions are $\boldsymbol{\rho}, \dot{\boldsymbol{\rho}} = 0$ at $t = 0$. If the condition

$$\omega \gg \Omega \quad (5.14)$$

is satisfied, the acceleration due to the micromotion dominates over that of the macromotion. The total acceleration may be approximated by $\ddot{\boldsymbol{\rho}} \simeq \mathbf{F}_c/m$. In other words, $\ddot{\boldsymbol{\rho}}$ points in the direction $\hat{\boldsymbol{\rho}}_m$, which is opposite to the direction of $\boldsymbol{\rho}$ (as per Fig. 5.1). Hence, the initial phase of the micromotion is $\phi \simeq \phi_m + \pi$, where ϕ_m is fixed by the phase of the rotating \mathbf{B}_m field [125]. Without loss of generality we can set $\phi_m = 0$, which means that $\hat{\boldsymbol{\rho}}_m$ is oriented along the positive x direction at $t = 0$. With this choice and setting $\phi = \phi_m + \pi$, we find from the initial conditions: $\varphi_x, \varphi_y = 0$, $X_0 = \rho_0$, and $Y_0 = (\omega/\Omega)\rho_0$. Substituting these values in Eq. (5.12) we obtain an equation for the macromotion representing an elliptical orbit with its major axis oriented perpendicular to the instantaneous direction $\hat{\boldsymbol{\rho}}_m$ of the \mathbf{B}_m field at $t = 0$. Since the amplitude of the macromotion along its major axis is larger than the micromotion by the factor ω/Ω , a substantial sloshing motion results from the sudden switch-on. Note that with increasing ω , the micromotion amplitude ρ_0 decreases like $1/\omega^2$ whereas the amplitude of the sloshing motion Y_0 decreases only like $1/\omega$. For this reason the sloshing cannot be neglected in most practical cases involving audio-frequency modulation.

5.2.3 Numerical analysis

To validate the analytical model introduced in Section 5.2.2, we numerically integrate the classical equations of motion in the full time-dependent potential given by Eq. (5.1) for $z = 0$, $v_z = 0$ and $\phi_m = 0$. The result for the trajectory is given in Fig. 5.2 and exhibits the sloshing macromotion described above. The choice of parameters is such that it matches the experimental conditions that will be presented in Section 5.3.

The drawn black lines in Fig. 5.2 correspond to sudden switch-on of the TOP trap at $t = 0$ for an atom initially at rest at the origin in the absence of gravity. The figure clearly shows the micromotion superimposed onto the macromotion orientated along the y direction. The amplitudes and phases of the macromotion obtained by

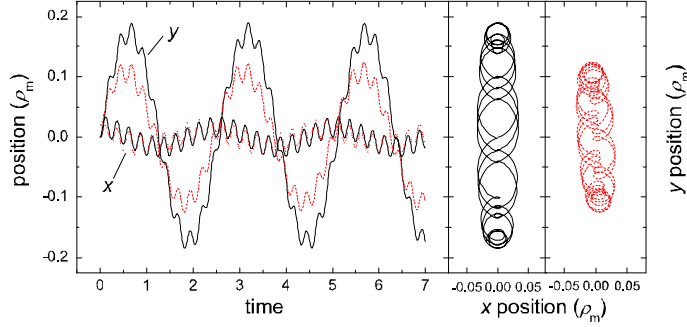


Figure 5.2: Numerically calculated trajectories in the xy plane with the x - and y -positions shown against time (left) and parametric plots of the same trajectory in the xy plane (middle and right) of a particle initially at rest at the origin, after instant switch-on (black lines). The dotted red curves correspond to a switch-on time of $3 \mu\text{s}$ of the TOP field, a settling time for the value of B_0 as well as the presence of gravity. The trap frequencies are $\omega/2\pi = 4 \text{ kHz}$ and $\Omega/2\pi = 394 \text{ Hz}$. Units are scaled to the TOP radius ρ_m .

Table 5.1: Comparison of numerical results (num) with the analytical model (AM); +ab - including refinements (a) and (b); +abc - all refinements included

	ϕ_m	θ/π	φ_x/π	φ_y/π	X_0/ρ_0	Y_0/ρ_0
num	0	0	0	0	1	10.2
AM	0	0	0	0	1	10.2
num+ab	0	0.024	0.22	0.04	1.34	10.2
AM+ab	0	0.024	0.23	0.04	1.34	10.2
num+abc	0	0.017	0.20	0.06	0.82	6.5
AM+abc	0	0.021	0.23	0.06	0.85	6.5

fitting Eq. (5.12) to the results of the numerical calculation agree accurately with the analytical model of Section 5.2.2 (see Table 5.1). A more detailed comparison reveals that anharmonicities play a minor role; the harmonics of both the micro- and macromotion have amplitudes which are at least two orders of magnitude smaller than those of the fundamentals.

In order to allow a better comparison with the experiments to be discussed below we have also performed the numerical analysis including several refinements that pertain to our specific experimental situation. These effects are: (a) a difference (δy) in gravitational sag between the IP and the TOP trap; (b) an exponential switching transient of the current in the TOP coils and correspondingly in the \mathbf{B}_m field ($\tau_{1/e} = 3 \mu\text{s}$); (c) a switching transient of $\sim 0.5 \text{ ms}$ in the offset field from $B_0 = 9.5 \times 10^{-5} \text{ T}$ at the $t = 0$ to the final value $B_0 = 3.1 \times 10^{-5} \text{ T}$.

The initial gravitational sag in the IP trap is $1.2 \mu\text{m}$. When switching on the TOP, the sag Δy jumps in $\sim 3 \mu\text{s}$ to $1.7 \mu\text{m}$ and settles in $\sim 0.5 \text{ ms}$ to its final value $1.6 \mu\text{m}$ due to the decrease of B_0 . Thus the gravitational sag increases jump wise and settles at $\delta y = 0.4 \mu\text{m}$. During the same transient the radius of the stationary micromotion grows from $\rho_0 = 0.21 \mu\text{m}$ to $\rho_0 = 0.33 \mu\text{m}$ and Ω increases by about 5%.

The dotted red traces in Fig. 5.2 correspond to the numerical calculation including all the above refinements relevant to the experiments. We have also investigated the effects of gravity, \mathbf{B}_m -switching and B_0 -switching separately. We find that the main effect of the settling time of B_0 is to reduce the amplitude along the major axis by $\sim 35\%$. The combined effect of changing gravitational sag and \mathbf{B}_m transient is to slightly increase the x amplitude as well as to produce a slight tilt angle of the trajectory (see right-most panel of Fig. 5.2).

The tilt angle θ of the macromotion also follows from a fit of Eq. (5.12) to the numerical results: for known values of X_0 , Y_0 , φ_x and φ_y the angle of rotation ϑ to align the coordinate system along the major and minor axis is given by

$$\vartheta = \frac{1}{2} \tan^{-1} [2 \sin(\varphi_x - \varphi_y) X_0 Y_0 / (Y_0^2 - X_0^2)] \quad (5.15)$$

For $\phi_m = 0$ the tilt angle equals the rotation angle ($\theta = \vartheta$).

The results of a fit of Eq. (5.12) to the numerical results including only the refinements (a) and (b), as well as a fit including all three refinements (a), (b) and (c) are also given in Table 5.1. Extending the analytical model to include the refinements (a) and (b) is straightforward and given in detail in Section 5.4. The expressions for the amplitudes and phases depend on the model parameter τ_0 and are given by Eqs. (5.24)-(5.27) of Section 5.4. The model parameter τ_0 is chosen by ensuring that the value of the tilt angle θ of the model reproduces that of a fit to the numerical solution for zero settling time, $\theta = 0.024\pi$. This results in $\tau_0 = 3.5 \mu\text{s}$. Excellent agreement is obtained with the numerical model as is shown in Table 5.1. Insight in the cause of the reduction of the major-axis amplitude associated with the settling behavior of B_0 can also be gained using the analytical model. As discussed in Section 5.4 the major refinement is change the launch speed corresponding to the initially smaller value of ρ_0 . Although this refinement captures the origin of the 35% reduction of the major axis amplitude, Table 5.1 shows that the overall agreement with the numerical model is less favorable.

5.2.4 Phase jumps

Let us now analyze how the macromotion can be quenched. For a one-dimensional, rapidly-oscillating potential it was demonstrated in Ref. [42] that the amplitude of the macromotion can be quenched by an appropriate phase-jump of the modulation field. For the 2D motion in a TOP, the success of such an approach is not *a priori* obvious because the phase jumps for the x - and y motion cannot be selected independently.

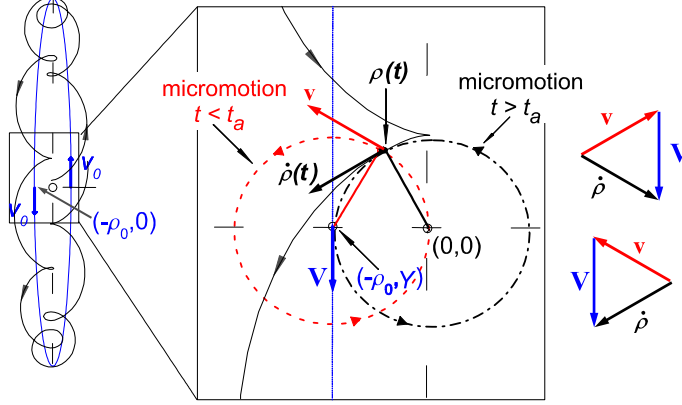


Figure 5.3: Explanatory diagram for the phase jump. Left: cloud trajectory (black solid line) along with macromotion trajectory (blue dotted line). The black dashed lines are the symmetry axes of the trap and the blue arrows show the macromotion velocity on crossing the x -axis. Middle: Expanded view of boxed region of the left panel; $\rho(t)$ is the position of the cloud at the time of the phase jump. The red dashed (black dot-dashed) circle is micromotion just before (after) the phase jump at $t = t_a$. Right: micromotion (\mathbf{v}) and macromotion (\mathbf{V}) velocity vectors add up to the total velocity vector $\dot{\rho}(t)$.

Yet, as will be shown below, also for the TOP it is possible to quench both the X_0 - and Y_0 amplitudes more or less completely by imposing a single phase jump $\Delta\phi_m$ to the \mathbf{B}_m field.

For clarity we first restrict ourselves to the case $\phi_m = 0$ and neglect the effects of gravity and switching transients. This means that the cloud is launched at $t = 0$ in the vertical y direction with a speed that is equal to v_0 , the micromotion speed. As can be seen from the trajectory depicted at the left of Fig. 3 the macromotion speed will again be equal to v_0 when the cloud returns close to the origin after an integer number of macromotion half-periods. The total velocity $\dot{\rho}(t)$ is the vector sum of the micro- and macromotion velocities and this quantity varies rapidly on a time scale of the micro-motion period.

The essence of the quenching procedure is to apply the phase jump at a time t_a chosen in the interval $t_n - \Delta t < t < t_n + \Delta t$ around times $t_n = n(\pi/\Omega)$ corresponding to a multiple of the macromotion half-period. We choose t_a such that $\dot{\rho}(t_a)$ has a magnitude equal to v_0 . When the cloud returns at the x axis the micro- and macromotion speeds are both v_0 and hence the resultant total velocity can only be equal to v_0 if the angle between the macro- and micromotion directions is either $2\pi/3$ or $-2\pi/3$ corresponding to two distinct micromotion phases $\phi_a \equiv \phi(t_a) = \omega t_{2n-1} + \phi = \pm\pi/3$ (see Fig. 3-right). In other words the micro- and macromotion velocity vectors form an equilateral triangle. For each of these cases a corresponding

phase jump exists, $\Delta\phi_m = \pm\pi/3$ respectively, such that $\hat{\rho}_m$ is set perpendicular to $\dot{\rho}(t_a)$, which sets the macromotion velocity to zero. The result is pure micromotion if the orbit into which the particle is kicked is centered around the origin. For each of the two choices of ϕ_a , pure micromotion results only if the macromotion position at the time of the phase jump is equal to $(\pm\rho_0, 0)$, where the $+$ ($-$) sign applies for even (odd) n . Complete quenching can be achieved only for specific choices of the ratio ω/Ω . The change of orbit upon a phase jump is explained pictorially in the middle of Fig. 3.

We now generalize to the case where the ratio ω/Ω is not precisely fine tuned and allow for the possibility that the macromotion speed deviates slightly from the value v_0 assumed above. One can show that, also in this case, the maximal reduction in macromotion energy resulting from a phase jump is achieved when the jump is applied at a time t_a when $\dot{\rho}(t_a)$ has a magnitude equal to v_0 . The value of $\Delta\phi_m$ is again selected such as to set $\hat{\rho}_m$ perpendicular to $\dot{\rho}(t_a)$. By a reasoning similar to the case described above we find that the condition of an equilateral triangle of the three velocity vectors is now replaced by one that is isosceles-triangle condition with the micro-motion velocity and $\dot{\rho}(t_a)$ both having a magnitude v_0 . This in turn means that the magnitude of the phase jump will deviate slightly from the values $\pm\pi/3$ found above. Also, the nearest distance to the x axis at which the isosceles-triangle condition can be met is in general not equal to zero. This means that some residual macromotion will be present after the phase jump, with an amplitude given by the distance to the origin of the center of the circular orbit into which the cloud is transferred by the phase jump. One can show that there is always a choice possible where the isosceles-triangle condition is satisfied such that this distance is approximately $2\rho_0$ or less. As a consequence, even in the worst case, the macromotion amplitude is reduced from $(\omega/\Omega)\rho_0$ to an amplitude of order ρ_0 .

The criterion that the acceleration be set perpendicular to the total velocity at the time that the macromotion speed is equal to v_0 can be expressed by the following equation:

$$\Delta\phi_m = \arctan \left[\frac{\dot{\rho}_y(t_a)}{\dot{\rho}_x(t_a)} \right] - \phi(t_a) + (-1)^k \frac{\pi}{2} \quad (5.16)$$

where $\dot{\rho}_x(t_a) = -v_0 \sin \phi(t_a) - V_{0,x} \sin(\Omega t_a + \varphi_x)$ and $\dot{\rho}_y(t_a) = v_0 \cos \phi(t_a) + V_{0,y} \cos(\Omega t_a + \varphi_y)$ are x - and y components of $\dot{\rho}$ at time t_a and $k = 1$ for $\dot{\rho}_x(t_a) > 0$ and $k = 0$ for $\dot{\rho}_x(t_a) < 0$. We return to selection of the jump time and the use of Eq. (5.16) when discussing the measurement procedure in Section 5.3.2.

Examples of the numerical calculations of the quenching procedure are shown in Fig. 5.4. The near complete quenching of the macromotion shown in panel (a) is obtained for $\delta y = 0$ and $\tau = 0$ with phase jump $\Delta\phi_m = -\pi/3$ at time $t_a = 3.834$ ms in the time interval around $t_3 = 3\pi/\Omega$. In Fig. 5.4b the refinements (a), (b) and (c) are included in the simulation of the experiment. In this case the phase jump had to be adjusted to $\Delta\phi_m = -0.22\pi$ for maximum quenching. Note that the quenching is less

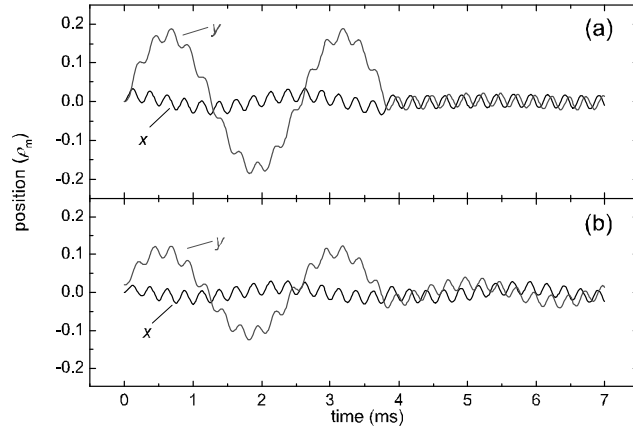


Figure 5.4: Numerically calculated radial trajectories in the x - and y direction for the same trap parameters as used for Fig. 5.2, with a quenching phase jump $\Delta\phi_m$ applied at optimized $t = t_a \simeq t_3$ (three macromotion half-periods). (a) instant switching, no gravity: $\Delta\phi_m = -\pi/3$, $t_a = 3.834$ ms; (b) including switching transients and gravity: $\Delta\phi_m = -0.22\pi$, $t_a = 3.834$ ms.

complete. By adjusting, at constant Ω , the micromotion frequency to $\omega = 4.068$ kHz and the jump time to $t_a = 3.769$ ms, complete quenching similar to that shown in panel (a) was obtained also when including all refinements in the numerical model.

5.3 Experimental

5.3.1 Apparatus

The experiments are done with the apparatus described in detail in [38] and [44]. We produce a BEC of 2.5×10^5 atoms of ^{87}Rb in the $|F = 2, m_F = 2\rangle$ state in a Ioffe-Pritchard trap using radio-frequency (rf) evaporative cooling. The symmetry axis (z axis) of the trap lies horizontal with trap frequencies ($\Omega_\rho/2\pi = 455(5)$ Hz, $\Omega_z/2\pi = 21$ Hz) and the magnetic field offset $B_0 = 9.5(3) \times 10^{-5}$ T, $\alpha = 3.53$ T/m and $\beta = 266$ T/m². The Thomas-Fermi radius of the BEC is $2.2 \mu\text{m}$. The TOP field is produced by two pairs of coils, one in the x direction, the other in the y direction as described previously in [35]. The coils consist of only two windings to keep the inductance low. The current for the TOP is generated by a TTI 4 channel arbitrary waveform generator (TGH 1244), amplified by a standard audio-amplifier (Yamaha AX-496). The current used is $I_m = 3.0$ A and the field produced is $B_m = 6.8(2) \times 10^{-5}$ T. All measurements in the TOP are done with $\Omega/2\pi = 394(4)$ Hz ($B_0 = 3.1 \times 10^{-5}$ T). Detection is done by time-of-flight absorption imaging along the

z axis using a one-to-one transfer telescope to image the xy plane onto a Princeton TE/CCD-512EFT CCD camera with $15\ \mu\text{m}$ pixel resolution. All measurements are carried out with the same flight time $\Delta t_{\text{TOF}} = 23\ \text{ms}$, giving rise to an expanded cloud radius of $\sim 140\ \mu\text{m}$.

5.3.2 Measurement procedure

Our experiments on phase-jump-controlled motion in a TOP trap are done with the \mathbf{B}_m field operated at $\omega/2\pi = 4\ \text{kHz}$. This frequency is sufficiently high ($\omega/\Omega \gtrsim 10$) to satisfy the ‘TOP condition’ Eq. (5.14). The frequency is chosen lower than in a typical TOP to ensure that the speed of the stationary micromotion, $9\ \text{mm/s}$ as estimated with Eq. (5.11), is accurately measurable. In the experiments we start with an equilibrium BEC in the IP trap described above. At $t = 0$ we switch on the \mathbf{B}_m field, using B_0 to tune the measured trap frequency to $\Omega/2\pi = 394\ \text{Hz}$. As the trap minimum shifts down by $\delta y = 0.40\ \mu\text{m}$, the initial position of the cloud is slightly above the trap center. The $1/e$ -switching time of the \mathbf{B}_m field was measured to be $\tau \approx 3\ \mu\text{s}$, which corresponds to $\omega\tau \approx 0.08$. When changed, the B_0 field settles to a new value after a damped oscillation with a frequency of $650\ \text{Hz}$ and a damping time τ' of $0.56\ \text{ms}$. This corresponds to $\Omega\tau' \approx 0.2$. The velocity $\dot{\boldsymbol{\rho}}$ of the BEC in the radial plane at the time of release is determined by time-of-flight absorption imaging along the z axis. For the chosen flight time of $23\ \text{ms}$, a speed of $1\ \text{mm/s}$ corresponds to a displacement of $23\ \mu\text{m}$ with respect to a cloud released from the same position at zero velocity. A cloud released at rest at time t_{rel} is imaged at position $\mathbf{R}_0 = \boldsymbol{\rho}(t_{\text{rel}}) + \frac{1}{2}\ddot{\boldsymbol{\rho}}_g \Delta t_{\text{TOF}}^2$, where $\ddot{\boldsymbol{\rho}}_g$ is the gravitational acceleration. For a finite release velocity $\dot{\boldsymbol{\rho}}(t_{\text{rel}})$ the cloud will be imaged at $\mathbf{R} = \dot{\boldsymbol{\rho}}(t_{\text{rel}})\Delta t_{\text{TOF}} + \mathbf{R}_0$.

In practice we may neglect the small variation in the release position due to the macromotion, approximating $\boldsymbol{\rho}(t_{\text{rel}}) \simeq \boldsymbol{\rho}(0)$, because this variation is smaller than the shot-to-shot reproducibility of the cloud position. From the model analysis of Section 5.2.2 the variation in release position due to the macromotion is estimated to be $\delta\boldsymbol{\rho}(t_{\text{rel}}) \lesssim (\omega/\Omega)\rho_0 \approx 4\ \mu\text{m}$. The centroid of the image of the expanded cloud is determined using a simple Gaussian fitting procedure and has a shot-to-shot reproducibility of $\sim 8\ \mu\text{m}$, small as compared to the $140\ \mu\text{m}$ radius of the expanded cloud. No improvement in shot-to-shot reproducibility was found by changing to a higher magnification. Since our measurements depend only on the position of the cloud center they are insensitive to fluctuations in atom number or density. To reconstruct the motion of the condensate in the trap we image the cloud at $t = t_i$, where t_i is the holding time in the TOP. We obtain the release velocity by measuring the x and y components of the cloud centroid (R_x, R_y). A typical set of data is shown in Fig. 5.5. The micromotion is recognized as the rapid modulation on the slow macromotion. As the frequency of the micromotion is accurately known we avoid aliasing by sampling the motion in steps of $0.025\ \text{ms}$, much shorter than the micromotion period. If we wish to look only at the macromotion in a stroboscopic manner, we can

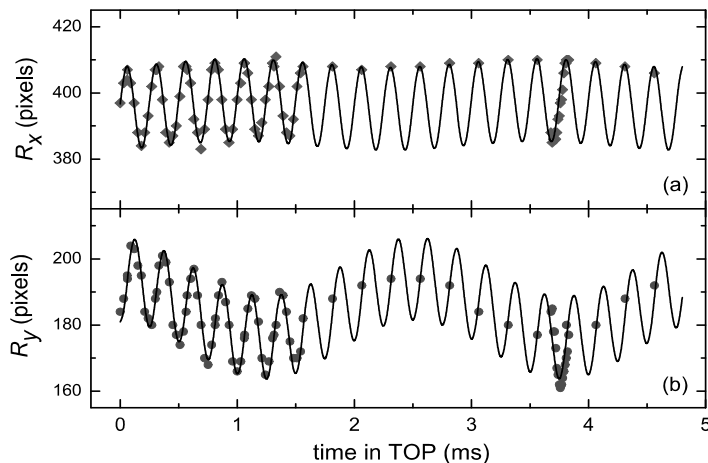


Figure 5.5: The centroid position after 23 ms TOF plotted in camera pixel units against holding time in the TOP trap: upper dataset: R_x ; lower dataset: R_y . The solid lines represent the fit of Eqs. (5.17) and (5.18) to the data. Note that by a stroboscopic measurement at 0.25 ms intervals the micromotion is eliminated. Each point represents a single measurement.

sample precisely at the micromotion period of 0.25 ms, with best results obtained when sampling on the crests of the micromotion. Fitting the expressions

$$R_x = -v_0 \Delta t_{\text{TOF}} \sin(\omega t + \phi) - V_{0,x} \Delta t_{\text{TOF}} \sin(\Omega t + \varphi_x) + R_{0,x} \quad (5.17)$$

$$R_y = v_0 \Delta t_{\text{TOF}} \cos(\omega t + \phi) + V_{0,y} \Delta t_{\text{TOF}} \cos(\Omega t + \varphi_y) + R_{0,y} \quad (5.18)$$

to the data, using the TOP frequency ω and Δt_{TOF} as known parameters, we obtain the amplitudes v_0 , $V_{0,x}$, $V_{0,y}$ as well as the macromotion frequency Ω and the phases ϕ , φ_x , φ_y . Note that the fit also yields the reference position $\mathbf{R}_0 = \{R_{0,x}, R_{0,y}\}$ but this information is superfluous for the reconstruction of the in-trap motion. Once these quantities are determined the motion of the condensate in the TOP trap is readily reconstructed with Eq. (5.12).

To investigate the effect of phase jumps, we implement the approach described in Section 5.2.4. First we determine for given ω and Δt_{TOF} all parameters to reconstruct the motion with the method just described. This enables us to determine the time intervals $t_n - \Delta t < t < t_n + \Delta t$, where the cloud returns close to the origin, and choose within this interval the time t_a , where the total velocity $\dot{\rho}(t_a)$ has magnitude

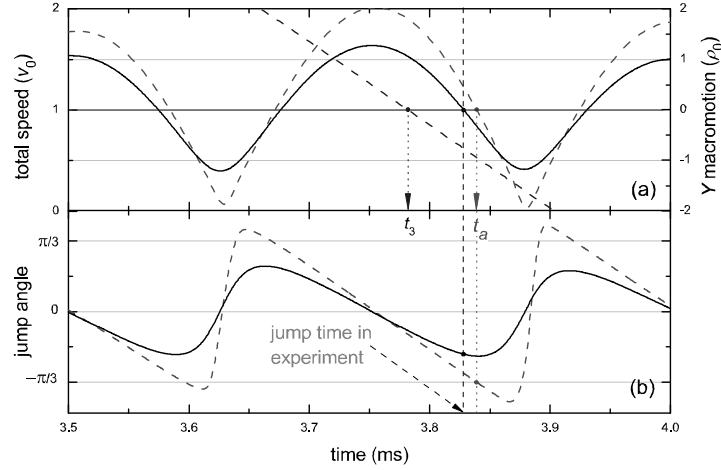


Figure 5.6: Illustration of how to choose the optimal phase jump and its timing. In both panels: solid curve - experimental conditions; dashed curve - analytical model of Section 5.2.4 for the case of instant switching - no gravity. (a) The total speed of the cloud in units of the micromotion speed v_0 (optimal phase jump time t_a corresponds to $\dot{\rho}(t_a) = v_0$); the dashed line (scale on right) shows the Y component of the macromotion position crossing zero at $t = t_3$ (stationary micromotion can be achieved by adjusting ω such that $t_3 = t_a$); (b) The optimal phase jump as a function of jump time as calculated by Eq. (5.16).

v_0 as shown in Fig. 5.6a. The red dashed lines correspond to the analytical model of Section 5.2.4 for the case of instant switching - no gravity (the case of Fig. 5.4a). The black solid lines correspond to the calculation including all relevant experimental constraints. The phase jump $\Delta\phi_m$ that sets $\hat{\rho}_m$ perpendicular to $\dot{\rho}(t_a)$ is given by Eq. (5.16). This optimal phase jump $\Delta\phi_m$ is plotted versus t_a in a time interval around $t_3 = 3\pi/\Omega$ in Fig. 5.6b. For the case of instant switching - no gravity the optimum phase jump is seen to be $\Delta\phi_m = -\pi/3$. At the chosen time t_a we vary the phase jump $\Delta\phi_m$ about the value suggested by Eq. (5.16) in search for optimal quenching. To reconstruct the residual macromotion, we hold the cloud for a variable additional time t_b , before TOF imaging at time $t = t_a + t_b$.

5.4 Analytic Model

For arbitrary ϕ_m the position $\boldsymbol{\rho}' = \{x', y'\}$ with respect to a coordinate system rotated over an angle ϕ_m is

$$x'(t) = -\rho_0 \cos \omega t + X'_0 \cos(\Omega t + \varphi'_x) \quad (5.19)$$

$$y'(t) = -\rho_0 \sin \omega t + Y'_0 \sin(\Omega t + \varphi'_y), \quad (5.20)$$

where X'_0, Y'_0 are the amplitudes and φ'_x, φ'_y the phases with respect to the rotated axes. Taking the time derivative and using the initial conditions $\boldsymbol{\rho}', \dot{\boldsymbol{\rho}}' = 0$ at $t = 0$, yields: $\varphi'_x = \varphi'_y = 0, X'_0 = \rho_0, Y'_0 = (\omega/\Omega)\rho_0$. This corresponds to an ellipse with its major axis oriented perpendicular to the instantaneous direction $\hat{\boldsymbol{\rho}}'_m \equiv \hat{\boldsymbol{\rho}}_m$ of the \mathbf{B}_m field at $t = 0$.

For exponential switch-on of the \mathbf{B}_m field with $1/e$ time τ_0 , we have for the acceleration in the 'primed' coordinate system

$$\begin{aligned} \ddot{x}'(t) = \omega^2(1 - \exp[-t/\tau_0])\rho_0 \cos \omega t - \\ - \Omega^2 X'_0 \cos(\Omega t + \varphi'_x) \end{aligned} \quad (5.21)$$

$$\begin{aligned} \ddot{y}'(t) = \omega^2(1 - \exp[-t/\tau_0])\rho_0 \sin \omega t - \\ - \Omega^2 Y'_0 \sin(\Omega t + \varphi'_y), \end{aligned} \quad (5.22)$$

where, during switch-on, $X'_0, Y'_0, \varphi'_x, \varphi'_y$ and Ω are functions of time. Since $\Omega \ll \omega$ we may approximate, for $\omega t \ll 1$,

$$\ddot{x}'(t) \simeq \omega^2(1 - \exp[-t/\tau_0])\rho_0 \cos \omega t \gg \ddot{y}'(t). \quad (5.23)$$

This shows that the switch-on profile mainly affects the acceleration in the x' direction because this is the initial direction of acceleration. By the time $\sin \omega t$ is sufficiently large to make \ddot{y}' non-negligible, the switch-on transient is already finished. For $\omega t \ll 1$, the velocity in the x' direction is given by $\dot{x}'(t) \simeq \omega^2(t - \tau + \tau \exp[-t/\tau])\rho_0$. This expression suggests to approximate the switch-on profile by a step function at $t = \tau_0 \simeq \tau$ and to treat $X'_0, Y'_0, \varphi'_x, \varphi'_y$ as constants for $t \geq \tau_0$. This 'delayed sudden-step approximation' is equivalent to imposing the boundary conditions $\boldsymbol{\rho}', \dot{\boldsymbol{\rho}}' = 0$ at $t = \tau_0$. In this approximation we obtain for the phases and amplitudes $\varphi'_x = \tan^{-1}[\omega^2 \tau_0 / \Omega]$, $\varphi'_y = 0, X'_0 = \rho_0(1 + \omega^4 \tau_0^2 / \Omega^2)^{1/2}, Y'_0 = (\omega/\Omega)\rho_0$ for $t \geq \tau_0$. The phase development $\omega \tau_0$ due to rotation of the \mathbf{B}_m field during switch-on will appear as a rotation of the major and minor axes of the macromotion with respect to the primed coordinate system defined by $t = 0$. The optimal value for τ_0 can be determined by comparing the predictions of the analytical model with the results of a numerical calculation (see Section 5.2.3).

In the presence of gravity, the above analysis remains valid as long as the radial frequency Ω does not change substantially during switch-on of the \mathbf{B}_m field; in principle Ω can be kept constant by simultaneously switching B_0 and B_m in such a

way that the quantity $\bar{B}_0/(1 + \frac{1}{2}B_m^2/\bar{B}_0^2)$ equals the value of B_0 before the \mathbf{B}_m field was switched on. In case of a small and fast change in Ω the above model can be adapted by changing the initial conditions to $\boldsymbol{\rho} = \{0, \delta y\}$, $\dot{\boldsymbol{\rho}} = 0$ at $t = \tau_0$, where $\delta y = \Delta y_{\text{TOP}} - \Delta y_{\text{IP}}$ is the difference in gravitational sag. Using the adapted boundary conditions we obtain in the limits $(g\alpha/\bar{B}_0)^{1/2} \ll \Omega \ll \omega$ and $\omega\tau_0 \ll 1$ for the amplitudes and phases of the macromotion

$$X_0 = \rho_0[1 + (\omega^2/\Omega^2 - 1) \sin^2(\omega\tau_0 + \phi_m)]^{1/2} \quad (5.24)$$

$$Y_0 = \rho_0[1 + (\omega^2/\Omega^2 - 1) \cos^2(\omega\tau_0 + \phi_m) + \delta y^2/\rho_0^2 + 2(\delta y/\rho_0) \sin(\omega\tau_0 + \phi_m)]^{1/2} \quad (5.25)$$

$$\varphi_x = -\Omega\tau_0 + \tan^{-1}[(\omega/\Omega) \tan(\omega\tau_0 + \phi_m)] + n\pi \quad (5.26)$$

$$\varphi_y = -\Omega\tau_0 + \tan^{-1}[(\Omega/\omega)\{\tan(\omega\tau_0 + \phi_m) + (\delta y/\rho_0)/\cos(\omega\tau_0 + \phi_m)\}] + n\pi. \quad (5.27)$$

where $n = 0$ for $|\omega\tau_0 + \phi_m| \leq \pi/2$, $n = 1$ for $|\omega\tau_0 + \phi_m| > \pi/2$. For $\phi_m = 0$, these equations coincide with the equations for X'_0 , Y'_0 , φ'_x and φ'_y in the primed coordinate system. Analyzing the limit $\omega\tau_0 \rightarrow 0$ for the case $\delta y \simeq \rho_0$ (typical for our experimental conditions) we find $X_0 \simeq \rho_0$ and $Y_0 \simeq (\omega/\Omega)\rho_0$ for $\phi_m = 0$ and $X_0 \simeq (\omega/\Omega)\rho_0$ and $Y_0 \simeq 2\rho_0$ for $\phi_m = \pi/2$. Thus, we deduce that gravity can have a substantial influence on the amplitude of the macromotion along its minor axis but not on the amplitude along the major axis. For known values of X_0 , Y_0 , φ_x and φ_y the angle of rotation ϑ to align the coordinate system along the major and minor axis is given by Eq. (5.15). For $\Omega\tau_0 \ll \omega\tau_0 \ll 1$ and in the absence of gravity ($\delta y = 0$) the delayed sudden-step gives rise to a small rotation $\Delta\varphi \simeq \omega\tau_0$, independent of ϕ_m . For $\delta y \simeq \rho_0$ gravity gives rise to an additional contribution to this rotation, which is minimal for $\phi_m = \pi/2$, where the macromotion is launched perpendicular to the gravity direction and Eq. (5.15) can be approximated by $\varphi \simeq \omega\tau_0[1 + (1 + \delta y/\rho_0)(\Omega/\omega)^2]$. The contribution is maximal for $\phi_m = 0$, where Eq. (5.15) can be approximated by $\varphi \simeq \omega\tau_0 - (\Omega/\omega)^2(\delta y/\rho_0)^2(1 + \omega\tau_0)$.

Insight in the dependence of X_0 and Y_0 on the settling behavior of B_0 can be obtained from Eq. (5.23), which shows that the initial acceleration and, hence, the launch speed scales with the initial value of ρ_0 . Therefore, most of the settling behavior is captured by using the *initial* value of ρ_0 in Eqs. (5.24) and (5.25). The 5% change in Ω requires a further refinement of the model. This cannot be implemented without sacrificing the simplicity of the model and is not pursued here.

5.5 Results and discussion

In this section we show the results obtained with the experimental procedure described in the previous section. We measured the macromotion induced by switching on the \mathbf{B}_m field for three values of the initial TOP phase, $\phi_m = 0, \pi/4, \pi/2$. For $\phi_m = 0$ part of the raw data are shown in Fig. 5.5. In Fig. 5.7 we show the measured

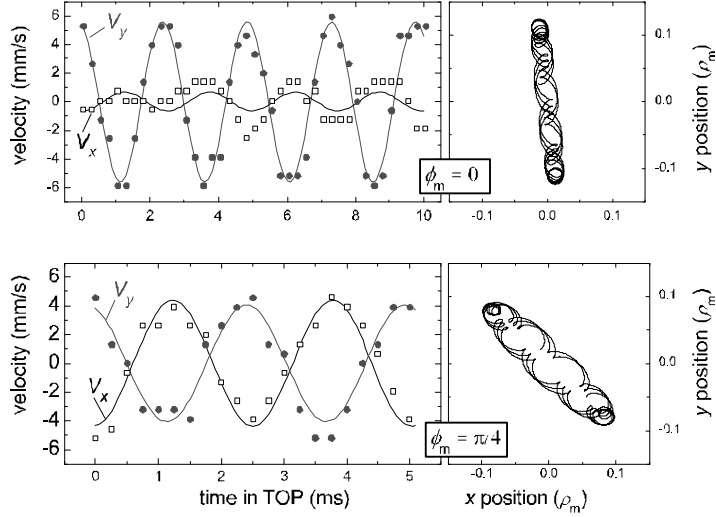


Figure 5.7: The panels on the left show the macromotion velocities (taken with the stroboscopic method) of the cloud centroid x - and y - versus time for $\phi_m = 0$ and $\pi/4$. The solid curves are fits of Eqs. (5.17) and (5.18) to the data. The panels on the right represent the reconstructed trajectories in parametric form (in units of the TOP radius $\rho_m = 19.5 \mu\text{m}$). The difference in aspect ratio is caused by the gravity shift.

velocity of the macromotion obtained with the stroboscopic method. The upper and lower panels correspond to $\phi_m = 0$ and $\pi/4$ respectively. The data for $\phi_m = \pi/2$ are not shown but are similar to those for $\phi = 0$ but with the roles of x and y interchanged.

The solid lines in the left panels of Fig. 5.7 are obtained by fitting Eqs. (5.17) and (5.18) to the full data including micromotion and provide the input for calculating the amplitudes. Using the known TOP frequency $\omega/2\pi = 4 \text{ kHz}$ and flight time $\Delta t_{\text{TOF}} = 23 \text{ ms}$, the fit yields for the velocity amplitudes, phases, and frequency: $v_0 = 7.6(2) \text{ mm/s}$, $V_{0,x} = 0.7(2) \text{ mm/s}$, $V_{0,y} = 5.6(2) \text{ mm/s}$, $\phi = 1.00(1)\pi$, $\varphi_x = 0.5(2)\pi$, $\varphi_y = 0.05(2)\pi$, and $\Omega/2\pi = 394(4) \text{ Hz}$. The corresponding in-trap amplitudes are $\rho_0 \equiv v_0/\omega = 0.30(1) \mu\text{m}$, $X_0 \equiv V_{0,x}/\Omega = 0.28(7) \mu\text{m}$, and $Y_0 \equiv V_{0,y}/\Omega = 2.3(1) \mu\text{m}$.

The right panels in Fig. 5.7 are parametric plots of the trajectories obtained by reconstructing the motion in the trap from the velocity fits described above. The trajectories provide a useful way to see the effect of the initial phase of the applied \mathbf{B}_m field and in addition the upper panel can be directly compared with the theoretical prediction shown in Fig. 5.2. As expected, the orientation of the major axis of the macromotion is dependent on the initial phase ϕ_m of the \mathbf{B}_m field. The small tilt θ away from the direction perpendicular to $\hat{\rho}_m$ is clearly visible and consistent with

the calculations for a finite switch-on time and the presence of gravity. The value obtained for ρ_0 is slightly smaller than the value calculated with Eq. (5.10) but in view of experimental uncertainties certainly consistent with the value of α . The results for φ_x/π , φ_y/π , X_0/ρ_0 , Y_0/ρ_0 and the tilt angle θ obtained for $\phi_m = 0$ and $\pi/4$ are given in Table 5.2. For comparison, also the numerical results are included.

We now turn to the results of a quenching experiment. The time $t_a \simeq 3.83$ ms and magnitude $\Delta\phi_m = -0.22\pi$ of the phase jump have been chosen to meet the conditions necessary to quench the macromotion as introduced in Section 5.3.2 and illustrated in Fig. 5.6. In Fig. 5.8 we show velocity data taken with the stroboscopic method. For $t < 3.83$ ms the data coincide with those shown in the upper panel of Fig. 5.7 but the solid lines are not a fit but represent the macromotion velocity predicted by the numerical calculation on the basis of the experimental parameters. These velocity curves correspond to the macromotion part of the position plot Fig. 5.4b and have no adjustable parameters. Both experiment and theory show pronounced reduction in the amplitude of the macromotion. Although, the phases of the quenched motion cannot be determined convincingly with our signal to noise ratio, the agreement between theory and experiment is satisfactory.

In general a jump in the micromotion phase produces an abrupt change in macromotion phase and amplitude. For the case illustrated in Fig. 5.8 we obtain a reduction of more than a factor of 5 in the amplitude of oscillation in the y direction at the expense of only a slight increase of the amplitude in the x direction. As a result the macromotion is reduced to the size of the micromotion. The energy associated with the macromotion is consequently reduced by a factor of about 15, reducing it to a small fraction of the micromotion energy. This demonstrates that the initial sloshing motion of the cloud can be efficiently quenched by applying an appropriate phase jump angle. As pointed out in the last paragraph of Section 5.2.4 we expect that it should be possible to suppress the macromotion almost completely by adjusting the micromotion frequency such that $t_3 = t_a$.

Even a small variation in the phase jump magnitude or its timing can result in a substantial difference in quenching efficiency. This is illustrated in Fig. 5.9, where we

Table 5.2: Experimental results (exp) for macromotion induced by the switch-on of the TOP field for $\phi_m = 0, \pi/4$. The data are compared with the results of the numerical calculation of Section 5.2.3 (num). In all cases the tilt angle has been calculated with the aid of Eq. 5.15

	ϕ_m	θ/π	φ_x/π	φ_y/π	X_0/ρ_0	Y_0/ρ_0
exp	0	0.04(2)	0.5(2)	0.05(2)	0.9(2)	7.7(3)
num	0	0.016	0.20	0.06	0.82	6.5
exp	$\pi/4$	0.04(2)	0.49(2)	0.12(2)	6.6(4)	5.2(3)
num	$\pi/4$	0.013	0.47	0.04	4.95	4.55

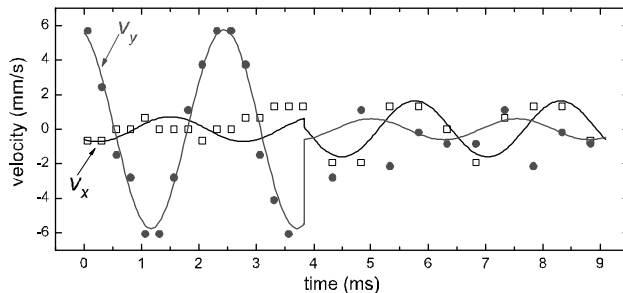


Figure 5.8: Measured and calculated velocity of the macromotion before and after a phase jump of $\Delta\phi_m = -0.22\pi$ at $t_a = 3.83$ ms for initial phase $\phi_m = 0$. The open squares (solid circles) correspond to the measured V_x (V_y) velocity component (for $t_a < 3.83$ ms the data coincide with those of Fig. 5.7). Each point represents a single measurement. The solid lines correspond to the numerical model without any adjustable parameter as described in the text.

plot the ratio of macro- and micromotion energy,

$$\frac{E_{macro}}{E_{micro}} = \frac{V_{0,x}^2 + V_{0,y}^2}{v_0^2}, \quad (5.28)$$

as the phase jump is varied in steps of 10 degrees, for $t_a = 1.32$ ms and 1.33 ms, where the position and velocity criteria are well satisfied. For most phase jumps $\Delta\phi_m$ the result is an *increase* in energy. The drawn lines are the predictions from the numerical model for the same conditions at $t_a = 1.31$ ms and $t_a = 1.32$ ms. The plot for $t_a = 1.32$ ms shows a deeper reduction than that for $t_a = 1.31$ ms, as well as a shifted optimal $\Delta\phi_m$. The common shift of ~ 0.01 ms between the data and the numerical results remains unexplained.

5.6 Summary and conclusion

We have shown that a cold atomic cloud initially at rest at the minimum of the effective potential of a TOP trap, acquires a macroscopic sloshing motion, in addition to near circular micromotion, when the TOP is suddenly switched on. The energy associated with this macromotion is of the same order as the energy of the micromotion and the amplitude of the former is larger than that of the latter by a factor $\sim \omega/\Omega$. We have theoretically described the phenomenon and the predictions compare well with our experimental results.

As the micromotion is shared in common mode by all trapped atoms, the associated energy does not affect the thermodynamics of the cloud in any way. In contrast, the macromotion energy is generally unwanted and potentially harmful. Fortunately,

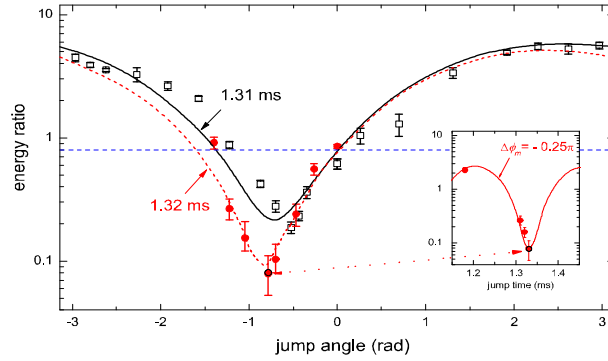


Figure 5.9: Ratio of macromotion energy over micromotion energy following a phase jump plotted against $\Delta\phi_m$ at 1.32 ms (open black squares) and 1.33 ms (red circles). Each data point is obtained from fits as described in the text. The horizontal blue dashed line shows the initial value of the energy before the phase jump. The solid black lines and dotted red are the numerical calculation for 1.31 ms and 1.32 ms respectively. The inset shows the dependence on jump time for fixed value of $\Delta\phi_m$.

as we have shown, it is possible to quench this macromotion almost completely and instantly, by applying a suitable and properly timed phase jump to the rotating magnetic field that defines the TOP. We have shown theoretically that this procedure works, even for the 2D case of the TOP, which is an extension of previous theory describing similar phenomena in 1D [42, 43]. We have presented a framework which allows a deterministic procedure for choosing the optimal parameters for the phase jump. Our experiments corroborate the theoretical model for the TOP in a quantitative manner.

The macromotion induced by the switch-on and the subsequent possibility to alter this motion by phase jumps have several consequences, some of which we now briefly mention. For example, the sloshing motion may affect the time of flight imaging once the fields have been switched off. When comparing TOF-images for different holding times it is in general not sufficient to synchronize the release time to the micromotion period. The position after TOF can be easily polluted by the non-zero macromotion, which evolves asynchronously with the micromotion. The time scales in this experiment are on the order of a few macromotion periods. The physics of interest of the cloud is usually seen on much longer time scales of hundreds of such periods. On these longer time scales, the presence of even small anharmonicities can lead to the conversion of macromotion energy into heat. The macromotion can be of order of the chemical potential which can have consequences for the stability of the condensate.

The possibility to excite or quench macromotion by phase jumps of the rotating field is a valuable feature of the TOP trap that has received little attention in the literature. Our work shows that this feature is well understood and can be applied in a well-controlled manner. We have primarily focussed on quenching with a single phase jump. However, the reverse effect in which the macromotion is excited may prove equally useful in some experiments. Also the consequences for multiple phase-jump applications deserve attention in this respect. We established numerically that it should be possible to excite or deexcite large macromotion with a series of π phase jumps at intervals of the macromotion half-period. At each of these phase jumps, either component of the macromotion velocity can be increased or decreased by $\sim 2v_0$. Being outside the primary focus of this thesis, we do not further elaborate on this interesting topic.

Appendix A

Quadrupole field with permanent magnets

A 2D quadrupole field can be produced by a simple geometry of just one pair of permanent magnets [50]. In this section the design of such a quadrupole field will be discussed. First we consider the magnetic field at position $\mathbf{R} = (R, \theta, \varphi)$ relative to the position $\mathbf{r}_0 = (x_0, y_0, z_0)$ of a single magnetic point dipole \mathbf{m} of dipole moment $m = |\mathbf{m}|$ pointing parallel to the y axis of a Cartesian plane as shown in Fig. A.1. The field $\mathbf{B}(\mathbf{r})$ at position \mathbf{r} can be expressed as

$$B_r = \mu_0 \frac{2m \cos \theta}{4\pi R^3}; \quad B_\theta = \mu_0 \frac{m \sin \theta}{4\pi R^3}; \quad B_\phi = 0, \quad (\text{A.1})$$

where $\cos \theta = (y - y_0) / r$, $\sin \theta = \sqrt{1 - \cos^2 \theta}$ with $0 \leq \theta \leq \pi$ and

$$R = |\mathbf{r} - \mathbf{r}_0| = \sqrt{(x - x_0)^2 + (y - y_0)^2 + (z - z_0)^2}. \quad (\text{A.2})$$

Here x, y and z are the cartesian components of \mathbf{r} . The Cartesian components of the field are given by

$$B_x(R, \theta, \varphi) = B_r \sin \theta \cos \phi + B_\theta \cos \theta \cos \phi \quad (\text{A.3a})$$

$$B_y(R, \theta, \varphi) = B_r \cos \theta - B_\theta \sin \theta \quad (\text{A.3b})$$

$$B_z(R, \theta, \varphi) = B_r \sin \theta \sin \phi + B_\theta \cos \theta \sin \phi, \quad (\text{A.3c})$$

where $\cos \phi = (x - x_0) / \rho$ and $\sin \phi = (z - z_0) / \rho$, with $\rho = R \sin \theta$.

Substituting Eq. (A.1) into (A.3) the field components at position $\mathbf{r} = (x, y, z)$ created by a *single point dipole* become

$$B_x(x, y, z) = \frac{3\mu_0 m}{4\pi R^5} (x - x_0) (y - y_0) \quad (\text{A.4a})$$

$$B_y(x, y, z) = \frac{3\mu_0 m}{4\pi R^5} [(y - y_0)^2 - r^2 / 3] \quad (\text{A.4b})$$

$$B_z(x, y, z) = \frac{3\mu_0 m}{4\pi R^5} (z - z_0) (y - y_0). \quad (\text{A.4c})$$

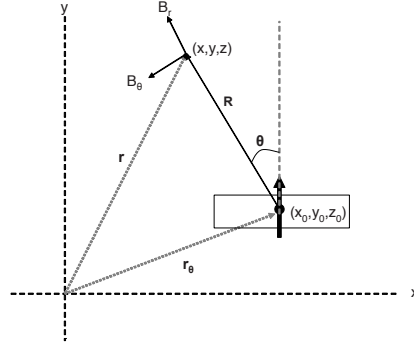


Figure A.1: A single dipole m orientated parallel to the y -axis and the polar components B_r and B_θ of the magnetic field at an arbitrary point (x, y, z) .

Let us now turn to the field created by *two identical point dipoles* \mathbf{m}_1 and \mathbf{m}_2 positioned on the x axis at $x_1 = x_0$ and $x_2 = -x_0$, with \mathbf{m}_1 pointing in the positive y direction and \mathbf{m}_2 pointing in the negative y direction as shown in Fig. 2.6. We shall show that, close to the origin, these dipoles give rise to a quadrupole field in the x - y plane. The distances d_1 and d_2 to dipoles \mathbf{m}_1 and \mathbf{m}_2 can be expressed as $d_1^2 = (x - x_0)^2 + y^2 + z^2$ and $d_2^2 = (x + x_0)^2 + y^2 + z^2$, respectively. Substituting $y^2 = r^2 - x^2 - z^2$ and assuming $|z| \ll r \ll x_0$ yields

$$B_x = B_{x_1} + B_{x_2} \simeq \frac{3\mu_0 m}{4\pi} \left(\frac{1}{d_1^5} + \frac{1}{d_2^5} \right) x_0 y \simeq \frac{3\mu_0 m}{4\pi} 2y/x_0^4 \quad (\text{A.5a})$$

$$B_y = B_{y_1} + B_{y_2} \simeq \frac{3\mu_0 m}{4\pi} \left(\frac{1}{3d_1^3} - \frac{1}{3d_2^3} \right) \simeq \frac{3\mu_0 m}{4\pi} 2x/x_0^4 \quad (\text{A.5b})$$

$$B_z = B_{z_1} + B_{z_2} \simeq \frac{3\mu_0 m}{4\pi} \left(\frac{1}{d_1^5} + \frac{1}{d_2^5} \right) yz \simeq \frac{3\mu_0 m}{4\pi} 10xyz/x_0^6 \quad (\text{A.5c})$$

Note that (close to the origin) the field has indeed the symmetry of the 2D quadrupole in the x - y plane, with the modulus of the field increasing linearly with the distance to the z axis.

Next we replace the point dipoles by homogeneously magnetized bar magnets of Neodymium Iron Boron. The magnetization \mathbf{M} inside a bar is the magnetic moment per unit volume. As the bars are magnetized to saturation the magnetization is constant over the volume of the bar. Hence, the magnetic field is obtained by replacing m by M and integrating over the volume. Using Eq.(A.4) for a bar magnet of volume $\Delta x \Delta y \Delta z$ at position $\mathbf{r}_n = (x_n, y_n, z_n)$ with magnetization \mathbf{M} pointing in the positive y direction, the field components at position $\mathbf{r} = (x, y, z)$ created by a *single bar* are

given by

$$B_x(\mathbf{r}, \mathbf{r}_n) = \frac{3\mu_0}{4\pi} M \int_{\mathbf{r}_{\min}(\mathbf{r}_n)}^{\mathbf{r}_{\max}(\mathbf{r}_n)} dx' dy' dz' \frac{(x-x')(y-y')}{r^5} \quad (\text{A.6a})$$

$$B_y(\mathbf{r}, \mathbf{r}_n) = \frac{3\mu_0}{4\pi} M \int_{\mathbf{r}_{\min}(\mathbf{r}_n)}^{\mathbf{r}_{\max}(\mathbf{r}_n)} dx' dy' dz' \frac{[(y-y')^2 - r^2/3]}{r^5} \quad (\text{A.6b})$$

$$B_z(\mathbf{r}, \mathbf{r}_n) = \frac{3\mu_0}{4\pi} M \int_{\mathbf{r}_{\min}(\mathbf{r}_n)}^{\mathbf{r}_{\max}(\mathbf{r}_n)} dx' dy' dz' \frac{(z-z')(y-y')}{r^5}. \quad (\text{A.6c})$$

where $\mathbf{r}_{\min} = (x_{\min}, y_{\min}, z_{\min})$ and $\mathbf{r}_{\max} = (x_{\max}, y_{\max}, z_{\max})$, with $x_{\min} = x_n - \Delta x/2$ and $x_{\max} = x_n + \Delta x/2$ and analogous expressions for y_{\min} , y_{\max} , z_{\min} and z_{\max} . Evaluating the integrals the field components take the form

$$B_x(\mathbf{r}, \mathbf{r}_n) = -\frac{\mu_0}{4\pi} M \sum_{i,j,k=0}^1 (-1)^{i+j+k} \operatorname{arcsinh} \left[\frac{z - z_{nk}}{\sqrt{(x - x_{ni})^2 + (y - y_{nj})^2}} \right] \quad (\text{A.7a})$$

$$B_y(\mathbf{r}, \mathbf{r}_n) = +\frac{\mu_0}{4\pi} M \sum_{i,j,k=0}^1 (-1)^{i+j+k} \arctan \left[\frac{(x - x_{ni})(z - z_{nk}) / (y - y_{nj})}{\sqrt{(x - x_{ni})^2 + (y - y_{nj})^2 + (z - z_{nk})^2}} \right] \quad (\text{A.7b})$$

$$B_z(\mathbf{r}, \mathbf{r}_n) = -\frac{\mu_0}{4\pi} M \sum_{i,j,k=0}^1 (-1)^{i+j+k} \operatorname{arcsinh} \left[\frac{x - x_{nk}}{\sqrt{(z - z_{ni})^2 + (y - y_{nj})^2}} \right], \quad (\text{A.7c})$$

where $\mathbf{r}_{n0} \equiv \mathbf{r}_{\min}(\mathbf{r}_n)$ and $\mathbf{r}_{n1} \equiv \mathbf{r}_{\max}(\mathbf{r}_n)$.

Bibliography

- [1] A. Einstein, *Sitzungsber. Preuss. Akad. Wiss.*, 3:18 (1925).
- [2] S. Bose, *Zeitschrift für Physik*, 26, 178 (1924).
- [3] C. J. Pethick and H. Smith, *Bose-Einstein Condensation in Dilute Gases*. Cambridge University Press (2002).
- [4] L. Pitaevski and S. Stringari, *Bose-Einstein Condensation*. Oxford University Press (2003).
- [5] P. Kapitza, *Nature*, 141, 3558 (1938).
- [6] J.F. Allen, A.D. Misener, *Nature* 141(3558), 75 (1938).
- [7] W.F. Vinen, *Proc. R. Soc. A* 260(1301), 218 (1961).
- [8] R.J. Donnelly, *Quantized Vortices in Helium II*, Cambridge University Press, (1991).
- [9] I.F. Silvera and J.T.M. Walraven, in *Progr. Low Temp Phys.*, (D. Brewer, ed) Vol. X, 139-370 (1986).
- [10] A.L. Migdall, J.V. Prodan, W.D. Phillips, T.H. Bergeman and H.J. Metcalf, *Phys. Rev. Lett.* 54, 2596 (1985).
- [11] H. Metcalf and P. van der Straten, *Laser Cooling and Trapping*, Springer, (1999).
- [12] H.F. Hess, G.P. Kochanski, J.M. Doyle, N. Masuhara, D. Kleppner, T.J. Greytak, *Phys. Rev. Lett.* 59, 672 (1987).
- [13] O.J. Luiten, M.W. Reynolds, J.T.M. Walraven, *Phys. Rev. A* 53, 381 (1995).
- [14] M. H. Anderson, J. R. Ensher, M. R. Matthews, C. E. Wieman, E. A. Cornell, *Science* 269, 198 (1995).
- [15] K. B. Davis, M. O. Mewes, M. R. Andrews, N. J. van Druten, D. S. Durfee, D. M. Kurn, and W. Ketterle, *Phys. Rev. Lett.* 75, 3969 (1995).

- [16] W. Petrich, M.H. Anderson, J.R. Ensher, and E.A. Cornell, *Phys. Rev. Lett.* 74, 3352 (1995).
- [17] D.S. Jin, J.R. Ensher, M.R. Matthews, C.E. Wieman, E.A. Cornell, *Phys. Rev. Lett.* 77, 420 (1996).
- [18] D.S. Hall, J.R. Ensher, D.S. Jin, M.R. Matthews, C.E. Wieman, E.A. Cornell, *Proc. SPIE*, 98, 3270 (1998).
- [19] D.J. Han, R.H. Wynar, Ph. Courteille, and D.J. Heinzen *Phys. Rev. A* 57, R4114 (1998).
- [20] B.P. Anderson and M.A. Kasevich *Phys. Rev. A* 59, R938 (1999).
- [21] O.M. Maragò, S.A. Hopkins, J. Arlt, E. Hodby, G. Hechenblaikner, and C.J. Foot, *Phys. Rev. Lett.* 84, 2056 (2000).
- [22] J.D. Luca, R. Napolitano, V.S. Bagnato, *Phys. Rev. A*, 55, 1597 (1997)
- [23] V.E. Shapiro, *Phys. Rev. A*, 54, 1018 (1996).
- [24] M. Edwards, R.J. Dodd, C.W. Clark, P.A. Ruprecht, and K. Burnett, *Phys. Rev. A* 53, R1950 (1996).
- [25] V. I. Yukalov, *Phys. Rev. A*, 56, 5004 (1997).
- [26] V.G. Minogin, J.A. Richmond, and G.I. Opat, *Phys. Rev. A* 58, 3138 (1998).
- [27] A.B. Kuklov, N. Chencinski, A.M. Levine, W.M. Schreiber, and J.L. Birman, *Phys. Rev. A* 55, 488 (1997).
- [28] M.R. Matthews, B.P. Anderson, P.C. Haljan, D.S. Hall, C.E. Wieman, E.A. Cornell, *Phys. Rev. Lett.* 83(13), 2498 (1999).
- [29] P. C. Haljan, I. Coddington, P. Engels, and E. A. Cornell *Phys. Rev. Lett.* 87, 210403 (2001).
- [30] E. Hodby, G. Hechenblaikner, S. A. Hopkins, O. M. Maragò, and C. J. Foot *Phys. Rev. Lett.* 88, 010405 (2001).
- [31] M. Kozuma, L. Deng, E.W. Hagley, J. Wen, R. Lutwak, K. Helmerson, S.L. Rolston, and W.D. Phillips, *Phys. Rev. Lett.* 82, 871 (1999).
- [32] J.H. Müller, O. Morsch, D. Ciampini, M. Anderlini, R. Mannella, and E. Arimondo *Phys. Rev. Lett.* 85, 4454 (2000).
- [33] D. R. Scherer, C. N. Weiler, T. W. Neely, and B. P. Anderson *Phys. Rev. Lett.* 98, 110402 (2007).

- [34] S.R. Muniz, D.S. Naik, and C. Raman, *Phys. Rev. A* **73**, 041605(R) (2006).
- [35] T.G. Tiecke, M. Kemmann, Ch. Buggle, I. Schwarchuck, W. von Klitzing and J.T.M. Walraven, *J. Opt. B*, **5**, S119 (2003).
- [36] N.R. Thomas, N. Kjærgaard, P.S. Julienne, and A.C. Wilson, *Phys. Rev. Lett.* **93**, 173201 (2004).
- [37] Ch. Buggle, J. Leonard, W. von Klitzing and J.T.M. Walraven, *Phys. Rev. Lett.* **93** 173202 (2004).
- [38] K. Dieckmann, Ph.D. thesis, University of Amsterdam (2001).
- [39] I. Shvarchuck, Ph.D. thesis, University of Amsterdam (2003).
- [40] K.J. Challis, R.J. Ballagh and C.W. Gardiner, *Phys. Rev. A* **70**, 053605 (2004).
- [41] R. Franzosi, B. Zambon, and E. Arimondo *Phys. Rev. A* **70**, 053603 (2004).
- [42] A. Ridinger and N. Davidson, *Phys. Rev. A* **76**, 013421 (2007).
- [43] A. Ridinger and C. Weiss, *Phys. Rev. A* **79**, 013414 (2009).
- [44] Ch. Buggle, Ph.D. thesis, University of Amsterdam (2004).
- [45] K. Dieckmann, R.C. Spreeuw, M. Weidemuller, J.T.M. Walraven, *Phys. Rev. A* **58**, 3891, (1998).
- [46] A. Roth, *Vacuum Technology*, chapter 4, page 158. Elsevier Science Publishers, (1990).
- [47] V. Ivanov, Ph.D. thesis, University of Amsterdam (2007).
- [48] S. Aubin, M. H. T. Extavour, S. Myrskog, L. J. LeBlanc, J. Esteve, S. Singh, P. Scrutton, D. McKay, R. McKenzie, I. D. Leroux, A. Stummer, and J. H. Thywissen, *J. Low Temp. Phys.* **140**, 377 (2005).
- [49] T. G. Tiecke, Ph.D. thesis, University of Amsterdam (2009).
- [50] M. Koot, Report, University of Amsterdam (2007).
- [51] T. G. Tiecke, S. D. Gensemer, A. Ludewig and J.T.M. Walraven, *Phys. Rev. A* **80**, 013409 (2009)
- [52] T. G. Tiecke, MSc. thesis, University of Amsterdam (2009).
- [53] M. D. Levenson and N. Bloembergen, *Phys. Rev. Lett.* **32**, 645 (1974).
- [54] F. Biraben, B. Cagnac and G. Grynberg, *Phys. Rev. Lett.* **32**, 643(1974).

- [55] S. Kraft, A. Deninger, C. Truck, J. Fortagh, F. Lison, and C. Zimmermann, *Laser Phys. Lett.* 1–6 (2004).
- [56] W. Ketterle, D.S. Durfee and D.M. Stamper-Kurn, in *Proc. Int. School Phys. Enrico Fermi course CXL*, M. Inguscio, S. Stringari, C. Wieman (Eds.), IOS Press, Amsterdam (1999).
- [57] T. Rom, Th. Best, D. van Oosten, U. Schneider, S. Folling, B. Parades, I. Bloch, *Nature*, 444, 733 (2006).
- [58] S. Whitlock, C.F. Ockeloen, and R.J.C. Spreeuw, *Phys. Rev. Lett.*, 104, 120402 (2010).
- [59] R. Wang, M. Liu, F. Minardi, M.Kasevich, *Phys. Rev. A* 75, 013610 (2007)
- [60] P.O. Fedichev, M.W. Reynolds, and G.V. Shlyapnikov, *Phys. Rev. Lett.* 77(14), 2921 (1996).
- [61] J. Soding, D. Guery-Odelin, P. Desbiolles, F. Chevy, H. Inamori, J. Dalibard, *Appl. Phys. B* 69, 257 (1999).
- [62] E.A. Burt, R.W. Ghrist, C.J. Myatt, M.J. Holland, E.A. Cornell, C.E. Wiemann, *Phys. Rev. Lett.* 79(14), 337 (1997).
- [63] J.R. Enscher, Ph.D thesis, University of Colorado (1998).
- [64] L. Onsager, *Suppl. Nuovo cimento* 2, 249 (1949).
- [65] R. Feynman, *Progress in Low-Temperature Physics*, Vol. 1, Chap. II, p.36 (1955).
- [66] E. Lundh, C.J. Pethick, H. Smith, *Phys. Rev. A* 58, 4816 (1998).
- [67] B.P. Anderson, P.C. Haljan, C.E. Wieman, E.A. Cornell, *Phys. Rev. Lett.* 85(14), 2857 (2000).
- [68] B.P. Anderson, P.C. Haljan, C.A. Regal, D.L. Feder, L.A. Collins, C.W. Clark, E.A. Cornell, *Phys. Rev. Lett.* 86(14), 2926 (2001).
- [69] K.W. Madison, F. Chevy, W. Wohlleben, J. Dalibard, *Phys. Rev. Lett.* 84(5), 806 (2000).
- [70] K.W. Madison, F. Chevy, V. Bretin, J. Dalibard, *Phys. Rev. Lett.* 86(20), 4443 (2001).
- [71] P. Rosenbusch, D.S. Petrov, S. Sinha, F. Chevy, V. Bretin, Y. Castin, G. Shlyapnikov, J. Dalibard, *Phys.Rev.Lett.* 88(25), 250403 (2002).

- [72] F. Chevy, K.W. Madison, J. Dalibard, Phys. Rev. Lett. 85(11), 2223 (2000).
- [73] F. Chevy, K.W. Madison, V. Bretin, J. Dalibard, Phys. Rev. A 64(3), 031601 (2001).
- [74] C. Raman, J.R. Abo-Shaeer, J.M. Vogels, K. Xu, W. Ketterle, Phys. Rev. Lett. 87(21), 210402 (2001).
- [75] S. Inouye, S. Gupta, T. Rosenband, A.P. Chikkatur, A. Görlitz, T.L. Gustavson, A.E. Leanhardt, D.E. Pritchard, W. Ketterle, Phys. Rev. Lett. 87(8), 080402 (2001).
- [76] J.R. Abo-Shaeer, C. Raman, W. Ketterle, Phys. Rev. Lett. 88(7), 070409 (2002).
- [77] E. Hodby, S.A. Hopkins, G. Hechenblaikner, N.L. Smith, C.J. Foot, Phys. Rev. Lett. 91(9), 090403 (2003).
- [78] N.L. Smith, W.H. Heathcote, J.M. Krueger, C.J. Foot, Phys. Rev. Lett. 93(8), 080406 (2004).
- [79] D.R. Scherer, Ph.D. thesis, University of Arizona (2007).
- [80] A.E. Leanhardt, A. Görlitz, A.P. Chikkatur, D. Kielpinski, Y. Shin, D.E. Pritchard, W. Ketterle, Phys. Rev. Lett. 89(19), 190403 (2002).
- [81] A.E. Leanhardt, Y. Shin, D. Kielpinski, D.E. Pritchard, W. Ketterle, Phys. Rev. Lett. 90(14), 140403 (2003).
- [82] Y. Shin, M. Saba, M. Vengalattore, T.A. Pasquini, C. Sanner, A.E. Leanhardt, M. Prentiss, D.E. Pritchard, W. Ketterle, Phys. Rev. Lett. 93(16), 160406 (2004).
- [83] M.F. Andersen, C. Ryu, P. Cladé, V. Natarajan, A. Vaziri, K. Helmerson, W.D. Phillips, Phys. Rev. Lett. 97(17), 170406 (2006).
- [84] C. Ryu, M.F. Andersen, P. Cladé, V. Natarajan, K. Helmerson, W.D. Phillips, Phys. Rev. Lett. 99(26), 260401 (2007).
- [85] K.C. Wright, L.S. Leslie, N.P. Bigelow, Phys. Rev. A 77(4), 041601 (2008).
- [86] K.C. Wright, L.S. Leslie, A. Hansen, N.P. Bigelow, Phys. Rev. Lett. 102(3), 030405 (2009).
- [87] P.C. Haljan, B.P. Anderson, I. Coddington, E.A. Cornell, Phys. Rev. Lett. 86(14), 2922 (2001).

- [88] P. Engels, I. Coddington, P.C. Haljan, E.A. Cornell, Phys. Rev. Lett. 89(10), 100403 (2002) .
- [89] P. Engels, I. Coddington, P.C. Haljan, V. Schweikhard, E.A. Cornell, Phys. Rev. Lett. 90(17), 170405 (2003).
- [90] I. Coddington, P. Engels, V. Schweikhard, E.A. Cornell, Phys. Rev. Lett. 91(10), 100402 (2003).
- [91] V. Schweikhard, I. Coddington, P. Engels, S. Tung, E.A. Cornell, Phys. Rev. Lett. 93(21), 210403 (2004).
- [92] T.P. Simula, P. Engels, I. Coddington, V. Schweikhard, E.A. Cornell, R.J. Ballagh, Phys. Rev. Lett. 94(8), 080404 (2005).
- [93] S. Tung, V. Schweikhard, E.A. Cornell, Phys. Rev. Lett. 97(24), 240402 (2006).
- [94] V. Schweikhard, I. Coddington, P. Engels, V.P. Mogendorff, E.A. Cornell, Phys. Rev. Lett. 92(4), 040404 (2004).
- [95] P. Rosenbusch, V. Bretin, J. Dalibard, Phys. Rev. Lett. 89(20), 200403 (2002).
- [96] V. Bretin, S. Stock, Y. Seurin, J. Dalibard, Phys. Rev. Lett. 92(5), 050403 (2004).
- [97] S. Stock, Z. Hadzibabic, B. Battelier, M. Cheneau, J. Dalibard, Phys. Rev. Lett. 95(19), 190403 (2005).
- [98] R.A. Williams, S. Al-Assam, C.J. Foot, Phys. Rev. Lett. 104(5), 050404 (2010).
- [99] Z. Hadzibabic, P. Kruger, M. Cheneau, B. Battelier, J. Dalibard, Nature 441(7097), 1118 (2006).
- [100] V. Schweikhard, S. Tung, E.A. Cornell, Phys. Rev. Lett. 99(3), 030401 (2007)
- [101] P. Cladé, C. Ryu, A. Ramanathan, K. Helmerson, W.D. Phillips, Phys. Rev. Lett. 102(17), 170401 (2009).
- [102] M.W. Zwierlein, J.R. Abo-Shaeer, A. Schirotzek, C.H. Schunck, W. Ketterle, Nature 435(7045), 1047 (2005).
- [103] M.W. Zwierlein, A. Schirotzek, C.H. Schunck, W. Ketterle, Science 311(5760), 492 (2006).
- [104] C.H. Schunck, M.W. Zwierlein, A. Schirotzek, W. Ketterle, Phys. Rev. Lett. 98(5), 050404 (2007).

- [105] M. Kumakura, T. Hirotsu, M. Okano, Y. Takahashi, T. Yabuzaki, Phys. Rev. A 73(6), 063605 (2006).
- [106] T. Isoshima, M. Okano, H. Yasuda, K. Kasa, J.A.M. Huhtamäki, M. Kumakura, Y. Takahashi, Phys. Rev. Lett. 99(20), 200403 (2007).
- [107] T. Kuwamoto, H. Usuda, S. Tojo, T. Hirano, J. Phys. Soc. Jpn. 79(3), 034004 (2010).
- [108] Y.J. Lin, R.L. Compton, K. Jimenez-Garcia, J.V. Porto, I.B. Spielman, Nature 462(7273), 628 (2009).
- [109] Y. Shin, C. Sanner, G.B. Jo, T.A. Pasquini, M. Saba, W. Ketterle, D.E. Pritchard, M. Vengalattore, M. Prentiss, Phys. Rev. A 72(2), 021604 (2005).
- [110] Chad N. Weiler, Tyler W. Neely, David R. Scherer, Ashton S. Bradley, Matthew J. Davis, Brian P. Anderson. Nature 455, 948 (2008).
- [111] D. McKay, M. White, M. Pasienski, B. DeMarco, Nature 453(7191), 76 (2008).
- [112] L.E. Sadler, J.M. Higbie, S.R. Leslie, M. Vengalattore, D.M. Stamper-Kurn, Nature 443(7109), 312 (2006).
- [113] M. Vengalattore, S.R. Leslie, J. Guzman, D.M. Stamper-Kurn, Phys. Rev. Lett. 100(17), 170403 (2008).
- [114] E.A.L. Henn, J.A. Seman, E.R.F. Ramos, M. Caracanhas, P. Castilho, E.P. Olímpio, G. Roati, D.V. Magalhães, K.M.F. Magalhães, V.S. Bagnato, Phys. Rev. A 79(4), 043618 (2009).
- [115] E.A.L. Henn, J.A. Seman, G. Roati, K.M.F. Magalhães, V.S. Bagnato, Phys. Rev. Lett. 103(4), 045301 (2009).
- [116] T.W. Neely, E.C. Samson, A.S. Bradley, M.J. Davis, B.P. Anderson, Phys. Rev. Lett. 104(16), 160401 (2010).
- [117] D.V. Freilich, D.M. Bianchi, A.M. Kaufman, T.K. Langin, D.S. Hall, Science 329(5996), 1182 (2010). E. Lundh, C J Pethick and H Smith Phys. Rev. A 55 2126 (1997).
- [118] I. Corro, N. G. Parker and A. M. Martin, J. Phys. B 40, 3615 (2007).
- [119] Subhasis Sinha and Yvan Castin, Phys. Rev. Lett. 87, 190402 (2001).
- [120] I. Coddington, Ph.D thesis, JILA (2004).
- [121] P.W. Cleary, T.W. Hijmans, and J.T.M. Walraven, Phys. Rev. A, 82, 63635 (2010).

- [122] T. Bergeman, G. Erez, and H. J. Metcalf, Phys. Rev. A, 35, 1535 (1987).
- [123] O.J. Luiten, PhD thesis, University of Amsterdam (1993).
- [124] E.L. Surkov, J.T.M. Walraven and G.V. Shlyapnikov, Phys. Rev. A 49, 4778 (1994).
- [125] We verified that the approximation $\phi = \phi_m + \pi$ holds to within one degree for conditions relevant for our analysis.
- [126] G. Breit and I. I. Rabi, Phys. Rev. 38, 2082 (1931).

Summary

This thesis describes some interesting uses of an oscillating magnetic trap to manipulate a cloud of ultracold ^{87}Rb atoms. Although rubidium is a metal at room temperature, it has a finite vapour pressure of atoms which are in gaseous state. These atoms are slowed with resonant laser light and then trapped in a magnetic field minimum. Further cooling stages use radio frequency radiation to evaporatively cool the resulting cloud to a millionth of a degree above absolute zero temperature (-273 C) where the ensemble undergoes a phase transition to a state of matter known as a Bose-Einstein condensate (BEC). Our sample clouds have a cigar shape due to the geometry of the trapping potential and contain from tens of thousands up to six million atoms in the condensate state.

The isotope used here, ^{87}Rb was the first to be cooled all the way to this condensation. This achievement was rewarded with the Nobel prize for physics in 2001. The magnetic trap used in that first experiment is known as the time-averaged orbiting potential (TOP) trap and a variation of this type of trap will be the subject of this thesis. The TOP trap takes a static confining potential with its own characteristic trapping frequency and adds an oscillating bias field (TOP field) which circularly translates the trapping potential at a radius known as the "radius of death". The angular speed of this rotation is much faster than the oscillation frequency of the atoms in the static trap and hence the atoms are unable to follow the movement of the trap minimum. The atoms are trapped in an effective potential which is a time-average over the period of rotation of the TOP field.

Chapter 1 provides a short history of the TOP trap and the evolution of the time-averaged potential in experiments with Bose-Einstein condensates. It explains that the motion in the TOP is more complicated than is implied by the effective potential found by time-averaging. The atoms exhibit motion on both the static trap oscillation time scale and the faster one of the TOP field and we will use this insight to manipulate the motion of the cloud. It also introduces the concept of superfluidity, a property associated with BECs as well as vortices, an interesting manifestation of that property. A superfluid is a state of matter with zero viscosity, which means it shows no resistance to flow (analogously to superconductivity) and except in special conditions will not rotate when stirred. These special conditions include the presence of vortices, holes in the superfluid about which the superfluid circulates.

Chapter 2 describes the apparatus used for the experiments – principally the vac-

uum system, magnetic trap and laser light used to excite optical transitions. The experiments create an incredibly cold atomic sample in a room temperature environment and so vacuum conditions are needed to minimize collisions with hot background atoms. Laser light is used to cool the atoms, to pump them to the correct (trappable) spin states and then also to image them onto a camera. Magnetic trapping is done both with an interlinked set of about 20 coils with intricate switching circuitry and with the relative simplicity of a set of permanent magnets.

Chapter 3 takes a deeper look at the changes in the optical system. An external cavity diode laser and a distributed feedback diode laser were stabilized to atomic transitions of a rubidium gas in a vapour cell. A laser amplifier system was developed from a commercially available diode which allowed us to stably amplify the power from our master lasers by up to 50 times. The imaging system was improved so that imaging was possible along the both the long and short axes of the clouds. In the process of this modification we also succeeded in measuring and improving both the resolution and the signal-to-noise of our imaging system.

Chapter 4 describes the first set of new experiments on this apparatus. Previously all experiments on this apparatus were performed with the $F = 2, m_F = 2$ spin substate of ^{87}Rb . To investigate a BEC cloud on longer timescales, another trappable state, the $F = 1, m_F = -1$ state is used. We adapted the apparatus and sequence of the experiments to work with this state and created a BEC in our conventional trap as well as various TOP traps. We indeed found that atoms in this $F = 1$ state had longer lifetimes and were able to characterize the main limiting factor of this lifetime: collisions between three atoms at once. This chapter also discusses the generation of vortices in BECs and by rotating ("spinning") an elliptical TOP trap, we try to generate vortices in our clouds. These experiments yielded rather unsatisfactory results, as although we found some indications of vorticity, we were unable to produce clear images of vortex holes in our clouds. We suspect this was due to insufficient homogeneity of the trapping potential.

Chapter 5 contains the main results of this thesis. We describe in detail the subtleties of atomic motion in the TOP trap and in particular the role of the phase of the oscillating TOP field. By numerical and analytical methods we show the importance of the initial phase of this field at switch-on when we transfer the atoms from a static trap to an oscillating trap such as a TOP trap. The resultant sloshing motion of the center of the mass of the cloud from this switch-on can be substantial compared to the micromotion due to the oscillating potential and this effect is found to be dependent on the initial phase of the TOP field. We also show how this motion can be quenched by a well-timed jump in the phase of the TOP field. We describe how this phase jump can be optimally chosen and proceed to demonstrate experimentally both the switch-on effect and successful motion quenching experiments.

Samenvatting

In dit proefschrift onderzoeken we een aantal interessante toepassingen van een oscillerende magnetische val waarmee we een wolk van ultrakoude atomen ^{87}Rb manipuleren. Hoewel rubidium een metaal is bij kamertemperatuur, heeft het een meetbare dampdruk. De atomen in de gasfase worden met resonant laserlicht gekoeld en vervolgens worden ze naar een spintoestand gepompt die in een magnetisch veldminimum gevangen kan worden. Verdere koeling gebeurt met het gebruik radiofrequente straling tot dat de resulterende wolk een temperatuur bereikt van een miljoenste graad boven het absolute nulpunt van de temperatuur (-273°C). Het atomaire gas ondergaat een faseovergang naar een toestand van materie bekend als een Bose-Einsteincondensaat (BEC). Onze condensaten hebben de vorm van een sigaar wat en bevatten tienduizend tot zes miljoen atomen.

Wij gebruikten de isotoop ^{87}Rb , waarmee in 1995 als eerste atomaire gas BEC werd bereikt. In 2001 werd voor dit werk de Nobelprijs voor natuurkunde uitgereikt. De magnetische val in dat experiment staat bekend als de time-averaged orbiting potential (TOP) trap en een variatie van dit type val zal het hoofdonderwerp van dit proefschrift zijn. De TOP-trap bestaat uit een statische magneetval gecombineerd met een snel roterend magneetveld (het TOP-veld). Het veldminimum doorloopt in deze val een cirkelbeweging met een straal die bekend staat als de 'afstand des doods'. De hoeksnelheid van deze rotatie is veel sneller dan de oscillatiefrequentie van de atomen in de statische val en dus zijn de atomen niet in staat de beweging van het veldminimum te volgen. De atomen zijn zo gevangen in een effectieve potentiaal die gelijk is aan het tijd-gemiddelde over de periode van de rotatie van het TOP-veld.

Hoofdstuk 1 geeft een korte geschiedenis van de TOP-val en de evolutie van de tijds-gemiddelde potentiaal in experimenten met Bose-Einstein condensaten. Het verklaart dat de beweging in de TOP is ingewikkelder dan wordt geïmpliceerd door het effectieve potentieel beeld. De atomen tonen beweging op een lange tijdschaal, bepaald door de gemiddelde potentiaal, en een korte tijdschaal gegeven door het de snel-roterende TOP-veld. We zullen gebruik maken van dit inzicht om de beweging van de wolk te manipuleren. In dit hoofdstuk introduceren we ook het concept van de supervloeistof, een eigenschap die verband houdt met BEC's en vorticeiteit (werveling). Een supervloeistof is een toestand van materie zonder stromingsweerstand. Dit is analoog aan supergeleiding in metalen. De vortices kunnen gezien worden als 'gaten' in de supervloeistof rond welke de supervloeistof circuleert.

Hoofdstuk 2 beschrijft de bij de experimenten gebruikte apparatuur: het vacuüm systeem, de magnetische val en het laserlicht gebruikt om optische overgangen te maken. De experimenten zorgen voor een ongelooflijk koud atomair monster in een omgeving bij kamertemperatuur. Hiervoor is een hoog vacuüm van belang om botsingen met het achtergrondgas te minimaliseren. Het laserlicht wordt gebruikt om de atomen af te koelen, te pompen naar de juiste spintoestanden en tevens om de atomen op een camera af te beelden. De magnetische opsluiting vindt plaats doormiddel van ongeveer 20 spoelen en een aantal permanente magneten.

In hoofdstuk 3 wordt dieper ingegaan op de details van het optische systeem. De diode-lasers worden gestabiliseerd met behulp van atomaire overgangen in een gas in een rubidium-dampcel. Een radiofrequent gemoduleerd magnetisch veld rond de cel wordt gebruikt om een elektronisch terugkoppelsignaal te genereren. Een laser-versterker werd ontwikkeld uit een in de commerciële beschikbare diodelaser waarmee het licht van onze lasers tot 50 keer stabiel versterkt kon worden. Het afbeeldingssysteem werd verbeterd zodat afbeelden van de gaswolk op de camera mogelijk werd langs zowel de lange als de korte as van de wolk.

Hoofdstuk 4 beschrijft de eerste reeks nieuwe experimenten met deze apparatuur. Eerder zijn alle experimenten op dit apparaat uitgevoerd met de $F = 2; m_F = 2$ spintoestand van ^{87}Rb . Om een BEC wolk te onderzoeken op langere tijdschalen is de $F = 1; m_F = -1$ toestand gebruikt. Wij hebben de geometrie en van de experimenten aangepast om te kunnen werken met deze toestand en creëerden een BEC in onze conventionele val evenals in diverse TOP-vallen. We vonden inderdaad dat atomen in deze $F = 1$ toestand een langere levensduur hadden en waren in staat om de belangrijkste beperkende factor van voor deze levensduur te karakteriseren: botsingen tussen drie atomen tegelijk. Dit hoofdstuk bespreekt ook de generatie van vortices (wervels) in BEC's en door het draaien van een elliptische TOP-val hebben wij geprobeerd wervels in onze wolken te genereren. Deze experimenten leverden onduidelijke resultaten, want hoewel wij een aantal aanwijzingen vonden voor vorticeiteit, waren we niet in staat om duidelijke vortex-gaten in onze wolken af te beelden. We vermoeden dat dit te wijten is aan onvoldoende homogeniteit van onze magnetische potentiaal.

Hoofdstuk 5 bevat de belangrijkste resultaten van dit proefschrift. We beschrijven in detail de atomaire beweging in de TOP val en in bijzonder de rol van de fase van het roterende TOP-veld. Door numerieke en analytische methoden tonen wij het belang aan van de fase van dit veld bij het inschakelen, wanneer het atomaire gas vanuit een statische- in een TOP-val wordt overgebracht. De resulterende langzame 'klotsende' beweging van het centrum van de gaswolk is aanzienlijk vergeleken met de snelle microscopische beweging en is sterk afhankelijk van de initiële fase van het TOP-veld. We laten ook zien dat deze klotsbeweging vervolgens kan worden onderdrukt middels een goed getimede sprong in de fase van het TOP-veld. We demonstreren hoe deze fasesprong optimaal worden gekozen en vervolgens wordt experimenteel zowel het inschakel-effect als de succesvolle demping van deze beweging aangetoond.

Acknowledgements

When you spend close to a decade at a task and you start a little unsuited to it, then you end up with a lot of people to thank. To begin I must speak of my promoter Prof. Jook Walraven. Jook took a bit of a gamble handing over control of a complex experiment to an algebraist with limited experience of (or ahem, affinity for) apparatus. After a couple of false starts, we managed to find a good working rhythm together, resulting in (amongst other things) a design for a laser amplifier and eventually a rather well-written paper to be proud of. Along the way I learned so much of a scientific and social nature from Jook that I emerged as a fully-formed engineer. It looks like I will be last of a long and illustrious line of PhD students who have Jook as their promotor and I would like to say a sincere thank you from us all.

Absolutely essential to reaching a successful end was the always helpful prodding of the unique Tom Hijmans. Tom got involved in this project just as I obtained control over the experiment, but at a stage when any meaningful results seemed intangibly far away. After some months of fruitless searching for cloud-holes, it was Tom who steered us in the direction of the phase of the TOP trap and provided essential theoretical support as well as invaluable labtime for the main results of this thesis. Sincerest thanks Tom also for giving me gainful employment at the praktikum - it was always a pleasure to work with you.

But of course there were others, so many others. In the beginning, at Amolf on the Kruislaan, there were 3 predecessors; Kai, Igor and Christian who left behind an impressively complicated apparatus and a treasure trove of labbooks. For 6 months I worked on laser modules next to the main lab with the help of Idsard Attema, Henk Dekker, Ton Vijftigschild, Wim Brouwer, Henk Sodenkamp, Ilia Cerjak and the all-round brilliance of Hinc Schoenmaker. Meanwhile a wonderful control system was built by Duncan Verhijde and Hans Alberda which proved to be more than I ever could have wished for to run the experiments. In that first year I was spoiled for choice with two great postdocs Wolf van Klitsing and Jeremie Leonard at my disposal until both got better offers and were off to pastures new. I missed you guys in later years!

In the summer of 2004, my life got turned upside down and as the summer closed I was a father, a husband and working with a heap of boxes in the cellar at the Valckenierstraat. Luckily I had some great new neighbors on their way there with the always helpful Steve, the knowledgeable Sebastian, “sporty” Tobias (climbing, rugby, baseball), and the simply wonderful Antje (world’s greatest paranimf!) in the

lab next door and Carolijn and eventually Richard across the corridor. I also had a number of masters students who helped me in the lab especially Maarten, Guillaume and Nicolas whom I would also like to thank. Apart from these neighbours, the WZI on Valekenierstraat had a host of other characters with whom you could talk physics, politics or football. I think in particular of the trio of theoreticians Carlos, Micha and Piotr who worked with Gora Shlyapnikov; the BEC on a chip group of Aaldert, Jan-Joris, Shannon and the inspirational Philipp Wicke under the guidance of Klaasjan (adept at a good pep-talk when it was most needed) and the permanent magnets group of Ben, Robert, Iuliana, our babysitter Vlad, Atreju, Vanessa and Rene. Together we made up the quantum gases group and had frequent colloquia with our cousins from the VU as well as a very productive literature club which introduced me to the ideas in this thesis. There was also an institute full of physicists of other disciplines experimental and theoretical on Valckenierstraat and a great boss in Mark Golden.

There was also a whole new support crew at the UvA for me to bother with all my electrical, mechanical, vacuum, design and administration problems. And I had enough to go around so thanks go to Theo van Lieshout, Hans Agema, Herman Prins, Pieter Sannes, Johan te Winkel for their time and help with all kinds of electrical issues, to Edwin Baay, Frans Pinkse, Aloff Wassink, Ed de Water for their electrical circuit designs, Hans Gerritsen, Gerrit Hardeman, Ben Harrison and Taco Walstra for their computerized expertise, to Cees van den Biggelaar, Harry Beukers, Wim van Aartsen, Fred van Anrooij, Wietse Buster, Tjerk van Goudoever, Jan Kalwij, Farah Kuckulus, Diederick Kwakkestijn, Ben Klein-Meulekamp, Henk Luijten (the master of PEEK), Joost Overtoom (provider of beer and precision work), Jur Plum, Johan Soede, Daan de Zwarte for all their help with mechanical parts of the experiment and to Ron Manuputy and his team Mattijs Bakker, Hans Ellermeijer, Eric Hennes for their design capabilities, to that man Bert Zwart for his procurement, supplies and vacuum knowledge and finally to Rita Vinig, Ineke Baas, Luuk Lusink, Joost van Marmeren and Meike Scholten for their help with my admin issues. Guys, thanks to you all I finally made it!

Looking back to the road which took me here, I'd like to thank my parents for giving me the freedom to choose my own path and for being there when I needed them and also my sisters Sandra and Orla and extended family for teasing me for being an eternal student and my brother Adrian for having the patience to put up with me. I also want to mention my friends from home Brian, Consey, John Flynn, Shane, Jamie and David for the great way that we can meet up every year or every other year and simply carry on as if time hadn't passed at all. Next, to the friends who I studied with: Marcus Foley, David Prendergast, Daniel Winter, Peter Curran and Paul O'Leary for generally dragging me through my first degree (in Physics) and also popping up again in later years in Germany and Amsterdam. I should next thank the Irish winter and my colleagues on the big dig for convincing me that my future lay in science and not in the freezing cold/archaeology.

On to Germany, to Tuebingen and the intercultural phenomena which are AEG, Erasmus and student exchanges. Tuebingen was such a wonderful place to find the world from with an amazing array of international flatmates (Sandrine, Summer, Mike, Ryu, Ales,...) football teammates (Jonny, Johnny, Mark,...) and drinking buddies (all of the above and so many more!) of all nationalities. But there was also time to become a diplom mathematiker with Nikolai, Yilmaz, Vera, Joris and Prof. Ihringer who all helped convince me that I was a physicist meddling in mathematics and not the other way around.

And so after a lively interlude at the LMU in Munich, it was onwards to Amsterdam, but not without someone precious – my lovely then-pregnant, wife-to-be Yanchun. I have to thank Jook and especially Marian for the warm welcome they gave us in Amsterdam and our friends Holly and Massimo, Devi and Steven, Tommy (always ready for tennis or a beer) and Mary (always ready with a helpful hand) for making life fun. My thanks also to Raoul and Roland and all the others who allowed me over the years to take out the frustration of the lab rat on a tennis court wherever we could find it. And to the students and teachers at the chinese school in Amsterdam, who managed to make me realize the delicacy of the dutch language as well as the mysteries of mandarin. I also want to mention Yanchun's family her Dad, her brother, her sister-in-law and little Huanhuan, but especially her wonderful Mum who helped out so much. *xie xie!*

While writing this thesis the whole lab moved from valckenierstraat to the science park and I moved to industry and the provinces, so I really have to thank the DPP team at ASML for allowing me the flexibility to take time off to work on my thesis when I needed and for providing a stimulating and open working environment that made the writing in the evenings much easier. Oh and Simon, who always managed a bit of perspective on things. I also want to thank our friends in Vught, Maarten and Red and our lovely neighbours (Paul, Morven, Rieta) for giving us a near instant feeling of home here.

And speaking of home the last and greatest thanks goes to my dear Yanchun. Nine years of my rollercoaster ride of despair, grumpiness, late evenings, elation, resignation and squeezed out success, how did you manage to put up with it? You deserve your own doctor title so much; maybe you felt the only way to understand my struggle was to join in. Your unique way of looking at the world, your passion, love and support pulled me through this, so I have you to thank the most. We started in January 2004 as two but with another on the way but now we have two lovely daughters 4 and 8 years old. Leaya and Zhurui: Mama and Papa have now both written books and both will have doctor titles, just like dr. Seuss. And best of all you don't have to hear that word that means "I'm busy": *thesis!*

